NorthWest Research
Associates, Inc.

NWRA-CR-99-R195

5 March 1999

Final Report

Investigation of Tropical Transport with UARS Data

Prepared by

Timothy J. Dunkerton

Prepared for

Stephen P. Cimino
Contracting Officer, Code 289
NASA
Goddard Space Flight Center
Greenbelt, MD 20771

Contract No. NAS5-32862

TABLE OF CONTENTS

Abstract

Measurements of trace constituents obtained by instruments aboard the Upper Atmosphere Research Satellite (UARS) have been used to study transport processes associated with the quasi-biennial oscillation, laterally propagating Rossby waves, and upward propagating Kelvin waves in the tropical and subtropical upper troposphere and stratosphere. Mean vertical motions, vertical diffusivities and in-mixing rates were inferred from observations of the 'tape recorder' signal in near-equatorial stratospheric water vapor. The effect of the QBO on tracer distributions in the upper half of the stratosphere was seen in a spectacular 'staircase' pattern, predominantly in the winter hemisphere, revealing the latitudinally asymmetric nature of QBO transport due to induced mean meridional circulations and modulation of lateral mixing associated with planetary Rossby waves. The propagation of Rossby waves across the equator in the westerly phase of the QBO was seen in tracer fields and corroborating UKMO analyses; a modeling study of the effect of these waves on typical QBO wind profiles was performed. Water vapor in the upper troposphere and lower stratosphere was found to exhibit signatures of the tropical intraseasonal oscillation (TIO) and faster Kelvin waves in the two regions, respectively.

These observational studies demonstrate a remarkable capability of UARS measurements to elucidiate several fundamental aspects of dynamics and transport in the tropical upper troposphere and stratosphere. Noteworthy among these is an estimation of upwelling due to the Brewer-Dobson circulation, which had not been observed directly prior to UARS, and the hydration of the tropical upper troposphere due to the passage of the convectively active phase of the TIO.

TRACE CONSTITUENT TRANSPORT

GEOPHYSICAL RESEARCH LETTERS, VOL. 23, NO. 18, PAGES 2497-2500, SEPTEMBER 1, 1996

Mixing zone in the tropical stratosphere above 10 mb

Timothy J. Dunkerton and Donal J. O'Sullivan

Northwest Research Associates, Bellevue, Washington

Abstract. Observations of trace constituents obtained from the Upper Atmosphere Research Satellite in late winter 1991/92 reveal a zone of quasi-horizontal stirring in the tropical stratosphere above 10 mb, equatorward of the subtropical jet. This mixing region was separated from the midlatitude surf zone by a strong gradient of potential vorticity and tracer along the jet axis. The jet and accompanying gradients are climatological features. Mixing equatorward of the jet evidently depends on the phase of the quasi-biennial oscillation.

Introduction

The distribution of long-lived trace constituents in the middle atmosphere is affected by quasi-horizontal stirring due to planetary Rossby waves and instabilities resulting from these waves. Preferred regions of mixing include the 'surf zone' in the midlatitude winter stratosphere [*McIntyre and Palmer*, 1984], the polar winter mesosphere [*Dunkerton and Delisi*, 1985], and the lowermost stratosphere in all seasons [*Chen*, 1995; *Dunkerton*, 1995; *Holton et al*, 1995]. Steep horizontal gradients of potential vorticity and trace constituents are observed at the lateral boundaries of mixing regions. In this letter we describe another region of stirring, the northern tropical stratosphere above 10 mb, as observed by instruments aboard the Upper Atmosphere Research Satellite (UARS) in late winter 1991/92.

Data Analysis

Several UARS constituents were examined, including water vapor (H_2O) from the Microwave Limb Sounder (MLS) version 3 [*Barath et al*, 1993; *Waters et al*, 1993] and nitrous oxide (N_2O) from the Cryogenic Limb Array Etalon Spectrometer (CLAES) version 7 [*Roche et al*, 1993]. Features described in this letter were observed in other UARS constituents as well, but could be seen more clearly in some tracers than in others, depending on the background distribution. Level 3AT data, consisting of soundings along the orbital track, were interpolated to a longitude-latitude grid using 4 consecutive days of data as input. The weight function was an elliptical gaussian with major axis aligned in the zonal direction. Assigning a relatively small radius of influence (3°x1°) to this function, comparable to the distance between soundings, strong tracer gradients were preserved, as well as in the original data. A disadvantage of this method is that any rapidly evolving (< 4-day) disturbances are aliased into spurious features with short longitudinal scale. Aliasing was insignificant in the examples shown, but small-scale features in our tracer figures should be viewed with caution. This simple procedure captured the slow evolution of tracers affected by quasi-stationary planetary waves, and was entirely adequate for zonally averaged latitude-height cross sections. Circulation data were obtained from the United Kingdom Meteorological Office (UKMO) analyses [*Swinbank and O'Neill*, 1994], and the state of the quasi-biennial oscillation (QBO) at the equator was determined using rawinsonde data from Singapore (1.4°N, 104.0°E).

Paper number 96GL02302
0094-8534/96/96GL-02302$05.00

Results

Figure 1 displays the mean zonal wind at 4.6 mb for UARS day 50-650 beginning in November 1991. The first northern winter, occurring in a deep easterly phase of the QBO (~70-15 mb), experienced stronger wave activity and a more disturbed vortex than the second winter, occurring in a deep westerly phase. Aside from differences in timing, the mean flow evolution was qualitatively similar in the two winters. Breakdown of midwinter westerlies led to the formation of a detached subtropical westerly jet near 30°N. This jet is commonly observed in late northern winter [*Randel*, 1992] persisting for one or two months after the transition to easterlies at higher latitudes.

To illustrate the relation between the subtropical jet and quasi-horizontal stirring, we focus on the second half of February and first half of March 1992, UARS days 160-185, indicated at the top of Fig. 1 by a bold line. Figures 2a,b show latitude-height cross sections of MLS H_2O and CLAES N_2O, respectively, averaged over this time interval. Figure 3 shows the corresponding latitude-height cross section of mean zonal wind, from UKMO analyses. The axis of the subtropical jet is indicated by a bold curve in each of the figures, and a few isopleths of N_2O are superposed in Fig. 3. Both constituents display an unusual 'staircase' pattern in the latitude-height plane (highlighted in yellow). This complicated pattern can be separated into individual features and interpreted, tentatively, as follows: 1) In the upper stratosphere south of the equator, tracer isopleths are pushed upward due to Brewer-Dobson upwelling. 2) In the upper stratosphere north of the equator, between 10 and 2.2 mb, there is a region of weak tracer gradient due to quasi-horizontal stirring (as shown below). 3) Near the tropical stratopause there

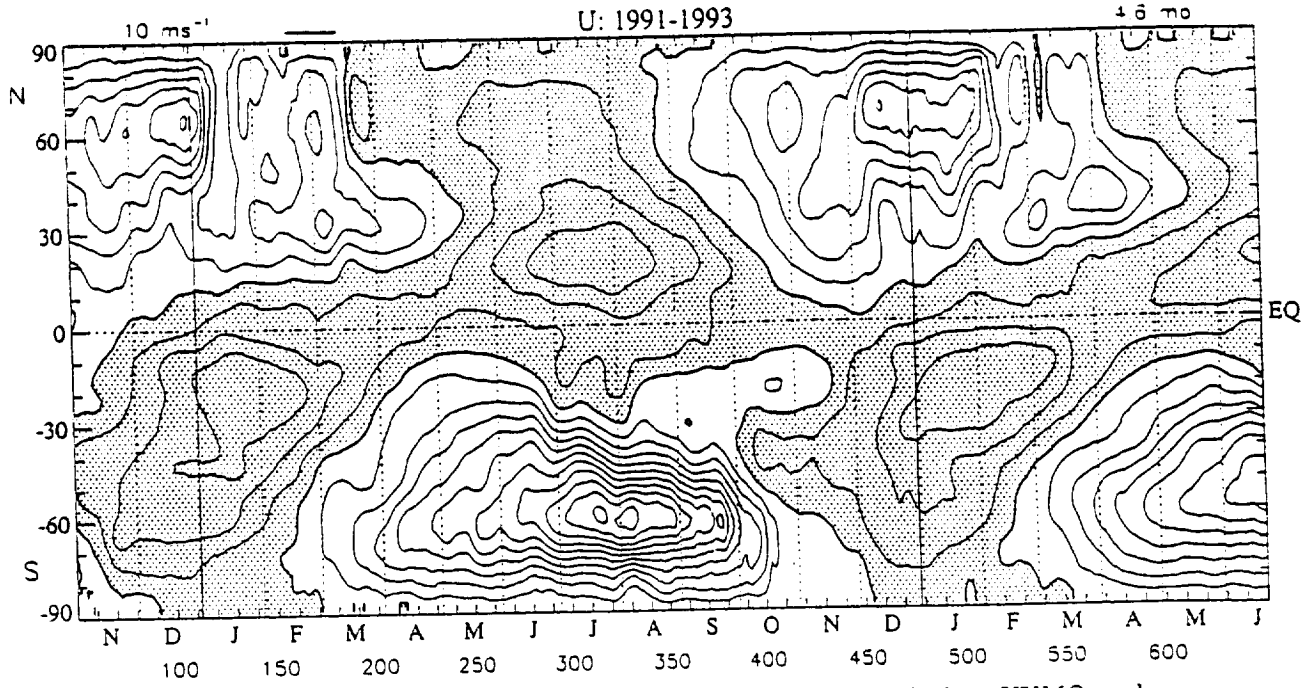

Figure 1. Latitude-time cross section of mean zonal wind at 4.6 mb, from UKMO analyses. Contour interval 10 ms^{-1}, easterlies are shaded.

is a double-peak structure associated with the onset of the semiannual oscillation (SAO) west phase. 4) In the tropical middle stratosphere, there is another double-peak structure associated with the onset of the QBO west phase. This feature is visible as a weak depression of tracer isopleths on the equator accompanied by tracer anomalies on either side, the one on the north side being especially prominent in N_2O. 5) There is a strong horizontal gradient of tracer along the axis of the subtropical jet, extending from the middle stratosphere, where the gradient is visible in both tracers, to the upper stratosphere, where the gradient is evident only in H_2O. Lack of a strong gradient in N_2O is attributable to the small amount and/or weak background gradient of this constituent in the upper stratosphere. 6) Tracer isopleths in the midlatitude Northern hemisphere stratosphere are quasi-horizontal, extending across the region of weak mean zonal wind, i.e., the surf zone. 7) A modest horizontal gradient of N_2O at 46-22 mb, but not of H_2O, coincides with the axis of a weak polar night jet near 60°N.

Comparing Fig. 2 with a cross section one year later, in the opposite phase of the QBO, we find several similarities and differences. There is a strong gradient of tracer coincident with the subtropical jet, flat isopleths of tracer across the midlatitude surf zone, and a modest N_2O gradient approaching polar latitudes (not shown). The SAO double peak is also apparent. On the other hand, there is less evidence of Brewer-Dobson upwelling south of the equator, no hint of QBO anomaly in the middle stratosphere, and no evidence of quasi-horizontal stirring in the upper half of the tropical stratosphere.

The QBO evidently affects the distribution of conserved tracers in four ways. 1) QBO circulation cells in the tropics advect tracers horizontally and vertically in the latitude-height plane. 2) The QBO zonal wind anomaly determines whether planetary Rossby waves can enter the tropical stratosphere from the winter hemisphere. 3) The equatorial QBO affects the polar vortex and planetary-wave flux in the northern winter stratosphere, thereby indirectly influencing the amount of wave activity that can enter the tropics, and 4) the strength and southern extent of the Brewer-Dobson circulation.

We note incidentally that UKMO analyses underestimated the onset of the QBO west phase in early 1992 relative to that of Singapore. While there is a suggestion in Fig. 3 of westerly vertical shear at the equator above 22 mb, Singapore winds revealed a much stronger shear with absolute westerlies maximizing at almost 20 ms^{-1}. The reason for this discrepancy is unknown.

The latitude-height cross sections of tracer and mean zonal wind in Figs. 2,3 are representative of shorter intervals within this time period. Figure 4 displays a horizontal map of CLAES N_2O and UKMO zonal wind for UARS days 180-183 at the 4.6 mb level. There was a significant planetary-wave event in March 1992, leading to the breakdown of a remnant vortex and final transition to summer easterlies at higher latitudes. This event was underway during the time period shown, but unfortunately, the north-viewing yaw period of UARS ended on day 194.

In Fig. 4, a strong tracer gradient just north of the equator bifurcates into two strong gradients near the dateline; the northern one links up with the subtropical jet and closely follows the jet axis as it meanders through the Western hemisphere and extends into midlatitudes in the Eastern hemisphere. The flow is dominated by wavenumber 1, but higher wavenumbers

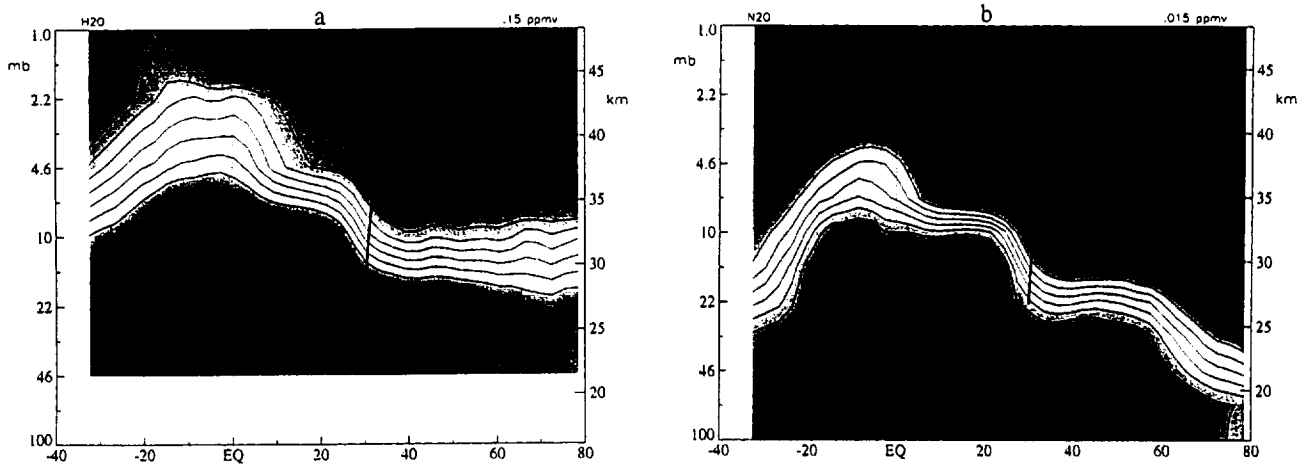

Figure 2. Latitude-height cross sections of (a) MLS H_2O, and (b) CLAES N_2O, averaged over UARS day 160-185. Contour interval is 0.15 ppmv in (a), starting at 3.8 ppmv (dark blue); 0.015 ppmv in (b), starting at 0.015 ppmv.

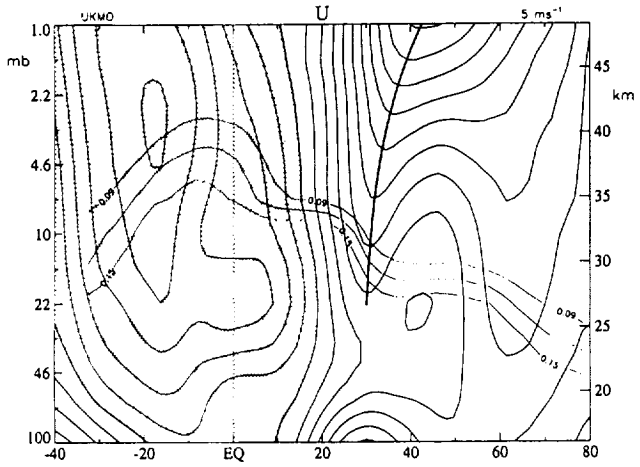

Figure 3. Latitude-height cross section of mean zonal wind, from UKMO analyses, averaged over UARS day 160-185. Contour interval 5 ms^{-1}, easterlies are shaded. A few isopleths of N_2O are also shown (thin lines).

develop in the Western hemisphere inside the tropical mixing region. A sequence of maps around this time suggests that the apparent flux of high N_2O concentrations into the Northern hemisphere is occurring in two branches: one near the dateline, and another near 90°W. Spontaneous formation of higher wavenumbers was observed in nonlinear simulations of a Rossby-wave critical layer [*Salby et al*, 1990].

What is remarkable about this picture, in contrast to the usual midlatitude surf zone, is that the narrow mixing region occurs equatorward of the subtropical jet, rather than poleward of it, and is dynamically separated from the midlatitude mixing region. In effect, one can imagine that the subtropical jet has split the surf zone into two parts: a midlatitude part and a tropical part. The tropical mixing zone is isolated from the midlatitude surf zone at most longitudes, except over east Asia and the west Pacific. Meridional displace-

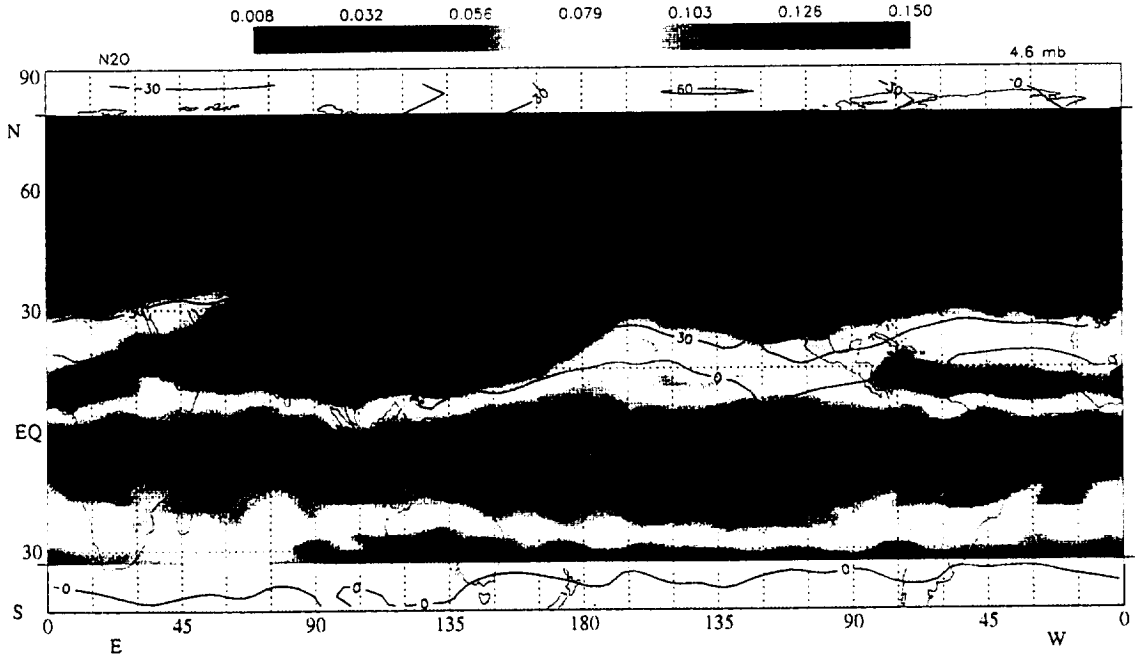

Figure 4. Horizontal map of CLAES N_2O and UKMO zonal wind at 4.6 mb, averaged over UARS day 180-183. Units: ppmv (N_2O) and ms^{-1} (zonal wind).

ment of air parcels is reduced in the jet core, so that mixing is inhibited there. Mixing is encouraged where parcel displacements are large, i.e., approaching a critical layer. This interpretation is supported by Fig. 3, showing that the zero-wind line intersects the tropical mixing zone above 10 mb. The subtropical jet and accompanying PV/tracer gradients are most likely the result of i) Coriolis torques due to a mean meridional circulation extending outside the region of wavedriving to the north, and ii) mixing on either side of the jet maximum.

Conclusion

UARS observations suggest that the so-called subtropical transport 'barrier', evident at lower levels in volcanic aerosol and trace constituents [e.g., *Trepte and Hitchman*, 1992, *Randel et al*, 1994] extends to higher altitudes and represents not only the equatorward boundary of the midlatitude surf zone but also the poleward boundary of an intermittent mixing zone in the tropical upper stratosphere. Although this region is not as isolated from midlatitude disturbances as at lower levels, the subtropical jet separates the intermittent tropical mixing from the more pervasive stirring in the midlatitude surf zone. Except where the subtropical gradient is breached, there is tendency for the tropical stratosphere to remain isolated even at higher levels. During the west phase of the QBO, a strong tracer gradient also develops at the equator, which marks the southern boundary of the tropical mixing zone.

Strong PV/tracer gradients often coincide with westerly jets in the atmosphere and ocean because Rossby-wave and instability critical levels cannot exist near a westerly maximum. Propagating Rossby waves must have negative intrinsic phase speed and therefore cannot have a critical level near the center of a westerly jet. Barotropic and baroclinic instabilities must have a critical level in a region of reversed potential vorticity gradient, which can only occur in the flanks of a westerly jet. Mixing is therefore inhibited near the jet core, but as long as the maximum wind is not too strong, Rossby waves can propagate across the jet and break in adjacent regions of weaker mean flow.

Not all tracer gradients are necessarily the result of Rossby wavebreaking. A strong, zonally symmetric N_2O gradient at the southern boundary of the domain in Fig. 4 suggests a possible role for differential upwelling in subtropical latitudes of the summer hemisphere, in addition to a 'leftover' effect of wavebreaking from the previous winter. Further study is necessary to determine the relative importance of these effects.

Acknowledgments. This research was supported by the National Aeronautics and Space Administration. Contracts NASW-4844 and NAS5-32862. and by the National Science Foundation, Grant ATM-9301105.

References

Barath, F.T., and Co-authors, The Upper Atmosphere Research Satellite Microwave Limb Sounder instrument. *J. Geophys. Res., 98*, 10,731-10,762, 1993.

Chen, P., Isentropic cross-tropopause mass exchange in the extratropics. *J. Geophys. Res., 100*, 16,661-16,673, 1994.

Dunkerton, T.J., Evidence of meridional motion in the summer lower stratosphere adjacent to monsoon regions. *J. Geophys. Res., 100*. 16,675-16,688, 1995.

Dunkerton, T.J., and D.P. Delisi, The subtropical mesospheric jet observed by the Nimbus 7 Limb Infrared Monitor of the Stratosphere. *J. Geophys. Res., 90*, 10,681-10,692, 1985.

Holton, J.R., P.H. Haynes, M.E. McIntyre, A.R. Douglass, R.B. Rood, and L. Pfister, Stratosphere-troposphere exchange. *Rev. Geophys., 33*, 403-439, 1995.

McIntyre, M.E., and T.N. Palmer, The 'surf zone' in the stratosphere. *J. Atmos. Terr. Phys., 46*, 825-849, 1984.

Randel, W.J., Global Atmospheric Circulation Statistics, 1000-1 mb. *NCAR Tech. Note* (NCAR/TN-366+STR), Boulder, CO, 1992.

Randel, W.J., B.A. Boville, J.C. Gille, P.L. Bailey, S.T. Massie, J.B. Kumer, J.L. Mergenthaler, and A.E. Roche, Simulation of stratospheric N_2O in the NCAR CCM2: comparison with CLAES data and global budget analyses. *J. Atmos. Sci., 51*, 2834-2845, 1994.

Roche, A.E., J.B. Kumer, J.L. Mergenthaler, G.A. Ely, W.G. Uplinger, J.F. Potter, T.C. James and L.W. Sterritt, The Cryogenic Limb Array Etalon Spectrometer (CLAES) on UARS: experiment description and performance. *J. Geophys. Res., 98*, 10,763-10,776, 1993.

Salby, M.L., D. O'Sullivan, R.R. Garcia, and P. Callaghan, Air motions accompanying the development of a planetary wave critical layer. *J. Atmos. Sci., 47*, 1179-1204, 1990.

Swinbank, R. and A. O'Neill, A stratosphere-troposphere data assimilation system. *Mon. Wea. Rev., 122*, 686-702, 1994.

Trepte, C.R., and M.H. Hitchman. The stratospheric tropical circulation deduced from aerosol satellite data. *Nature, 355*, 626-628, 1992.

Waters, J.W., L. Froidevaux, W.G. Read, G.L. Manney, L.S. Elson, D.A. Flower, R.F. Jarnot, and R.S. Harwood, Stratospheric ClO and ozone from the Microwave Limb Sounder on the Upper Atmosphere Research Satellite. *Nature, 362*, 597-602, 1993.

T. J. Dunkerton and D. J. O'Sullivan, Northwest Research Associates, P.O. Box 3027, Bellevue, WA 98009. e-mail: tim@nwra.com; donal@nwra.com

(received May 8, 1996; revised June 25, 1996; accepted June 28, 1996.)

GEOPHYSICAL RESEARCH LETTERS, VOL. 24, NO.12, PAGES 1483-1486, JUNE 15, 1997

Cross-equatorially radiating stratospheric Rossby waves

Donal O'Sullivan
Northwest Research Associates, Bellevue, Washington

Abstract. Upper Atmosphere Research Satellite observations of constituent distributions in the middle stratosphere show that extratropical Rossby waves from the winter hemisphere can, at certain times, radiate across the equator and reach the summer subtropics before they break and are absorbed. Conditions are most favorable for Rossby waves to radiate into the tropics when the westerlies of the winter hemisphere extend to low latitudes, as usually occurs during November and December in the northern hemisphere. Cross-equatorial radiation of quasi-stationary Rossby waves requires westerly equatorial winds, as occurred in the middle stratosphere in late 1992. Constituent distribution maps show numerous episodes of Rossby-wave radiation across the equator during this early winter period, but not after early January 1993. Wave breaking in both the winter and summer subtropics above 22 mb causes constituent exchange between the tropics and extratropics, including deep tropical in-mixing.

Introduction

Little is known observationally about the interaction of extratropical stratospheric Rossby waves with the tropics partly because Rossby waves have a relatively weak temperature signal at low latitudes. Such information is desirable, however, as Rossby waves from the winter hemisphere may impart significant momentum to the tropics and because they can induce constituent transport. Here the distributions of a long-lived constituent species, nitrous oxide (N_2O), are analyzed to reveal eddy motions at low latitudes in the middle stratosphere. United Kingdom Meteorological Office (UKMO) assimilated winds [*Swinbank and O'Neill*, 1994] are also used to interpret the deduced wave behavior.

Data

N_2O observed by the Cryogenic Limb Array Etalon Spectrometer (CLAES) instrument [*Roche et al.*, 1993] on the Upper Atmosphere Research Satellite (UARS) are used here. The data used were Level 3AT, consisting of soundings along the orbital track. The UARS orbit allowed coverage of the stratosphere between 35° S (N) and 80° N (S) during a northward (southward) viewing yaw period with over 1200 vertical profiles measured per day. The L3AT data were interpolated to a latitude-longitude map using data from three consecutive days, using an elliptical Gaussian weight function with major axis aligned in the zonal direction, as in [*Dunkerton and O'Sullivan*, 1996]. N_2O has a ground level source and is destroyed in the stratosphere by photolysis. Its lifetime is approximately one year at 10 mb, increasing rapidly at lower altitudes.

Paper number 97GL01336.
0094-8534/97/97GL-01336$05.00

Results

Figure 1 shows maps of N_2O mixing ratio at 10 mb during November and December, 1992. The polar vortex air has very low N_2O values (dark blue) due to descent within the vortex and its isolation from the extratropics by the polar night jet. The winter mid-latitudes are dominated by the surf zone with large-scale stirring around an anticyclone over the north Pacific and Canada. The tropics have upwelled air rich in N_2O, some of which is drawn northwards over Africa (on this occasion) into the mid-latitude surf zone by breaking Rossby waves [*Randel et al.*, 1993]. Overlaid 10 mb UKMO wind vectors and potential vorticity (PV) contours show the winter polar vortex is disturbed by a developing anticyclone, while there are weak easterlies in the summer extratropics. The quasi-biennial oscillation (QBO) phase is westerly at 10 mb during this period (Fig. 2), a necessary condition for cross-equatorial radiation of quasi-stationary Rossby waves.

Maps of N_2O at 10 mb from the period November 1992 to early January 1993 frequently show patterns associated with Rossby wave radiation across the equator and wave absorption in the southern hemisphere subtropics. A dramatic example of such events occurred over a period of approximately two weeks from late November to early December. The N_2O and PV fields in Fig. 1 show a zonal wave one pattern extending into the tropics from the midlatitudes of the northern hemisphere; e.g., note the strong meridional gradient of N_2O and PV trailing southwestwards from ~40°N, 90°E to about 10°N, 180°W. N_2O also has a strong meridional gradient near 5°S - 15°S at this time which is rearranged by a zonal wave one disturbance whose zonal phase is consistent with its being an extension of the wave one north of the equator. Similarly the tropical region of high N_2O (upwelled air) is wider meridionally in the western hemisphere than in the eastern hemisphere during the time period of Fig. 1, in response to the presence of zonal wave one Rossby wave activity.

Figure 1a shows N_2O and PV at 10 mb on November 20-22, 1992. The N_2O pattern has zonal wave one asymmetry at low latitudes but is relatively smooth at smaller scales. Figure 1b shows a similar view four days later with the tropics dominated by zonal wave one but now with smaller-scale disturbances near the dateline. The agreement between the the smaller-scale N_2O and PV tropical patterns supports the idea that they arise from quasi-horizontal motions associ-

ated with Rossby waves. The clockwise roll-up on the equator near the dateline indicates Rossby wavebreaking is occurring there. South of the equator N_2O's isopleths show rearrangement consistent with incipient wavebreaking, but not of a simple wave one disturbance as there are two developing crests of extratropical air penetrating the tropics. The N_2O pattern near the dateline is consistent with a wavetrain of medium scale waves Rossby waves emanating from the winter subtropics and radiating southwards. Apparently the zonal-wave one's breaking is disturbed by a more localized Rossby wavetrain radiating into the tropics. The localized Rossby wavetrain appears to originate from a positive PV anomaly which was advected around a developing anticyclone over the north Pacific region. The positive PV (low N_2O) anomaly appears in Fig. 1b at 15°-30°N, 150°-180°E. This feature was advected to low latitudes fairly suddenly during the previous 2-4 days; prior to that, air with such low N_2O remained north of ~25°N. Heavy solid lines in Fig. 1b are subjectively placed to indicate the ridge and trough axes of the waves seen in N_2O, while an 'X' marks the probable wavetrain source. From the NE-SW orientation these waves' trough and ridge axes it is clear that the the wavetrain is southward radiating (having northward momentum flux) and the waves are distinct from northward radiating waves which break at southern low-latitudes during southern winter.

Following a five-day data gap as the satellite changed from south viewing to north viewing orientation, Fig. 1c, shows N_2O from Dec 2-4, 1992. The tropics and winter subtropics are still disturbed but less dramatically than in Fig. 1b. Folded isopleths in Fig. 1c show that wave energy reaches to ~20°S. The folds between the equator and 15°S develop little over the next four days, however, other than being sheared westward by the summer hemisphere easterlies, and fade from view after about ten days. The lack of critical line roll-up in these folds indicates that the wave's are behaving approximately linearly at this time, consistent with the waves having slow westward phase speed (~5-10 ms^{-1}). As the wave activity approaches its critical latitude in the summer easterlies the waves' meridional wavelength contracts, as expected from linear wave theory. In Fig. 1c, and during the following week, there are hints of clockwise roll-up motion near 15-25°S, 60-120°E which drifts westwards at about 7-8 ms^{-1}. This represents wavebreaking and absorption of wavetrain energy which probably also occurs at other longitudes but is not easily seen in the mappings. Thus Fig. 1 shows wavebreaking occurring at the equator (Fig. 1b) and near 15-25°S (Fig. 1c) which is distinct from the northern hemisphere's midlatitude wavebreaking zone.

It is difficult to unambiguously identify the characteristics of the Rossby waves crossing the equator: above the 10 mb level (e.g., 6.8 and 4.6 mb) the mixing ratio pattern near the equator is dominated by zonal wavenumber one, while below (14.7 mb) the localized wavepacket nature predominates. It is likely that cross-equatorial radiation of zonal wavenumber one is blocked below 10 mb by unfavorable zonal mean winds in the winter subtropics. Stronger westerly winds in the winter subtropics south of the Pacific sector anticyclone allow the medium-scale wavetrain to radiate southwards even below 10 mb, however.

Map animations from November and December 1992 show that tropical air is regularly stripped from the tropics and mixed to higher latitudes (>10°-15°N or S) by wave breaking in both the northern and southern subtropics, due to Rossby waves from the winter hemisphere extratropics. While tropical detrainment into the winter hemisphere has been observed before, these observations show exchange also occurring on the summer side of the tropics. The case presented indicates that the mixing is bi-directional with summer extratropical air penetrating deep into the tropics, even reaching the equator (near the dateline in Fig. 1c). Tropical air is also seen advected out to 25° S by the wave breaking (100° E, 25° S).

Figure 2 is a latitude-height cross-section of zonal mean N_2O and zonal wind averaged over the same three days as Fig. 1c. The westerly QBO phase at 10 mb and the westerly wind connection to the extratropical westerlies indicates that linear, quasi-stationary extratropical Rossby waves could freely reach the southern hemisphere. The weakened N_2O meridional gradient near 15°S and above about 22 mb in Fig. 2 results from such Rossby-wave radiation. Analysis of N_2O maps at other levels (not shown) indicates the Rossby wave radiation across the equator is confined between about 22 and 3.2 mb. This altitude range is above the QBO westerly maximum (Fig. 2), but coincides with the altitude where there are strong westerlies across the subtropics between the equator and the mid-latitude westerly jet.

Discussion

Rossby waves in the middle stratosphere frequently crossed the equator during early winter 1992-93, when the QBO's phase was weakly westerly there, breaking at the equator and at low latitudes in the summer hemisphere and causing exchange of tropical and extratropical air. Such behavior is consistent with the evolution of the zonal mean wind at 10 mb during this time. Strong zonal mean westerly winds extend south to the tropics from mid-November through mid-December (not shown). The QBO phase near 10 mb is westerly during this period so westerly winds extend across the equator. These conditions are favorable for quasi-stationary, southward radiating Rossby waves to reach the southern hemisphere [*Bowman*, 1996]. During December the winter surf zone matures and a deeper minimum develops in the meridional profile of zonal mean wind, $\overline{u}$, near 30°N with $\overline{u} < 10$ ms^{-1}, versus $\overline{u}$ = 15-20 ms^{-1} during November. This minimum inhibits southward radiation of large-scale extratropical Rossby waves from higher latitudes. A deeper zonal wind minimum implies a more effective filter for equatorward radiating Rossby waves [*Chen*, 1996; *O'Sullivan*, 1997].

Rossby waves should not break and irreversibly decelerate the QBO's core westerlies if the core westerlies are stronger than the zonal wind minimum between the equator and the extratropical westerlies [*O'Sullivan*, 1997]. (For localized medium-scale wavetrains this argument should be modified to consider the westerly wind encountered by the wavetrain on its equatorward path, rather than the zonal mean). The radiating waves should break and be absorbed along the summer subtropical flank of the QBO westerlies and in the winter subtropics, but not at the equator. At intermediate QBO phases, however, during transitions to easterlies for example, the equatorial westerlies may not exceed the subtropical westerly minimum and the Rossby-wave filtering may not shelter the QBO core from wave breaking. During December 1992 the equatorial zonal mean wind was weakly westerly at 10 mb, with maximum

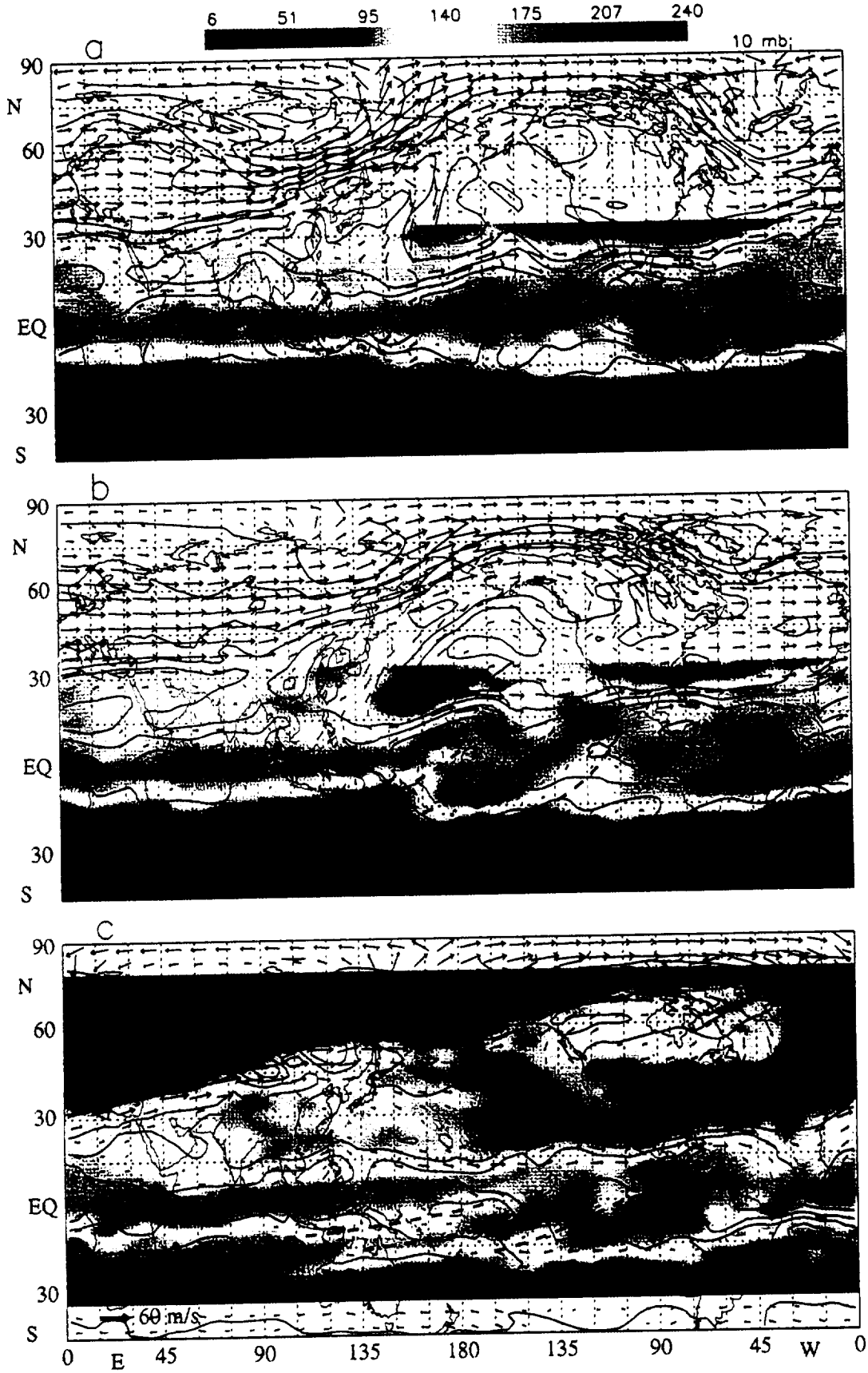

Figure 1. Horizontal map of CLAES N_2O mixing ratio and UKMO PV and wind vectors at 10 mb, using data from (a) November 20-22, 1992, (b) November 24-26, 1992, (c) December 2-4, 1992. Units: ppbv (N_2O) and $7\times10^{-5}Km^2kg^{-1}s^{-1}$ (PV). A bold wind vector representing 60 ms^{-1} is shown in the lower left corner. Heavy dashed lines indicate Rossby wave ridge and trough axes seen in N_2O.

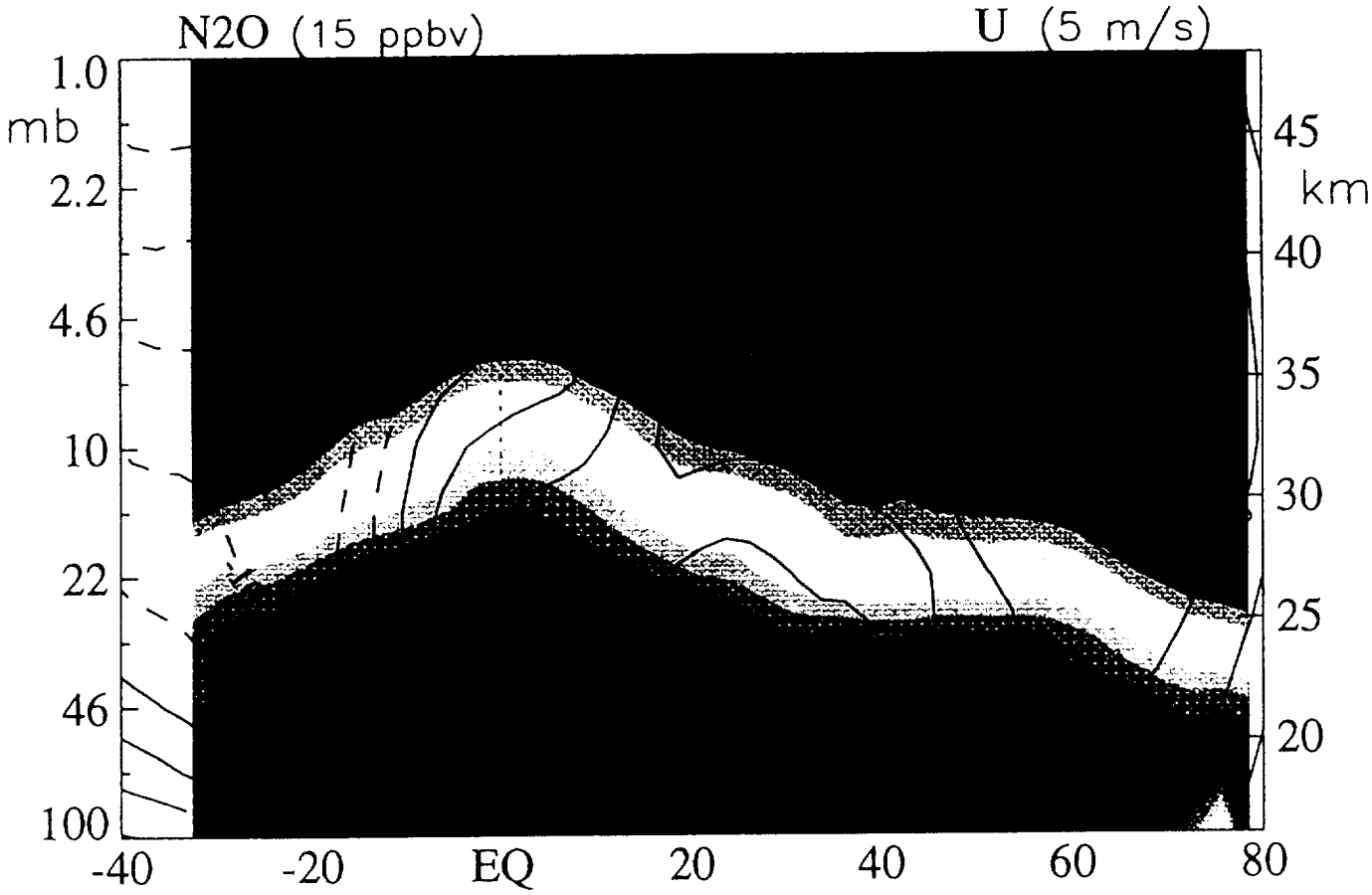

Figure 2. Latitude-height cross-section of CLAES N_2O and UKMO zonal mean wind, averaged over December 2-4, 1992. Contour interval is 15 ppbv (values less than 15 ppbv are darkest blue), and 10 ms^{-1}.

westerlies near 22 mb and increasing easterlies above 6.8 mb (Fig. 2 above, and [*Ortland et al.*, 1996], Fig. 12a). Consistent with this, the presented case (Fig. 1) shows wave breaking mainly occurred at, and south of, the equator at 10 mb and levels below, where the QBO winds are westerly. At the 6.8 mb level (not shown), however, the wave breaking zone expanded northwards, engulfing the equator, consistent with the weak QBO winds. Thus, the breaking of Rossby waves near the equator in the middle and upper stratosphere, with momentum deposition and meridional mixing, are most likely during early winter at levels where the QBO phase is changing from westerly to easterly [*Chen*, 1996]. This work provides observational support for the idea that Rossby waves contribute to the QBO's momentum budget [*Dunkerton*, 1983] at upper levels.

Acknowledgments. This research was supported by NSF grant ATM-9634394 and NASA contract NAS5-32862.

References

Bowman, K. P., Rossby wave phase speeds and mixing barriers in the stratosphere, Part 1; Observations, *J. Atmos. Sci.*, *53*, 907-916, 1996.

Chen, P., The influences of zonal flow on wave breaking and tropical-extratropical interaction in the lower stratosphere, *J. Atmos. Sci.*, *53*, 2379-2392, 1996.

Dunkerton, T. J., Laterally propagating Rossby waves in the easterly acceleration phase of the quasi-biennial oscillation, *Atmos. Ocean.*, *21*, 55-68, 1983.

Dunkerton, T. J., and D. O'Sullivan, Mixing zone in the tropical stratosphere above 10 mb, *Geophys. Res. Lett.*, *23*, 2497-2500, 1996.

Ortland, D. A., W. R. Skinner, P. B. Hays, M. D. Burrage, R. S. Lieberman, A. R. Marshall, and D. A. Gell, Measurements of stratospheric winds by the high resolution doppler imager. *J. Geophys. Res.*, *101*, 10,351-10,363, 1996.

O'Sullivan, D., The interaction of extratropical Rossby waves with westerly quasi-biennial oscillation winds. *J. Geophys. Res.*, in press, 1997.

Randel, W. J., J. C. Gille, A. E. Roche, J. B. Kumer, J. L. Mergenthaler, J. W. Waters, E. F. Fishbein, and W. A. Lahoz, Stratospheric transport from the tropics to middle latitudes by planetary wave mixing, *Nature*, *365*, 533-535, 1993.

Roche, A. E., J. B. Kumer, J. L. Mergenthaler, G. A. Ely, W. G. Uplinger, J. F. Potter, T. C. James and L. W. Sterrit, The Cryogenic Limb Array Etalon Spectrometer (CLAES) on UARS: experiment description and performance. *J. Geophys. Res.*, *98*, 10,763-10,776, 1993.

Swinbank, R., and A. O'Neill, Quasi-biennial and semi-annual oscillations in equatorial wind fields constructed by data assimilation, *Geophys. Res. Lett.*, *21*, 2099-2102, 1994.

D. O'Sullivan, Northwest Research Associates, Inc., P.O. Box 3027, Bellevue, WA 98009-3027. (e-mail: donal@nwra.com)

(Received March 13, 1997; accepted April 14, 1997.)

JOURNAL OF GEOPHYSICAL RESEARCH, VOL. 102, NO. D18, PAGES 21,731–21,743, SEPTEMBER 27, 1997

The influence of the quasi-biennial oscillation on global constituent distributions

Donal O'Sullivan and Timothy J. Dunkerton

Northwest Research Associates, Bellevue, Washington

Abstract. Long-lived stratospheric constituents observed by the Upper Atmosphere Research Satellite are compared between late northern winters 1991-1992 and 1992-1993. The phase of the quasi-biennial oscillation (QBO) was such that the equatorial zonal wind was easterly (westerly) in the lower stratosphere during the first (second) winter. In the tropics, winter-to-winter differences in the latitude-height distribution of zonally averaged N_2O and H_2O are associated with differences in large-scale upwelling, the QBO's mean meridional circulations, and lateral mixing by incident extratropical Rossby waves. In the extratropics, significant differences in zonally averaged N_2O and H_2O are also found which are believed to represent the extratropical constituent QBO. The transport processes creating the extratropical constituent QBO are tentatively identified: In the winter extratropics, QBO modulation of the residual circulation appears to dominate in the upper stratosphere, while QBO-modulated Rossby-wave isentropic mixing dominates below about 10 mbar. Analysis of Rossby waves at low latitudes, as deduced from isobaric constituent distribution maps, suggests that the meridional distribution of Rossby wave breaking depends on the tropical zonal winds. Easterly QBO winds prevent Rossby-wave radiation into the tropics, so that a strong constituent concentration gradient is generated in the winter subtropics. Westerly QBO winds allow some wave radiation into the tropics, accompanied by isentropic mixing in the winter subtropics, cross-equatorial propagation, and occasional mixing in the summer subtropics. These effects depend on altitude and appear to vary in accord with the descending phases of the QBO.

1. Introduction

In the tropics, the zonal mean distribution of long-lived constituents is dramatically altered by the annual cycle, the semiannual oscillation (SAO), and the quasi-biennial oscillation (QBO) [*Gray and Pyle*, 1986; *Zawodny and McCormick*, 1991; *Trepte and Hitchman*, 1992; *Hasebe*, 1994; *Hitchman et al.*, 1994]. The mean meridional circulations associated with these oscillations have upwelling/downwelling in conjunction with easterly/westerly shear layers on the equator. Thus, for example, a westerly SAO shear zone produces a double peak of methane mixing ratio in the upper stratosphere during springtime [*Gray and Pyle*, 1986].

Quasi-biennial variability in constituents or circulation is not nearly as dominant in the extratropics as it is in the tropics, because of the larger interannual, seasonal, and shorter-term variability present there. Nevertheless, the interaction of the QBO with the northern hemisphere extratropics has been documented in both circulation and long-lived constituents; the most active seasons for QBO-extratropical interaction appear to be winter and spring.

The interaction of the QBO and extratropical circulation was first documented by *Holton and Tan* [1980, 1982] who found a robust correlation between the phase of the QBO at 50 mbar and the geopotential height in the north polar region. The relation is such that the December-February polar night jet is stronger during winters when the QBO phase at 50 mbar is westerly. Such QBO-correlated interannual variability of the polar vortex strength is now known as the extratropical QBO. The coupling of the winter extratropical circulation to the QBO apparently occurs through QBO modulation of extratropical Rossby-wave activity, as there is greater Eliassen-Palm flux convergence at middle and high latitudes throughout the stratosphere in the easterly QBO winter composite [*Dunkerton and Baldwin*, 1991; *Baldwin and Dunkerton*, 1991; *Baldwin and Tung*, 1994]. This tendency has also been simulated in numerical models [*O'Sullivan and Salby*, 1990; *Dameris and Ebel*, 1990; *Holton and Austin*, 1991; *O'Sullivan and Young*, 1992; *O'Sullivan and Dunkerton*, 1994; *Butchart and Austin*, 1996; *Chen*, 1996]. Such results imply that extratropical transport of constituents should be modulated by the phase of the QBO, as suggested by *Tung and Yang* [1994a, b] and *Hess and O'Sullivan* [1995].

Paper number 97JD01689.
0148-0227/97/97JD-01689$09.00

Thus the QBO affects tracer transport not only in the tropics but also throughout the winter middle atmosphere. The QBO signal in total ozone has been described using data from the satellite-borne total ozone mapping spectrometer (TOMS) [*Bowman*, 1989; *Lait et al.*, 1989; *Chandra and Stolarski*, 1991; *Randel and Cobb*, 1994; *Tung and Yang*, 1994a]. These data show the dominant influence of the QBO in the tropics where the total ozone anomaly is approximately in phase with the equatorial 30-mbar zonal wind. They also depict an off-equatorial total ozone anomaly which develops in both northern and southern hemispheres during the local winter-spring season, with amplitude and sign depending on the QBO's phase. This seasonally synchronized subtropical and extratropical QBO signal in total ozone maximizes at ~30°-40° latitude, and again at the pole, and is out of phase with the tropical anomaly [e.g., *Randel and Cobb*, 1994, Figure 11].

Studies using vertically integrated total ozone cannot reveal details of the extratropical QBO's vertical structure, however. *Randel and Wu* [1996] used stratospheric aerosol and gas experiment (SAGE) ozone and nitrogen dioxide (over the range ±60° latitude with 1-km vertical resolution) and stressed the importance of the extratropical ozone QBO at middle stratospheric levels (above 30 mbar) in addition to the larger signal at lower levels (below 30 mbar). The extratropical QBO for different constituents depends greatly on the constituent's mean distribution, as this is the basic distribution that the QBO-modulated transport acts upon. Thus to isolate the extratropical QBO signal in constituent transport ideally requires multiyear data sets with vertical and global coverage of constituents which are long-lived at middle and lower stratospheric levels. Unfortunately, such data sets will not be available in the foreseeable future. The Upper Atmosphere Research Satellite (UARS) Halogen Occultation Experiment (HALOE) data may prove useful for this purpose, but the infrequent horizontal sampling by HALOE (about 30 profiles daily) limits its value for studying eddy transport processes.

In this paper, as an alternative to a long-term climatological study, we compare long-lived constituent distributions observed by UARS during its first two northern winters. We note the fortuitous phasing of the QBO, which switched phase by approximately 180° between winters, from a deep easterly QBO phase during the first winter to a deep westerly phase during the second. It is notable that the winter-mean extratropical circulations seen during these two northern winters were similar to the extratropical circulations observed for easterly and westerly QBO composites described above. Thus it is reasonable to suppose that the constituent transport seen during these two winters is also representative of a multiyear QBO composite and that the constituent's winter-to-winter difference is representative of the constituent's extratropical QBO signal. The objectives of this paper are to analyze the UARS observations of long-lived stratospheric constituents in order to determine the QBO's influence on global constituent distributions and to clarify how the QBO modulates transport processes in the tropics and winter hemisphere.

2. Data

The UARS constituents chosen for this study are nitrous oxide (N_2O) observed by the cryogenic limb array etalon spectrometer (CLAES) instrument [*Roche et al.*, 1993; *Roche et al.*, 1996] and water vapor (H_2O) observed by the Microwave Limb Sounder (MLS) instrument [*Barath et al.*, 1993; *Waters et al.*, 1993; *Lahoz et al.*, 1996]. Level 3AT data, consisting of soundings along the orbital track, were used. The CLAES data have a vertical resolution of 2.5 km, while MLS data have about 6-km spacing.

N_2O and H_2O are long-lived constituents in the stratosphere [*Andrews et al.*, 1987, Figure 9.2]. N_2O is destroyed through photolysis and has a lifetime of greater than a year at 10 mbar, and which increases rapidly at lower levels. H_2O is created in the stratosphere from methane oxidation and therefore has a lifetime similar to methane's of about 3 years at 10 mbar and which increases rapidly below. Methane's longer lifetime allows this constituent to act as a source of H_2O in the extratropical upper stratosphere, providing a background concentration gradient that mixing processes can deform. On the other hand, N_2O's shorter lifetime in this region results in nearly homogenized, very low mixing ratio values.

The UARS orbit allows coverage of the stratosphere between 35°S (N) and 80°N (S) during a northward (southward) viewing yaw period. Maps of the L3AT data were made by interpolating to a latitude-longitude grid using data from three consecutive days and an elliptical Gaussian weight function with major axis aligned in the zonal direction, as described by *Dunkerton and O'Sullivan* [1996]. These mappings take advantage of the CLAES and MLS instrument's frequent sampling, providing over 1200 vertical profiles per day. Such mappings capture the slowly evolving features and are particularly successful at lower latitudes where wind speeds are relatively weak. Comparison of maps for successive days shows that most significant features at low latitudes are slow moving and are well represented.

3. Comparison of the First Two Northern Winters of UARS

3.1. Zonal Wind

The evolution of the stratosphere's zonal mean wind at 10 mbar over the first two years of UARS is shown in Figure 1, using United Kingdom Meteorological Office (UKMO) assimilated winds [*Swinbank and O'Neill*, 1994a]. The polar vortex was relatively disturbed during the first winter when the QBO phase was easterly over a deep layer from 60 mbar to near 15 mbar (Figure 2a), while it was relatively quiet during the second winter [*Manney et al.*, 1994, 1995] when the QBO was westerly over a deep layer (from 70 to above 10 mbar). Comparing the two northern winters shows that the polar vortex broke down earlier in 1991-1992 than the fol-

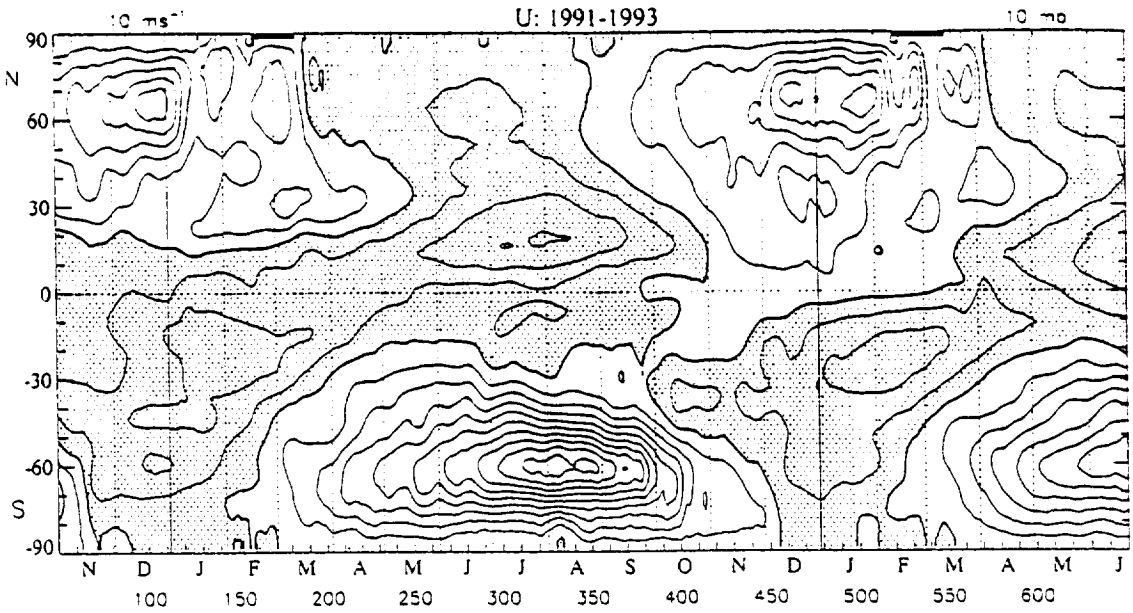

Figure 1. Latitude-time cross section of mean zonal wind at 10 mbar, from United Kingdom Meteorological Office (UKMO) analyses. Contour interval is 5 m s^{-1}, and easterlies are shaded. The bold bars indicate the duration of the northward viewing yaw periods discussed here.

lowing year. In 1991-1992 the vortex broke down in mid-January, whereas in the following year it survived until the beginning of March.

Although the UKMO assimilation provides a good representation of the QBO at most times when compared with Singapore rawinsonde data (Figure 2a) [*Naujokat*, 1986], there is a discrepancy at the 10-mbar level during the first UARS winter, with the onset of the westerly phase at 10 mbar occurring 10 months later in the UKMO analyses than in Singapore rawinsonde observations (Figure 2a), occurring in September 1992 versus November 1991, respectively [*Swinbank and O'Neill*, 1994b]. The UARS high resolution Doppler imager (HRDI) instrument [*Ortland et al.*, 1996, Figure 11] provides independent zonal wind observations and indicates that zonal mean westerly winds near 10 mbar first appear during April 1992. At other times, there is much better agreement between Singapore, UKMO, and HRDI zonal wind observations.

Figure 2b shows the 1992 minus 1993 difference in the zonal mean wind averaged over the months of January, February and March. This corresponds to an "easterly minus westerly" QBO phase difference and shows the dipole pattern associated with Holton and Tan's [1980] extratropical QBO [*Baldwin and Dunkerton*, 1991, Figure 3]. The corresponding difference in geopotential height at 10 mbar (not shown) also gave a pattern similar to that of Holton and Tan [1980] (and Dunkerton and Baldwin [1991]). These results suggest that the QBO is responsible for the extratropical circulation differences between the two northern winters. In the following we will refer to the differing extratropical circulation as the extratropical QBO's dynamical signal. It is, in any case, the signature of a relatively "active" versus "inactive" winter in the northern hemisphere stratosphere.

3.2. CLAES Nitrous Oxide Distributions

To compare the distribution of long-lived constituents between the first two northern winters, we are limited to the time periods when the UARS instruments were northward viewing. This occurred from early December to mid-January and again from mid-February to mid-March of both winters. Unfortunately, only a few days of data are available from the CLAES instrument for the first time period during the winter of 1991-1992, so we concentrate on a year-to-year comparison of constituents during the mid-February to mid-March yaw period. Plate 1 shows the zonal mean N_2O mixing ratio cross section averaged over mid-February to mid-March for both years, along with their difference. The bold horizontal line in the tropics indicates the 27-km (~20 mbar) level which approximately marks the aerosol cloud top in early 1992 [*Lambert et al.*, 1993]. Both winters show the extratropical surf zone between about 20° and 60°N as a region of nearly horizontal isopleths. The polar vortex is evident north of about 60°N in the lower stratosphere as a region of lower N_2O mixing ratio. Both years also show displacement of isopleths due to tropical upwelling and winter extratropical downwelling characteristic of the large-scale Brewer-Dobson circulation. The elevated maximum N_2O mixing ratio in the tropics between 30 and 50 mbar (Plate 1a) is probably an artifact introduced by the Mount Pinatubo aerosol cloud, since the major source of stratospheric N_2O is ground-level emissions from microbiological activity followed by tropical ascent into the stratosphere. At this time the Pinatubo aerosol cloud was dense below about 30 mbar (~26 km) within about 20° of the equator [*Grant et al.*, 1994], so N_2O values in this region may not be accurate. It is unlikely that aerosol lofting could explain the constituent pattern outside of

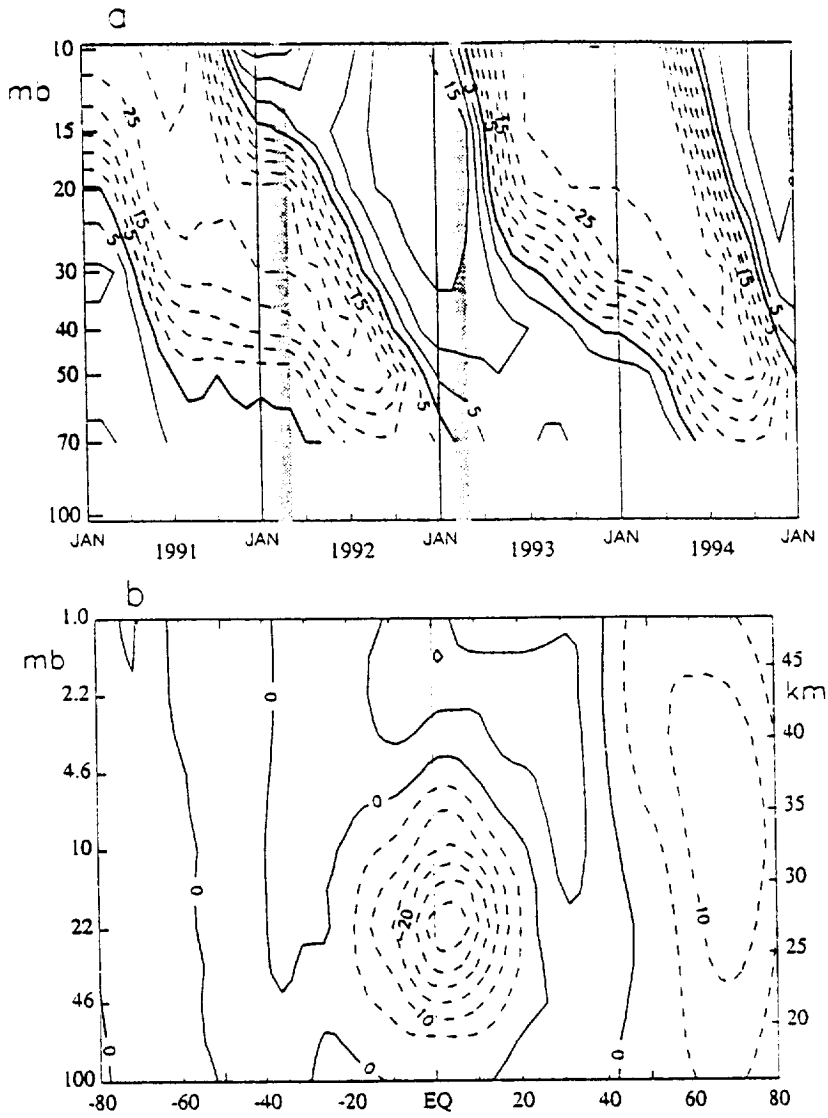

Figure 2. (a) Monthly mean zonal winds at Singapore (1°N, 104°E). Contour interval is 5 m s^{-1} and easterlies are shown by dashed lines. Shading denotes the time periods discussed in this paper. (b) Latitude-height cross-section of the 1992 minus 1993 mean zonal wind difference, averaged over January through March, from UKMO analyses.

the equatorial lower stratosphere, however. As noted by *Dunkerton and Delisi* [1991] in their study of the time period after El Chichon, it is difficult for aerosols to have much direct, long-lasting impact on the mean meridional circulation because (1) the aerosol tends to settle into a shallow layer, implying a small geopotential perturbation for a typical temperature anomaly, and (2) the aerosol spreads horizontally, reducing the latitudinal gradient of heating (which is one of two terms driving the mean meridional circulation). Furthermore, (3) aerosol-induced lofting is accompanied by ozone reduction, which has a buffering effect on the mean meridional circulation [*Kinne et al.*, 1992]. Finally, (4) the magnitude and even the sign of heating rate above an aerosol cloud is not known, so that little can be said about the direct effect of aerosols above the aerosol cloud.

Analysis of CLAES N_2O during January-March 1992 suggests the following. The structure of the tropical maximum (mixing ratio greater than 240 parts per billion by volume (ppbv)) is consistent with transport by the QBO mean meridional circulation as discussed by *Trepte and Hitchman* [1992], given that the QBO zonal wind has a westerly shear layer near 15 mbar according to the Singapore rawinsonde record (Figure 2a). Strong meridional gradients of N_2O develop about the equator near 20° N or S latitude, partly attributable to meridional outflow away from the equator below the westerly shear layer, as discussed by Trepte and Hitchman. Strong vertical gradient of N_2O mixing ratio occurs just above 15 mbar at the equator due to the QBO mean meridional circulation's downwelling in the westerly shear zone.

The marked asymmetry of N_2O mixing ratio about the equator at and above 15 mbar is, however, a major difference between this pattern and the canonical QBO-induced aerosol pattern discussed by *Trepte and Hitchman* [1992]. Transport by the QBO's mean merid-

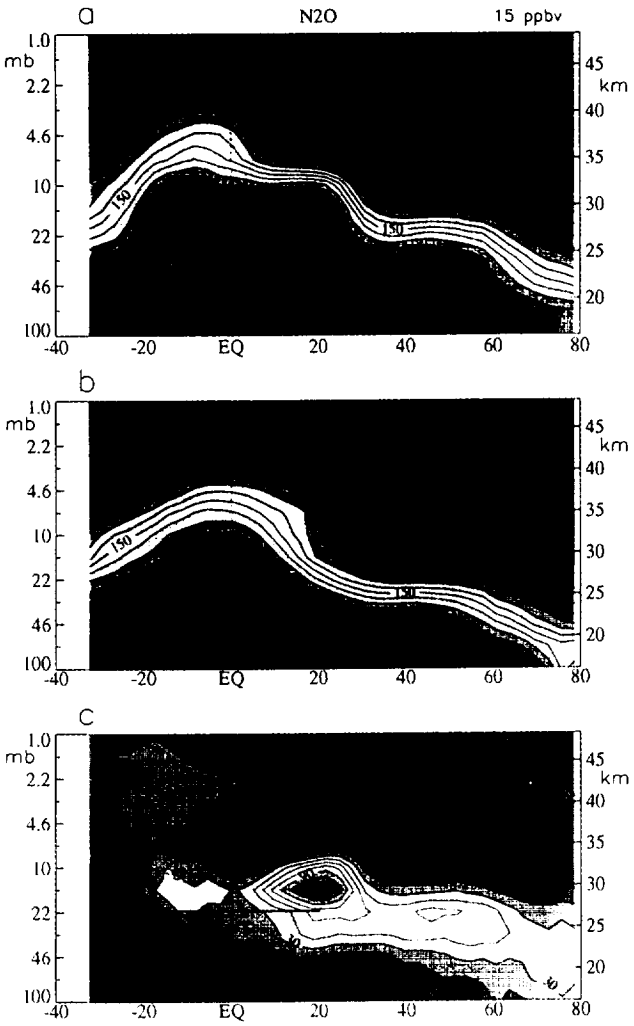

Plate 1. Latitude-height cross-sections of CLAES N_2O, averaged over UARS days (a) 160-185 (February 18–March 14, 1992); (b) 520-550 (February 12–March 14, 1993); and (c) the difference (a) minus (b). Contour interval is 15 ppbv in Plates 1a-1c with the darkest blue representing 0-15 ppbv in Plate 1a and Plate 1b. In Plate 1c negative values are shown by dashed contours, and the bold line denotes the zero isopleth. In the tropics a solid horizontal line indicates 27-km altitude, indicating the approximate top of the Mount Pinatubo aerosol cloud in early 1992.

ional circulations alone would produce a pattern symmetric about the equator. This difference could be due to the different season examined here (late winter) compared with Trepte and Hitchman's cases, which were from early October and early November (see their Figure 3). In our case, the upwelling Brewer-Dobson circulation has become stronger in the summer hemisphere subtropics, tending to elevate the mixing ratio isopleths near 10°–20°S. *Grant et al.* [1996] similarly show equatorial asymmetry about the equator for constituent distributions below 30 km during winter and summer due to seasonally varying upwelling. A second difference is the presence of a strong flux of Rossby-wave activity toward the tropics from the winter extratropics. The propagation and breakdown of these waves, approaching the equator at a particular altitude, depends on the phase of the QBO at that altitude as discussed in section 3.4. A third factor to consider is that the altitude range studied by Trepte and Hitchman was lower than our region of interest, since aerosol concentration is very low above about 30 km.

A year later, in January-March 1993, the QBO has evolved to a nearly opposite phase, with a rapidly descending easterly shear layer near 10 mbar and weaker westerly shear mainly below 50 mbar (Figure 2a). The zonal mean N_2O mixing ratio pattern (Plate 1b) is very different from a year earlier (Plate 1a) at low latitudes, having weaker meridional gradients flanking a central, nearly equatorial peak. The easterly shear layer and upwelling at the equator are centered near 10 mbar, where the mixing ratio isopleths show a more pronounced upward displacement than is seen at altitudes above or below. The asymmetry of the mixing ratio pattern about the equator, above 50 mbar, is mainly due to a stronger meridional gradient in the winter subtropics. This represents the equatorward edge of the winter midlatitude surf zone as it encroaches on the tropics [*Grant et al.*, 1996]. The strongest meridional gradient in the winter subtropics slopes upward and equatorward from ~20°N at 30-40 mbar to ~10°N at 10 mbar. Above 10 mbar the strongest gradient again occurs at ~20°N. This is consistent with HRDI wind observations for March 1993 [*Ortland et al.*, 1996] showing equatorial easterlies reaching to near 20°N above 10 mbar, while westerlies occur below, approximately the reverse of the zonal wind configuration a year earlier. Isobaric synoptic maps of constituent mixing ratios are presented in section 3.4 to help distinguish the transport effects of mean motions from those of eddy mixing.

Comparing the two winters' N_2O distributions indicates that greater large-scale tropical upwelling occurred in February-March 1992 than in February-March 1993. This is indicated in the 1992 minus 1993 mixing ratio difference (Plate 1c) by a positive anomaly in the summer hemisphere's low latitudes above 50 mbar. Similarly, the mixing ratio difference in the winter extratropical upper stratosphere suggests that greater downwelling occurred in 1992, creating the negative difference in the winter extratropics between 30 and 40 km. In the extratropics below 10 mbar, however, it appears that enhanced meridional mixing by Rossby waves during February-March 1992 was the dominant effect. Such differences in long-lived constituent distributions are consistent with the dynamical differences between the two winters. During the 1991-1992 (easterly QBO phase) winter, the more disturbed extratropical circulation would result in a strengthened Brewer-Dobson circulation and greater Rossby-wave mixing compared with the less disturbed 1992-1993 (westerly QBO phase) winter.

3.3. MLS Water Vapor Distributions

In this section we look at water vapor, an independently observed long-lived constituent observed by MLS, for comparison with N_2O. Plates 2a,b present zonal mean MLS H_2O mixing ratio cross sections for

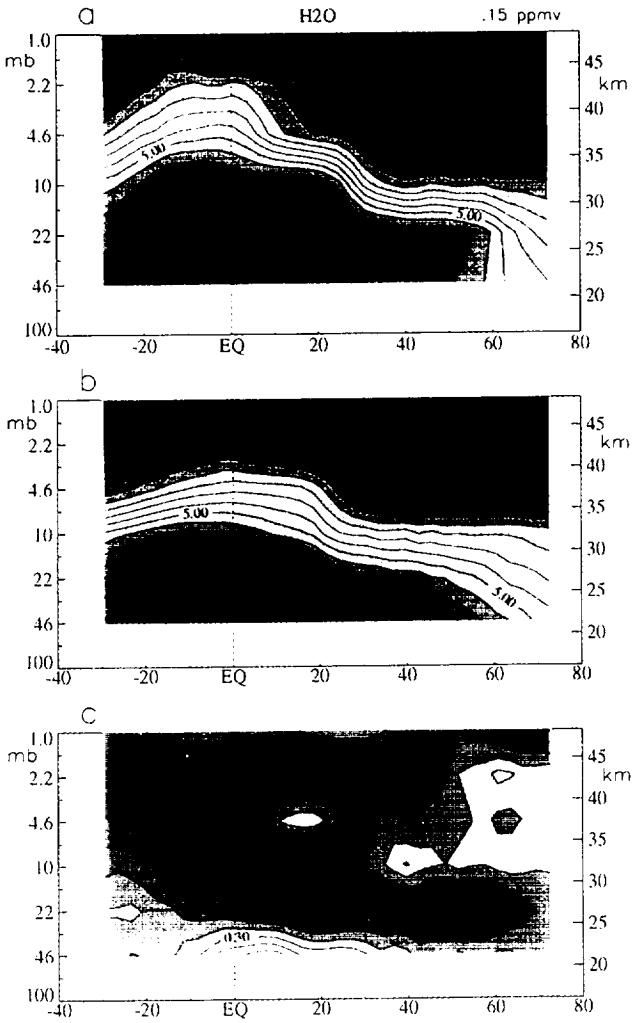

Plate 2. Latitude-height cross sections as in Plate 1 except for MLS H_2O. Contour interval is 0.15 ppmv in Plates 2a-2c, with the darkest blue representing 3.65-3.8 ppmv in Plate 2a and Plate 2b.

the mid-February to mid-March yaw periods of 1992 and 1993, respectively.

There is a strong similarity between the H_2O and N_2O mixing ratio patterns, allowing for their approximately inverted source/sink distribution with height and the poorer vertical resolution of MLS relative to CLAES. Plate 2a shows the stronger tropical upwelling with strong meridional gradients near ~25°N and 20°S, the tropical mixing zone above 10 mbar, downwelling in the winter extratropics and especially within the polar vortex, and the winter midlatitude surf zone. The lower vertical resolution of MLS does not permit the sharp vertical gradient near 10 mbar and 0°–20°N to be resolved as well as by CLAES, however. Methane oxidation increases H_2O mixing ratios with height in the upper stratosphere, so that H_2O shows strong gradients in this region, whereas the N_2O has been mostly destroyed and therefore appears nearly constant. Thus the H_2O mixing ratio (Plates 2a and 2b) highlights the meridional gradient near 5 mbar and 35°N much more clearly than the N_2O mixing ratio (Plates 1a and 1b). The H_2O mixing ratio from 1993 similarly compares well with the N_2O mixing ratio. The main difference between the two constituent distributions is that the H_2O mixing ratio gradients are more uniformly distributed over the domain, although the meridional gradient at the subtropical jet is still clearly evident from ~20°N near 22 mbar to 30°N near 2.2 mbar (Plate 2b). The 1992 minus 1993 difference (Plate 2c) bears a strong similarity to that of the N_2O mixing ratio (Plate 1c), apart from a sign change. The agreement between N_2O and H_2O is remarkable, considering the instrument and species lifetime differences, and increases our confidence in the accuracy of the observations.

As with N_2O, the main features in the winter difference plot can be attributed to transport processes. The tropical mixing zone above 10 mbar in February-March 1992 results in a positive maximum in the H_2O mixing ratio difference near 0°–20°N. Large-scale tropical upwelling, cross-equatorial transport and winter extratropical downwelling above 10 mbar are stronger during the first winter than the second, causing the large region of negative H_2O differences in the tropics and summer low latitudes, with positive difference above 10-15 mbar in the winter extratropics north of about 40°N. Below 10-15 mbar, for example, at 22 mbar, in the extratropics the negative H_2O difference reflects stronger surf zone meridional transport in the first winter. Thus comparing the February-March period between these winters suggests that meridional mixing dominates the zonal mean H_2O mixing ratio tendency below 10-15 mbar while Brewer-Dobson advection dominates above. The longer lifetime of H_2O in the middle and upper stratosphere allows the 1992 minus 1993 H_2O mixing ratio difference to be seen better in the upper stratosphere than was the case with N_2O. Otherwise, despite minor differences, the H_2O mixing ratio winter difference (Plate 2c) resembles the N_2O difference with sign reversed.

3.4. Rossby Wave-Induced Mixing

The striking winter-to-winter variability seen in the zonal mean constituent distribution at low northern latitudes, mirrored in the strong, equatorially asymmetric difference anomaly (Plate 1c and 2c), suggests that QBO-dependent Rossby-wave transport is active in shaping the distributions. To illustrate the importance of Rossby-wave mixing for trace constituent differences between easterly and westerly QBO phase, and their dependence on altitude, we present a few maps of CLAES N_2O in the time periods of interest. Plates 3a and 3b show the distribution of N_2O in early 1992 (UARS days 165-168; February 23-26) at 4.6 and 14.7 mbar, respectively, while Plates 4a and 4b show the corresponding distribution at these altitudes in early 1993 (UARS days 528-530; February 20-23). The days selected from each winter are representative of their yaw periods, and the features we discuss are also evident on other days of each yaw period. One feature immediately apparent is the larger N_2O concentration throughout the tropics in the first winter at 14.7 mbar. This may indicate en-

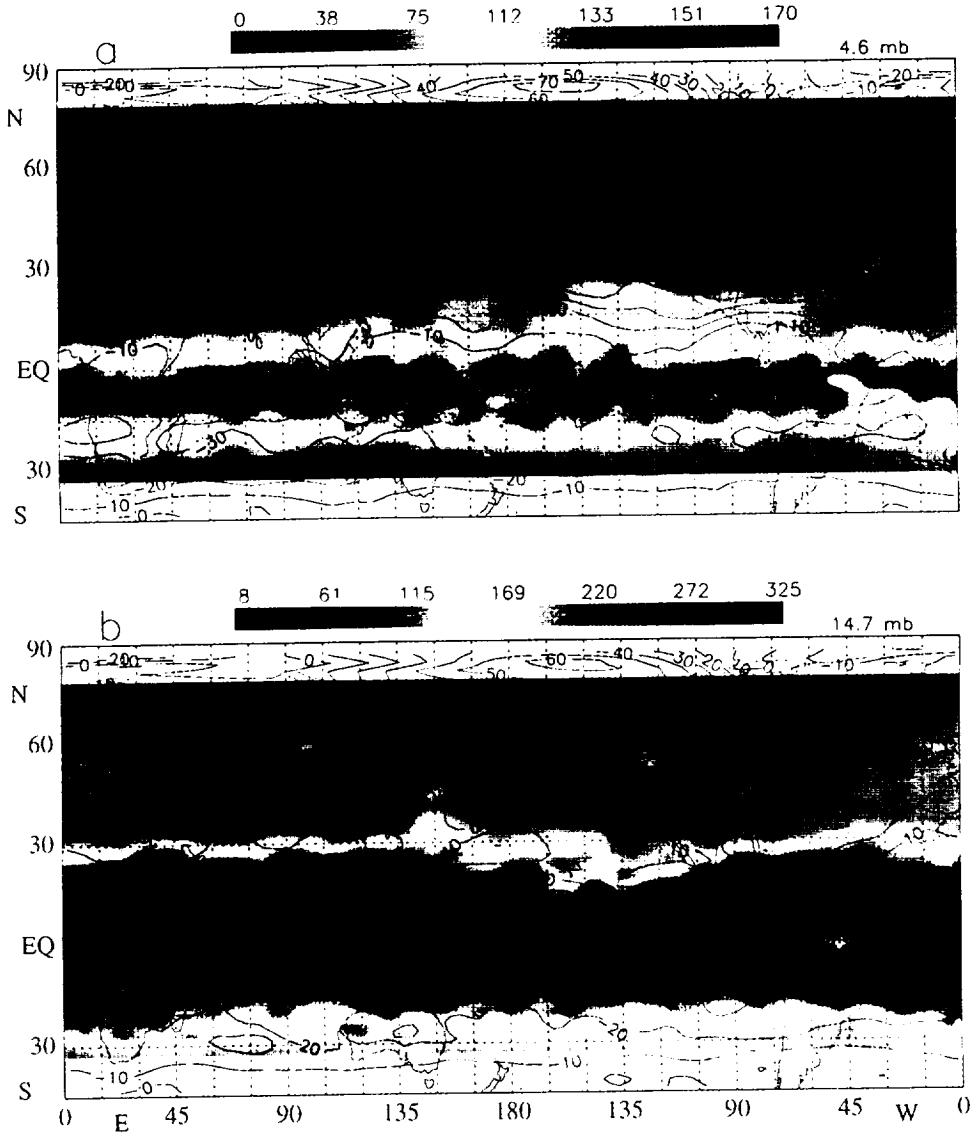

Plate 3. Horizontal map of CLAES N_2O mixing ratio (ppbv) and UKMO zonal wind (m s^{-1}) averaged over UARS day 165-168 (February 23-26, 1992) at (a) 4.6 mbar, and (b) 14.7 mbar.

hanced Brewer-Dobson upwelling, as noted above, since the pattern of increased N_2O in Plate 3b is almost zonally symmetric and unperturbed by Rossby waves. Note that the same color scheme is used in Plates 3a and 4a (4.6 mbar) but that the scheme is altered between Plates 3b and 4b (14.7 mbar) due to the different tropical N_2O concentrations seen at that level in each winter. Several other features in these maps comparing the two years cannot be explained solely in terms of mean meridional transport, however. The data suggest that Rossby-wave propagation and breaking, as modulated locally by the QBO, plays a significant role in shaping the distribution of long-lived constituents in the tropics and subtropics (where our color scheme displays the greatest contrast). In particular, the intensity and location of maximum horizontal N_2O gradient, and the latitude of maximum N_2O concentration, differ significantly between the two winters in a manner consistent with the action of laterally propagating Rossby waves and a local modulation of their propagation and breaking by the QBO winds.

During January-March 1992, Rossby waves are seen to transport N_2O-depleted air quasi-horizontally closer to the equator above about 10 mbar, creating a tropical mixing zone between the equator and 20°N. Isobaric maps of N_2O above 10 mbar show that N_2O is transported to about 10°N on day 165 (Plate 3a) and to about 5°N by day 180 [see *Dunkerton and O'Sullivan*, 1996, Figure 4]. Below 10 mbar, such maps show quasi-stationary Rossby-wave radiation to be nearly completely blocked at about 20°N throughout February and March (Plate 3b). This is presumably due to the QBO zonal wind, which is westerly above 10-15 mbar and easterly below (Figure 2a). Winds observed by HRDI during March 1992 also show strong tropical easterlies below about 10 mbar reaching to about 20°N, while above 10 mbar (to at least 2 mbar) there are weak easterly or westerly zonal mean winds between the equator

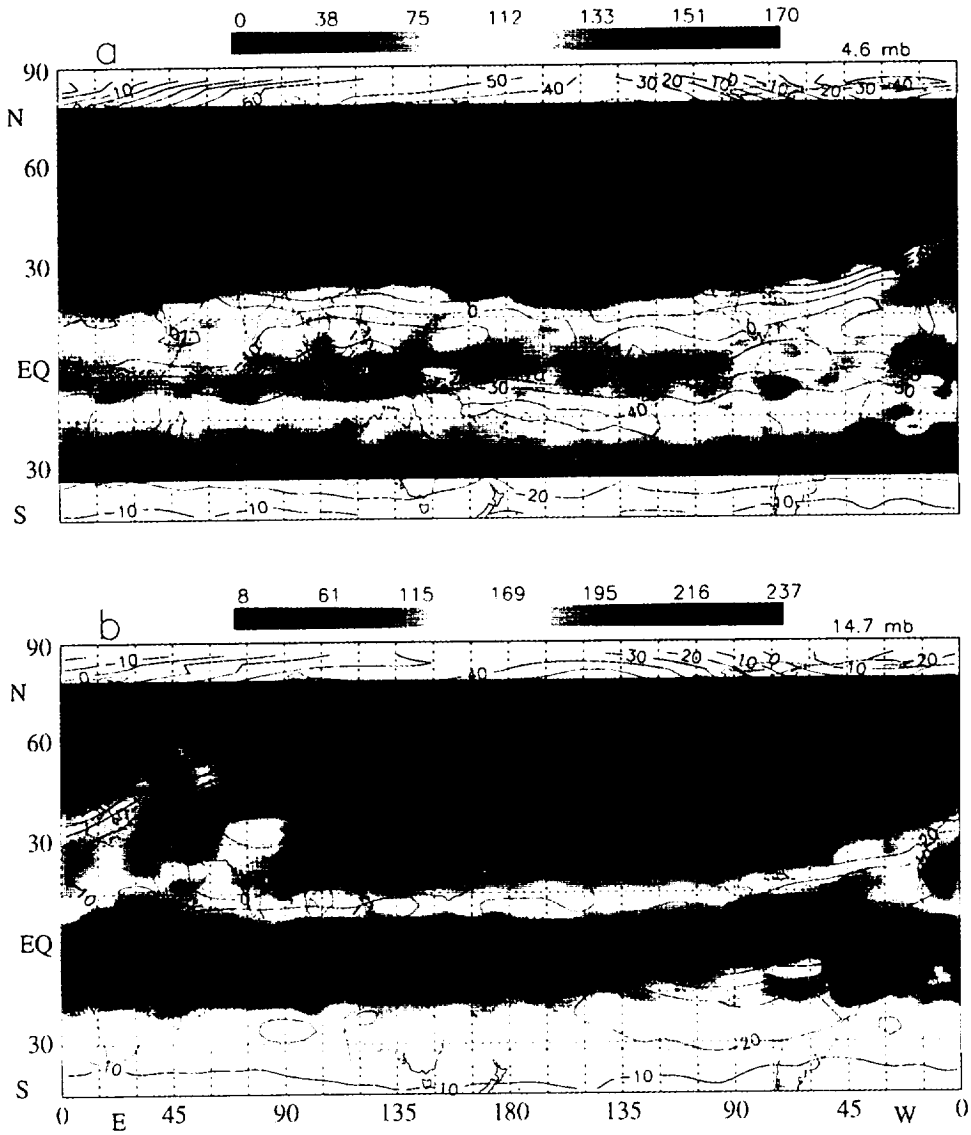

Plate 4. Horizontal map of CLAES N_2O mixing ratio (ppbv) and UKMO zonal wind (m s^{-1}) averaged over UARS day 528-530 (February 20-23, 1993) at (a) 4.6 mbar, and (b) 14.7 mbar. Note the altered color scale between Plate 3b and Plate 4b.

and the extratropical westerly jet (Figure 3a and *Ortland et al.* [1996, Figure 12a]). One effect of Rossby-wave mixing at low latitudes above 10 mbar is the dissipation of the QBO mean meridional circulation-induced peak near 20°N. The equatorward transport and mixing above 10 mbar during February and March was discussed by *Dunkerton and O'Sullivan* [1996].

Examination of isobaric maps of N_2O mixing ratio during late February 1993 indicates that Rossby waves penetrate closer to the equator below 10 mbar, to about 10°N at least, with some evidence of propagation across to the summer hemisphere (e.g., Plate 4b shows the 15-mbar level) while their transport signature is largely confined poleward of ~15°-20°N above 10 mbar (Plate 4a). Such behavior is consistent with linear Rossby-wave theory, which permits the equatorward radiating Rossby waves to propagate until they reach their critical latitude ($\overline{u} = c \sim 0$ in this case). During February and March 1993, QBO easterlies should block equatorward radiating Rossby waves near ~20°N above 10 mbar, (e.g., Figure 3a). Below 10 mbar at this time, however, zonal winds at low latitudes remain weakly westerly in the lower stratosphere according to UKMO wind analyses (not shown) or HRDI observations (Figure 3b). This allows the possibility of Rossby-wave radiation from extratropical westerlies to reach the equator and summer hemisphere [*Chen*, 1996; *O'Sullivan*, 1997].

The propagation of Rossby waves and their irreversible effect on the distribution of a long-lived tracer evidently depend on the local wind distribution as modulated by the QBO. A "westerly over easterly" zonal wind pattern (as occurred in the first UARS winter) allows the possibility of wave propagation into the equatorial zone in the upper, but not lower, levels, while an "easterly over westerly" pattern (as developed in the second winter) prevents equatorial penetration at up-

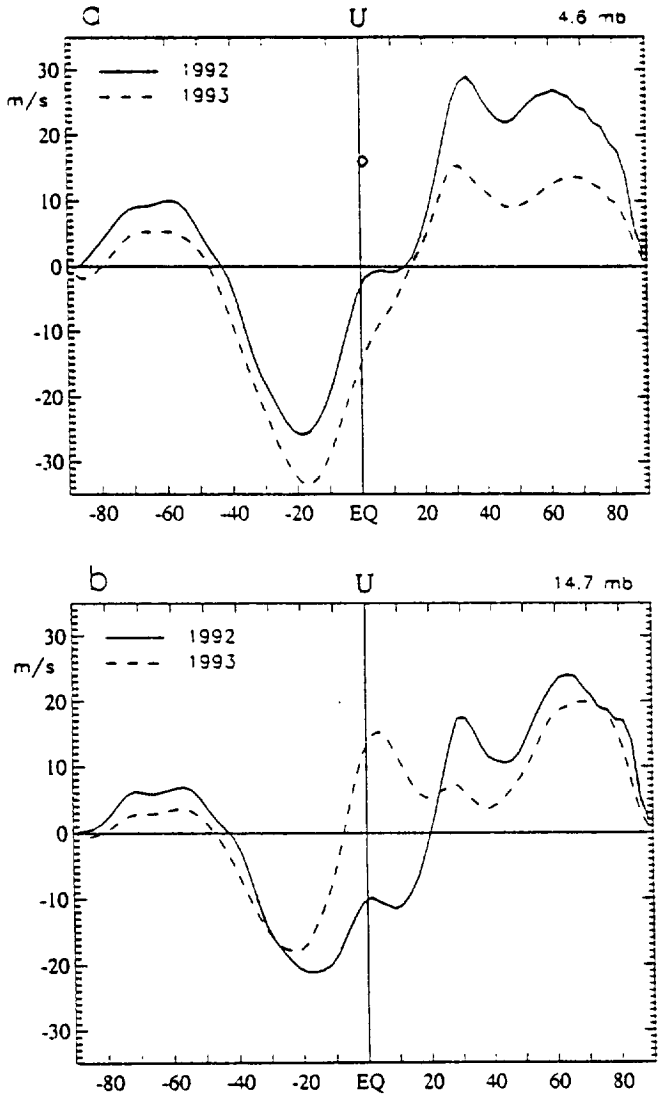

Figure 3. Meridional profile of zonal mean wind at (a) 4.6 mbar, and (b) 14.7 mbar, averaged over the two yaw periods. Winds are from UKMO analyses poleward of 30° and HRDI equatorward of 16°, with a linear transition between. The corresponding 1992 Singapore zonal wind observation in Figure 3a is shown by the diamond.

per levels while allowing a modest amount of isentropic mixing at lower levels of the tropics. The strength and location of the subtropical tracer "barrier" therefore depends on the ability of Rossby waves to penetrate the tropics, irrespective of any remote effect of the QBO on extratropical waves. Not surprisingly, at any given altitude this barrier (e.g., in the region ~10°-25°N) was more diffuse when tropical winds were westerly compared with when they were easterly. Thus, at 4.6 mbar a sharper subtropical gradient is visible in Plate 3b than in Plate 4b, while at 14.7 mbar the subtropical gradient is sharper in Plate 3b than in Plate 4b. *Dunkerton and O'Sullivan* [1996] showed, however, that in the first UARS late winter, the subtropical tracer gradient coincided with the axis of a climatological subtropical jet. The jet axis and tracer gradient tilted poleward with height in the upper stratosphere. There was a second tracer gradient at the equator, associated with QBO westerlies that formed around this time. These features are visible in Plate 3a.

In general, the apparent subtropical "transport barrier" can be viewed as the lateral terminus of a mixing zone. However, there may be more than one reason for such a terminal latitude to appear in the tracer data. On the one hand, Rossby-wave mixing tends to be suppressed in a westerly jet core for reasons discussed by *Dunkerton and O'Sullivan* [1996]. On the other hand, a critical latitude (i.e., critical level where intrinsic phase speed goes to zero) acts as a barrier to mixing because propagation, hence breaking, is precluded beyond this point, or more precisely, beyond the edge of the critical layer. In the first case, mixing does not occur because a critical latitude cannot exist at the jet core for waves able to propagate on the jet, so that mixing is discouraged at the center of the jet. In the second case, mixing does not occur because further wave propagation is precluded by the presence of a critical latitude. The common thread is that significant mixing occurs only in a region of breaking waves, i.e., a critical layer. For quasi-stationary waves which dominate the winter middle atmosphere, the breaking region or "surf zone" occurs poleward of the zero-wind line in a region of relatively weak winds, and is bounded to the north and south either by a westerly jet(s) (equatorial, subtropical, and/or polar) or a region of strong easterlies in which such waves cannot propagate at all.

The tracer distribution in the tropical and subtropical upper stratosphere in the first UARS late winter may be explained in terms of the first mechanism, due to the subtropical westerly jet and formation of QBO westerlies over the equator. At lower levels in the first winter and at upper levels in the second winter, the second mechanism seems more relevant on account of QBO easterlies at the respective altitudes. Latitudinal profiles of mean zonal wind for the two yaw periods in 1992 and 1993 are shown in Figure 3 as obtained from HRDI and UKMO data, together with the point measurement at Singapore. At the upper level in 1992 (Figure 3a), a new westerly jet is beginning to develop near the equator, but the actual maximum value is just shy of zero, unlike the situation at Singapore where typical QBO westerlies have already been attained. There is evidently some zonal variation in the onset of QBO westerlies, such that westerlies first appear near the maritime continent, in the region south-southwest of the Aleutian anticyclone, into which positive potential vorticity (PV) is advected by the prevailing anticyclonic flow. Westerlies are associated with the southern flank of an extrusion of high-PV air and are therefore expected to form in this region as a result of planetary wave breaking. At the upper level in 1993, zonal winds are easterly south of about 15°N, and the subtropical jet is weaker than in 1992. (These results agree with Figure 2b. However, the polar night jet in Figure 2b (January- March average) is weaker in 1992, as expected of the Holton-Tan oscillation, whereas in Figure 3a the jet speed, averaged over the yaw period (mid-February to mid-March), is stronger in 1992. Compared with Figure 1, the polar

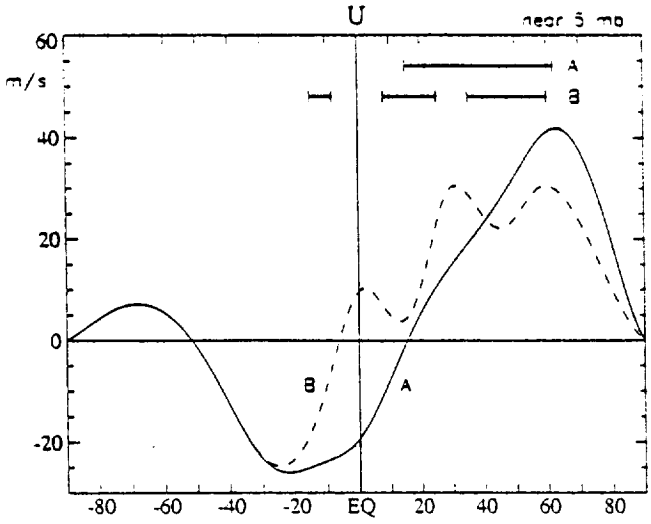

Figure 4. Schematic of the meridional profile of zonal mean wind in the upper stratosphere during late winter, when the quasi-biennial oscillation's phase in the lower stratosphere is westerly (letter A) or easterly (letter B). (Note that the QBO reverses phase between the lower and upper stratosphere.) The solid horizontal lines indicate the extent of distinct meridional mixing zones which may form during late winter (see text for details).

night jet reappeared during the yaw period in late winter 1992, but in 1993, winds were actually at a local minimum during this time. Thus the apparent QBO anomaly in high latitudes in Figure 3a is simply due to the timing of planetary wave events and does not indicate the true extratropical QBO shown in Figure 2b.) At the lower level in 1992 (Figure 3b), the QBO was westerly in 1993, while in 1992 the QBO was easterly, and a new westerly jet was beginning to emerge.

The ability of Rossby waves to penetrate the tropics differs significantly between the two periods shown in Figure 3, at both levels. At the upper level in 1992, stationary waves can radiate across the equator at certain longitudes (e.g., near Singapore), and slowly westward propagating waves can reach the equator at all longitudes. In 1993, all such waves are excluded from the tropics. (The Singapore zonal wind at 35 km in 1993 is -18 m s^{-1} in good agreement with HRDI, -15 m s^{-1}, and there is no evidence of significant zonal asymmetry at this time.) At the lower level the difference in wave propagation is more dramatic, but wave amplitudes at this altitude should be smaller, on average, due to the density effect.

Figure 4 summarizes schematically the contrasting situations observed at upper levels in early 1992 and 1993, which may be taken to represent opposing phases of the tropical QBO in the upper stratosphere in late winter. QBO easterlies at lower levels are accompanied by the formation of QBO westerlies at upper levels. In this case, indicated by letter B, the extratropical QBO signal is such that midlatitude planetary wave activity is enhanced, the polar night jet is weakened, a more pronounced subtropical jet forms, and Rossby waves are able to penetrate the tropics at upper levels. The midlatitude surf zone is divided in half by the subtropical jet, and mixing extends to the equator, the "tropical mixing zone" of *Dunkerton and O'Sullivan* [1996]. In the opposite phase of the QBO, indicated by letter A, planetary wave activity is diminished somewhat by QBO westerlies at lower levels, etc., and propagation of quasi-stationary waves into the tropics at upper levels is entirely prevented by QBO easterlies. In the latter time and place, surf-zone mixing ends close to the zero-wind line. In reality, it is possible that westward moving disturbances are excited in the breaking zone of quasi-stationary waves [*Polvani et al.*, 1995; *O'Sullivan and Chen*, 1996], which may lead to minor mixing equatorward of the zero-wind line, or wherever such waves encounter their critical latitude. The main mixing zones in the upper stratosphere for each winter are indicated in Figure 4 by bold lines. Also included is a mixing zone at low latitudes in the summer hemisphere which can form when the equatorial wind is westerly [*O'Sullivan*, 1997].

4. Conclusions

We have compared the distribution of long-lived stratospheric constituents in the first two northern winters (1991-1992 and 1992-1993) observed by the UARS satellite. In the tropics, these winters were characterized by opposite QBO phases: A deep layer of easterlies dominated the lower stratosphere with westerlies above about 10 mbar during the first winter, and zonal winds were westerly throughout the lower stratosphere during the second winter with easterlies above about 10 mbar.

The behavior of the extratropical circulation during these two northern winters was consistent with the extratropical QBO [*Holton and Tan*, 1980, 1982] whereby the polar vortex is more disturbed and weaker during winters with easterly QBO rather than westerly QBO phase at 40 mbar. This is seen in the January-March average zonal mean wind (Figure 2b) and in 10-mbar geopotential height. It is reasonable, then, to expect that the distribution of long-lived constituents during these two northern winters should also be representative of their QBO composites, if enough years of data were available to obtain such composites.

The main objective of this paper has been to compare the late winter distribution of long-lived constituents, CLAES N_2O and MLS H_2O, between two northern winters with opposite QBO phase in order to reveal how the QBO may be influencing their distribution globally. From the comparison of winters it is concluded that long-lived constituents are affected by the QBO throughout the tropics and winter hemisphere. The winter-to-winter difference of these two independently observed constituents shows a similar mixing ratio pattern, as would be expected if the difference were due to differing transport between winters.

Comparison of the two winters (Plates 1 and 2) shows that transport by mean meridional circulations is affected by the QBO both locally and globally. The local redistribution by the QBO's mean meridional cir-

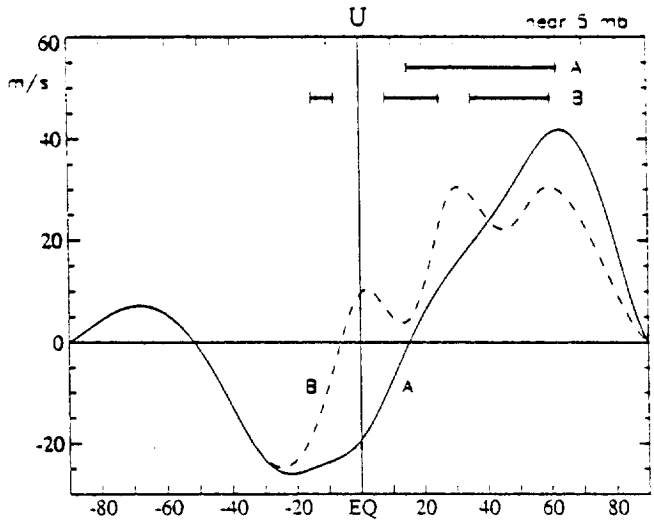

Figure 4. Schematic of the meridional profile of zonal mean wind in the upper stratosphere during late winter, when the quasi-biennial oscillation's phase in the lower stratosphere is westerly (letter A) or easterly (letter B). (Note that the QBO reverses phase between the lower and upper stratosphere.) The solid horizontal lines indicate the extent of distinct meridional mixing zones which may form during late winter (see text for details).

night jet reappeared during the yaw period in late winter 1992, but in 1993, winds were actually at a local minimum during this time. Thus the apparent QBO anomaly in high latitudes in Figure 3a is simply due to the timing of planetary wave events and does not indicate the true extratropical QBO shown in Figure 2b.) At the lower level in 1992 (Figure 3b), the QBO was westerly in 1993, while in 1992 the QBO was easterly, and a new westerly jet was beginning to emerge.

The ability of Rossby waves to penetrate the tropics differs significantly between the two periods shown in Figure 3, at both levels. At the upper level in 1992, stationary waves can radiate across the equator at certain longitudes (e.g., near Singapore), and slowly westward propagating waves can reach the equator at all longitudes. In 1993, all such waves are excluded from the tropics. (The Singapore zonal wind at 35 km in 1993 is -18 m s^{-1} in good agreement with HRDI, -15 m s^{-1}, and there is no evidence of significant zonal asymmetry at this time.) At the lower level the difference in wave propagation is more dramatic, but wave amplitudes at this altitude should be smaller, on average, due to the density effect.

Figure 4 summarizes schematically the contrasting situations observed at upper levels in early 1992 and 1993, which may be taken to represent opposing phases of the tropical QBO in the upper stratosphere in late winter. QBO easterlies at lower levels are accompanied by the formation of QBO westerlies at upper levels. In this case, indicated by letter B, the extratropical QBO signal is such that midlatitude planetary wave activity is enhanced, the polar night jet is weakened, a more pronounced subtropical jet forms, and Rossby waves are able to penetrate the tropics at upper levels. The midlatitude surf zone is divided in half by the subtropical jet, and mixing extends to the equator, the "tropical mixing zone" of *Dunkerton and O'Sullivan* [1996]. In the opposite phase of the QBO, indicated by letter A, planetary wave activity is diminished somewhat by QBO westerlies at lower levels, etc., and propagation of quasi-stationary waves into the tropics at upper levels is entirely prevented by QBO easterlies. In the latter time and place, surf-zone mixing ends close to the zero-wind line. In reality, it is possible that westward moving disturbances are excited in the breaking zone of quasi-stationary waves [*Polvani et al.*, 1995; *O'Sullivan and Chen*, 1996], which may lead to minor mixing equatorward of the zero-wind line, or wherever such waves encounter their critical latitude. The main mixing zones in the upper stratosphere for each winter are indicated in Figure 4 by bold lines. Also included is a mixing zone at low latitudes in the summer hemisphere which can form when the equatorial wind is westerly [*O'Sullivan*, 1997].

4. Conclusions

We have compared the distribution of long-lived stratospheric constituents in the first two northern winters (1991-1992 and 1992-1993) observed by the UARS satellite. In the tropics, these winters were characterized by opposite QBO phases: A deep layer of easterlies dominated the lower stratosphere with westerlies above about 10 mbar during the first winter, and zonal winds were westerly throughout the lower stratosphere during the second winter with easterlies above about 10 mbar.

The behavior of the extratropical circulation during these two northern winters was consistent with the extratropical QBO [*Holton and Tan*, 1980, 1982] whereby the polar vortex is more disturbed and weaker during winters with easterly QBO rather than westerly QBO phase at 40 mbar. This is seen in the January-March average zonal mean wind (Figure 2b) and in 10-mbar geopotential height. It is reasonable, then, to expect that the distribution of long-lived constituents during these two northern winters should also be representative of their QBO composites, if enough years of data were available to obtain such composites.

The main objective of this paper has been to compare the late winter distribution of long-lived constituents, CLAES N_2O and MLS H_2O, between two northern winters with opposite QBO phase in order to reveal how the QBO may be influencing their distribution globally. From the comparison of winters it is concluded that long-lived constituents are affected by the QBO throughout the tropics and winter hemisphere. The winter-to-winter difference of these two independently observed constituents shows a similar mixing ratio pattern, as would be expected if the difference were due to differing transport between winters.

Comparison of the two winters (Plates 1 and 2) shows that transport by mean meridional circulations is affected by the QBO both locally and globally. The local redistribution by the QBO's mean meridional cir-

culation has been previously studied and is evident regardless of season because it is the dominant source of transport variability in the tropics. During the first winter, having a deep easterly QBO phase below about 10 mbar, both N_2O and H_2O (zonally averaged) show a region of weak mixing ratio gradient within about 20° of the equator, at altitudes up to about 10 mbar, flanked by strong meridional gradients The second winter, in contrast, had westerly QBO phase below 10 mbar and shows a narrower, peaked zonal mean mixing ratio distribution centered near the equator with much weaker meridional mixing ratio gradients along its flanks.

The QBO also modulates the large-scale Brewer-Dobson circulation and its associated transport via the extratropical QBO, since the strength of the Brewer-Dobson circulation is closely coupled to the intensity of extratropical Rossby waves. The differing strengths of Brewer-Dobson circulation between winters can be seen in Plates 1 and 2. The circulation is stronger in the more active first winter than in the second. The ascending branch, occurring mainly in the summer subtropics (see Figure 17 of *Dunkerton* [1989]), is stronger in the first winter and elevates mixing ratio isopleths to higher altitudes than the following winter. This is best seen above 10 mbar where the circulation and its winter-to-winter difference are strongest. Variations in the strength of the large-scale meridional circulation are also seen in its descending branch at winter high latitudes, particularly in the upper stratosphere. Plate 2 shows that mixing ratio isopleths at high latitudes in the upper stratosphere are drawn to lower altitudes during the more active first winter, hence the positive H_2O mixing ratio difference above about 15 mbar in the middle and high latitudes (Plate 2c). These effects of the Brewer-Dobson circulation strength are not so evident in N_2O (Plate 1) as they are in H_2O because N_2O's shorter chemical lifetime in the upper stratosphere reduces its interannual variability there, relative to that seen in H_2O.

QBO modulation of extratropical Rossby-wave activity implies that an extratropical QBO signal also exists in isentropic Rossby-wave transport. The observations presented here appear to confirm this, showing greater quasi-horizontal constituent mixing occurring at latitudes poleward of ~30°N in the middle and lower stratosphere below 10 mbar during the first, more dynamically active winter. This causes the positive (negative) difference anomaly in Plate 1c (Plate 2c) in the winter extratropics below about 10 mbar. An alternative explanation for the distribution difference, in terms of different mean vertical transport between winters, seems unlikely, as it would create an extratropical difference having the same sign at all altitudes, given that the vertical gradients of the background constituent mixing ratio do not change sign with height. The quasi-biennial variability of the Brewer-Dobson circulation may explain the constituent variation in the middle and high-latitude upper stratosphere above 10 mbar, however. At an intermediate height, near 10 to 15 mbar, the mean and eddy transport effects apparently cancel for these constituents.

Randel and Wu [1996] examined the vertical structure of the extratropical QBO in using SAGE II ozone. Employing a seasonally varying regression between global ozone and QBO wind, they extracted QBO anomalies during January-March. Aside from the expected tropical ozone QBO anomalies, the regressed anomalies were large only in the winter hemisphere (see their Figure 10). The extratropical ozone anomalies are similar to the long-lived constituent anomalies seen here in latitudinal range but occur at different altitudes. They show two extratropical anomalies, near 10-20 mbar and near 50 mbar, of the same sign, and extending from about 20°N to 60°N, the limit of their data. They attribute the lower extratropical anomaly to vertical displacement, based on the background ozone distribution, while the middle stratospheric anomaly's origin is unknown. The different structure of their extratropical ozone QBO from that seen here in N_2O and H_2O is not surprising, given the very different species lifetimes and background mixing ratios. Ozone has a much weaker meridional mixing ratio gradient in the stratosphere, reducing the effect of isentropic mixing relative to that of N_2O and H_2O.

Finally, the most prominent winter-to-winter differences in N_2O occur between the equator and ~30°N and are attributed to the effect of the QBO winds on wave breaking equatorward of 30°N, as discussed in section 3.4. The frequent sampling of the CLAES and MLS instruments allow "synoptic" maps of N_2O and H_2O to be made, clearly showing that Rossby-wave breaking in the winter low latitudes is influenced by the QBO phase. Plates 3 and 4 show that Rossby waves penetrate closer to the equator when the QBO winds are westerly rather than easterly. Partly as a consequence of this, there is also a weaker constituent mixing ratio gradient between the tropics and extratropics when the QBO winds are westerly rather than easterly. This relationship is consistent with results from numerical modeling of tracer transport under such circumstances [*O'Sullivan and Chen*, 1996]. Thus the distribution of mixing ratio in the tropics appears to be affected by the breaking of Rossby waves incident from the winter hemisphere. In fact, there appears to be evidence of such waves propagating across the equator at 15 mbar during the westerly QBO phase of the second winter. As discussed by *O'Sullivan* [1997], such waves will not break in the QBO westerlies but will instead break on reaching a critical latitude in the summer subtropics. The constituent maps, as well as the zonal mean winter-to-winter differences, support the conclusion that QBO modulation of Rossby-wave transport plays an important role, along with QBO modulated mean meridional transport, in forming the seasonally synchronized, off-equatorial QBO in long-lived constituents.

Acknowledgments. This research was supported by National Science Foundation grant ATM-9634394 and by National Aeronautics and Space Administration contracts NAS5-32862 and NASW-4844. We are grateful to D. Ortland for providing HRDI data and to B. Naujokat for providing Singapore rawinsonde data.

References

Andrews, D. G., J. R. Holton, and C. B. Leovy, *Middle Atmosphere Dynamics*, 489 pp., Academic, San Diego, Calif., 1987.

Baldwin, M. P., and T. J. Dunkerton, Quasi-biennial oscillation above 10 mb, *Geophys. Res. Lett.*, *18*, 1205-1208, 1991.

Baldwin, M. P., and K. K. Tung, Extratropical QBO signals in angular momentum and wave forcing, *Geophys. Res. Lett.*, *21*, 2717-2720, 1994.

Barath, F. T., et al., The Upper Atmosphere Research Satellite Microwave Limb Sounder instrument, *J. Geophys. Res.*, *98*, 10,751-10,762, 1993.

Bowman, K. P., Global patterns of the quasi-biennial oscillation in total ozone, *J. Atmos. Sci.*, *46*, 3328-3343, 1989.

Butchart, N., and J. Austin, On the relationship between the quasi-biennial oscillation, total chlorine and the severity of the antarctic ozone hole, *Q. J. R. Meteorol. Soc.*, *122*, 183-218, 1996.

Chandra, S., and R.S. Stolarski, Recent trends in stratospheric total ozone: Implications of dynamical and El Chichon perturbations, *Geophys. Res. Lett.*, *18*, 2277-2280, 1991.

Chen, P., The influences of zonal flow on wave breaking and tropical-extratropical interaction in the lower stratosphere, *J. Atmos. Sci.*, *53*, 2379-2392, 1996.

Dameris, M., and A. Ebel, The quasi-biennial oscillation and major stratospheric warmings: A three-dimensional model study, *Ann. Geophys.*, *8*, 79-86, 1990.

Dunkerton, T. J., Nonlinear Hadley circulation driven by asymmetric differential heating, *J. Atmos. Sci.*, *46*, 956-974, 1989.

Dunkerton, T. J., and D. P. Delisi, Anomalous temperature and zonal wind in the tropical upper stratosphere, 1982/83, *J. Geophys. Res.*, *96*, 22,631-22,641, 1991.

Dunkerton, T. J., and M. P. Baldwin, Quasi-biennial modulation of planetary wave fluxes in the northern hemisphere winter, *J. Atmos. Sci.*, *48*, 1043-1061, 1991.

Dunkerton, T. J., and D. O'Sullivan, Mixing zone in the tropical middle stratosphere above 10 mb, *Geophys. Res. Lett.*, *23*, 2497-2500, 1996.

Grant, W. B., et al., Aerosol-associated changes in tropical stratospheric ozone following the eruption of Mount Pinatubo, *J. Geophys. Res.*, *99*, 8197-8211, 1994.

Grant, W. B., E. V. Browell, C. S. Long, L. L. Stowe, R. G. Grainger, and A. Lambert, Use of volcanic aerosols to study the tropical stratospheric reservoir, *J. Geophys. Res.*, *101*, 3973-3988, 1996.

Gray, L.J., and J.A. Pyle, The semi-annual oscillation and equatorial tracer distributions, *Q. J. R. Meteorol. Soc.*, *112*, 387-407, 1986.

Hasebe, F., Quasi-biennial oscillations of ozone and diabatic circulation in the equatorial stratosphere, *J. Atmos. Sci.*, *51*, 729-745, 1994.

Hess, P.G. and D. O'Sullivan, A three dimensional modeling study of the extra-tropical quasi-biennial oscillation in ozone, *J. Atmos. Sci.*, *52*, 1539-1554, 1995.

Hitchman, M., M. McKay, and C. R. Trepte, A climatology of stratospheric aerosol, *J. Geophys. Res.*, *99*, 20,689-20,700, 1994.

Holton, J. R. and J. Austin, The influence of the equatorial QBO on sudden stratospheric warmings, *J. Atmos. Sci.*, *48*, 607-618, 1991.

Holton, J. R. and H.-C. Tan, The influence of the equatorial quasi-biennial oscillation on the global circulation at 50 mb, *J. Atmos. Sci.*, *37*, 2200-2208, 1980.

Holton, J. R. and H.-C. Tan, The quasi-biennial oscillation in the Northern Hemisphere lower stratosphere, *J. Meteorol. Soc. Jpn.*, *60*, 140-148, 1982.

Kinne, S., O. B. Toon, and M. J. Prather, Buffering of stratospheric circulation by changing amounts of tropical ozone: A Pinatubo case study, *Geophys. Res. Lett.*, *19*, 1927-1930, 1992.

Lahoz, W. A., et al., Validation of UARS microwave limb sounder 183 GHz H_2O measurements, *J. Geophys. Res.*, *101*, 10,129-10,149, 1996.

Lambert, A., R. G. Grainger, J. J. Remedios, C. D. Rodgers, M. Corney and F. W. Taylor, Measurements of the evolution of the Mount Pinatubo aerosol cloud by ISAMS, *Geophys. Res. Lett.*, *20*, 1287-1290, 1993.

Lait, L.R., M.R. Schoeberl, and P.A. Newman, Quasi-biennial modulation of the Antarctic ozone depletion, *J. Geophys. Res.*, *94*, 11,559-11,571, 1989.

Manney, G. L., R. W. Zurek, M. E. Gelman, A. J. Miller, and R. Nagatani, The anomalous Arctic lower stratospheric polar vortex of 1992-1993, *Geophys. Res. Lett.*, *21*, 2405-2408, 1994.

Manney, G. L., L. Froidevaux, J. W. Waters and R. W. Zurek, Evolution of microwave limb sounder ozone and the polar vortex during winter, *J. Geophys. Res.*, *100*, 2953-2972, 1995.

Naujokat, B., An update of the observed quasi-biennial oscillation of the stratospheric winds over the tropics, *J. Atmos. Sci.*, *43*, 1873-1877, 1986.

Ortland, D. A., W. R. Skinner, P. B. Hays, M. D. Burrage, R. S. Lieberman, A. R. Marshall, and D. A. Gell, Measurements of stratospheric winds by the high-resolution Doppler imager, *J. Geophys. Res.*, *101*, 10,351-10,363, 1996.

O'Sullivan, D. The interaction of extratropical Rossby waves with westerly quasi-biennial oscillation winds, *J. Geophys. Res.*, in press, 1997.

O'Sullivan, D. and P. Chen, Modeling the quasi-biennial oscillation's influence on isentropic tracer transport in the subtropics, *J. Geophys. Res.*, *101*, 6811-6822, 1996.

O'Sullivan, D. and T. J. Dunkerton, Seasonal development of the extratropical QBO in a numerical model of the middle atmosphere, *J. Atmos. Sci.*, *51*, 3706-3721, 1994.

O'Sullivan, D. and M. L. Salby, Coupling of the tropical and extratropical circulations in the stratosphere through planetary wave transport, *J. Atmos. Sci.*, *47*, 650-673, 1990.

O'Sullivan, D. and R. E. Young, Modeling the quasi-biennial oscillation's effect on the winter stratospheric circulation, *J. Atmos. Sci.*, *49*, 2437-2448, 1992.

Polvani, L. M., D. W. Waugh, and R. A. Plumb, On the subtropical edge of the stratospheric surf zone, *J. Atmos. Sci.*, *52*, 1288-1309, 1995.

Randel, W. J., and J. B. Cobb, Coherent variations of monthly mean column ozone and lower stratospheric temperature, *J. Geophys. Res.*, *99*, 5433-5447, 1994.

Randel, W. J., and F. Wu, Isolation of the ozone QBO in SAGE II data by singular value decomposition, *J. Atmos. Sci.*, *53*, 2546-2559, 1996.

Roche, A. E., J. B. Kumer, J. L. Mergenthaler, G. A. Ely, W. G. Uplinger, J. F. Potter, T. C. James and L. W. Sterrit, The cryogenic limb array etalon spectrometer (CLAES) on UARS: Experiment description and performance, *J. Geophys. Res.*, *98*, 10,763-10,776, 1993.

Roche, A. E., et al., Validation of CH_4 and N_2O measurements by the cryogenic limb array etalon spectrometer instrument on the upper atmosphere research satellite, *J. Geophys. Res.*, *101*, 9679-9710, 1996.

Swinbank, R., and A. O'Neill, A stratosphere-troposphere data assimilation system, *Mon. Wea. Rev.*, *122*, 686-702, 1994a.

Swinbank, R., and A. O'Neill, Quasi-biennial and semian-

nual oscillations in equatorial wind fields constructed by data assimilation, *Geophys. Res. Lett.*, *21*, 2099-2102, 1994b.

Trepte, C. R., and M. H. Hitchman, The tropical stratospheric circulation deduced from satellite aerosol data, *Nature*, *355*, 626-628, 1992.

Tung, K.K., and H. Yang, Global QBO in circulation and ozone. Part I: Reexamination of observational evidence, *J. Atmos. Sci.*, *51*, 2699-2707, 1994a.

Tung, K.K., and H. Yang, Global QBO in circulation and ozone. Part II: A simple mechanistic model, *J. Atmos. Sci.*, *51*, 2708-2721, 1994b.

Waters, J. W., L. Froidevaux, W. G. Read, G. L. Manney, L. S. Elson, D. A. Flower, R. F. Jarnot, and R. S. Harwood, Stratospheric ClO and ozone from the Microwave Limb Sounder on the Upper Atmosphere Research Satellite, *Nature*, *362*, 597-602, 1993.

Zawodny, J. M. and M. P. McCormick, Stratospheric Aerosol and Gas Experiment II measurements of the quasi-biennial oscillations in ozone and nitrogen dioxide, *J. Geophys. Res.*, *96*, 9371-9377, 1991.

D. O'Sullivan and T. J. Dunkerton, Northwest Research Associates, Inc., P.O. Box 3027, Bellevue, WA 98009-3027. (e-mail: donal@nwra.com, tim@nwra.com)

(Received March 6, 1997; revised May 21, 1997; accepted June 5, 1997.)

MEAN MERIDIONAL CIRCULATION

JOURNAL OF GEOPHYSICAL RESEARCH, VOL. 103, NO. D8, PAGES 8651–8666, APRIL 27, 1998

Vertical velocity, vertical diffusion, and dilution by midlatitude air in the tropical lower stratosphere

Philip W. Mote,[1,2] Timothy J. Dunkerton,[1] Michael E. McIntyre,[3] Eric A. Ray,[4] Peter H. Haynes,[3] and James M. Russell III[5]

Abstract.

Air passing upward through the tropical tropopause is "marked" by an annually varying water vapor mixing ratio much as a tape recorder marks a magnetic tape; as the air ascends in the tropical stratosphere, these marks are effaced by a combination of vertical diffusion within the tropics and dilution of tropical air by sideways (isentropic) mixing-in of midlatitude air. We represent these processes using a one-dimensional advection-diffusion-dilution model, which we inverse-solve for the vertical profiles of three unknowns (vertical advection velocity, vertical diffusion coefficient, and dilution rate coefficient) after prescribing the vertical profiles of time mean methane $[CH_4]$ and of amplitude and phase of the annually varying tape recorder signal in $2[CH_4]+[H_2O]$. When tested on synthetic data generated by forward solving the same model, the method for inverse solution proved to be well conditioned and to give accurate results above 18 km. Applying the method to 5 years of smoothed data from the Halogen Occultation Experiment, we find a vertical advection velocity with a minimum of about 0.2 mm s^{-1} near 20 km, and both dilution rate coefficient and vertical diffusion coefficient with remarkably low minima near 22 km, 1/(6–7 year) and roughly 0.02 $m^2 s^{-1}$, respectively. Our derived profile of vertical advection velocity agrees well, between 18 and 24 km, with an independent, radiatively derived, mass-budget-constrained transformed Eulerian mean calculation. Despite the relatively modest values of the diffusion coefficient, vertical diffusion plays a significant role in attenuating the tape recorder signal, according to our model. The minimum value of the dilution rate coefficient corresponds to a relaxation timescale of 6–7 years, much longer than the timescales found in other studies. The long relaxation timescale at 20–24 km is, however, consistent with (1) the minimum in vertical velocity, (2) a reduced attenuation rate in the tape recorder signal, and (3) a decrease, hitherto unremarked, in the tropical vertical gradient of $[CH_4]$ there.

1. Introduction

Profiles of water vapor in the tropical lower stratosphere have a vertical structure and time dependence that are determined, to a first approximation, by the ascent of the seasonally varying tropopause-level water vapor mixing ratio [*Mote et al.*, 1995, 1996; *Weinstock et al.*, 1995]. The tropical stratosphere thus resembles a "tape recorder" in that the water vapor content of rising air is "marked" by the seasonally varying saturation mixing ratio that it encountered at the tropical tropopause. These marks are slowly effaced as the air rises but are still discernible at 10 hPa, about 18 months after the air passed through the tropopause. *Mote et al.* [1996] (hereinafter M96) used data primarily from the Upper Atmosphere Research Satellite (UARS) to deduce several relevant aspects of the circulation and thermodynamics of the tropical lower stratosphere: the mean ascent rate between 100 and 10 hPa, some effects of the quasi-biennial oscillation (QBO), some characteristics of tropical troposphere-to-stratosphere mass transfer, and, for the 100 to 46 hPa and 46 to 10 hPa layers, upper bounds on the order of magnitude of vertical diffusion and on that of dilution of tropical air by sideways (isentropic) mixing-in of midlatitude air.

[1]Northwest Research Associates, Bellevue, Washington.
[2]Also at Climate Impacts Group, Joint Institute for the Study of Atmospheres and Oceans, University of Washington, Seattle.
[3]Centre for Atmospheric Science at the Department of Applied Mathematics and Theoretical Physics, University of Cambridge, England.
[4]NOAA Climate Modeling and Diagnostics Laboratory, Boulder, Colorado
[5]Department of Physics, Hampton University, Hampton, Virginia

Paper number 98JD00203.
0148-0227/98/98JD-00203$09.00

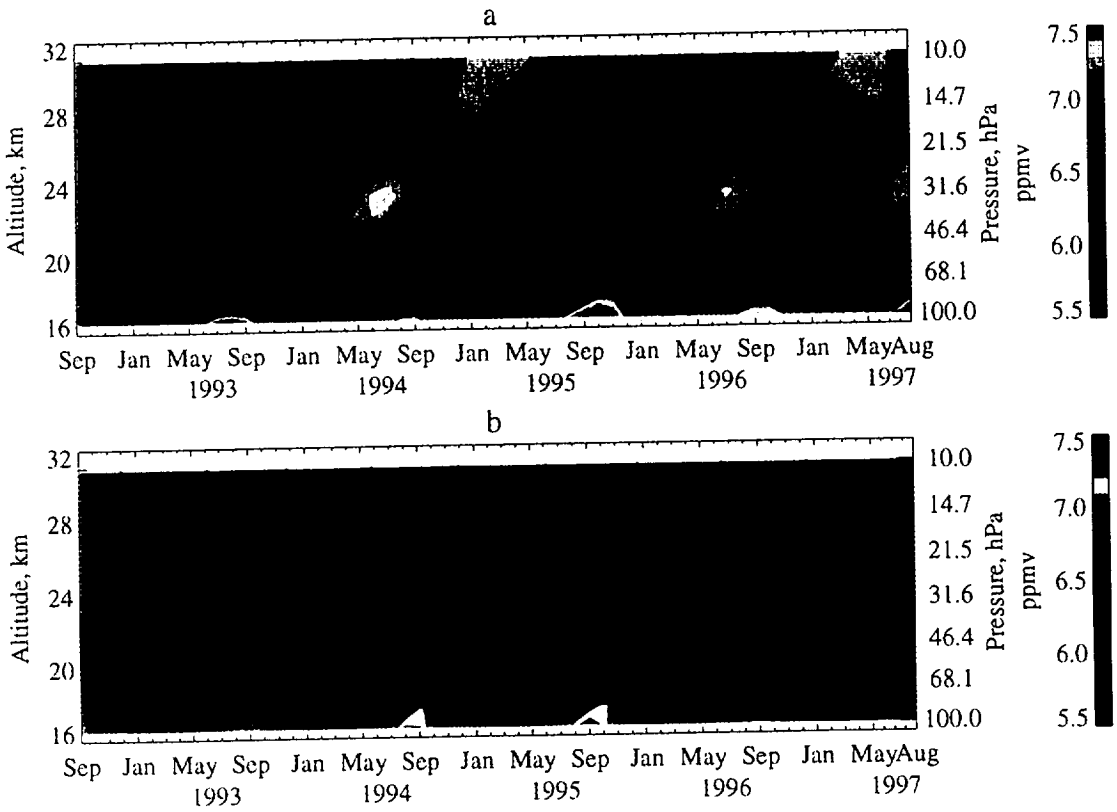

Plate 1. (top) HALOE tropical $\hat{H}$ and (bottom) its reconstruction from the first two EEOFs.

In this article we refine the work of M96 in three ways. First, we calculate extended empirical orthogonal functions (EEOFs) of the tape recorder signal in $2[CH_4]+[H_2O]$; the first two EEOFs are a conjugate pair describing a vertically propagating annual cycle. These two EEOFs and their associated time series are sufficient to reconstruct a smooth time-altitude plot of the tape recorder signal that is a good likeness of the time-altitude plot made directly from HALOE data (Plate 1). Second, by finding the slopes of features (extrema and zero crossings) on the smooth time-altitude plot (Plate 1b), we derive a vertical profile of the ascent rate w_{tr} of marks on the tape. Third, we obtain improved estimates of vertical diffusion and sideways dilution by fitting the profile of w_{tr} and other information in a one-dimensional (1-D) advection-diffusion-dilution model of the tropics. More precisely, the model fitting uses not only w_{tr} but also the amplitude of the tape recorder signal together with the vertical profile of time mean $[CH_4]$. We thus obtain consistent vertical profiles of the vertical advection velocity w (not necessarily the same as w_{tr}), the vertical diffusion coefficient K, and the rate or relaxation coefficient α for dilution by middle-latitude air. The results indicate that in the altitude range from about 18 to 24 km, w_{tr} is close to the vertical advection velocity w, implying that for those altitudes the tape recorder signal can be taken at face value as a good indicator of mean vertical motion. The extraction of all three vertical profiles $w(z)$, $K(z)$, and $\alpha(z)$ is a well-conditioned, hence credible, calculation only because water vapor, with its high information content concerning the annual cycle, is used simultaneously with a long-lived trace gas, in our case $[CH_4]$.

Several other efforts have recently been made to characterize the exchange of air between tropics and middle latitudes. Some focused on mixing out from the tropics to middle latitudes by advecting passive tracers using observed winds [*Chen et al.*, 1994; *Waugh* 1996], while others considered 1-D budgets of observed long-lived trace gases, thus focusing on dilution of tropical air by mixing in from middle latitudes [*Avallone and Prather*, 1996; *Minschwaner et al.*, 1996; *Volk et al.*, 1996]. *Remsberg and Bhatt* [1996] used the zonal variance of nitric acid to infer the (qualitative) altitude dependence of dilution. In a different approach, *Schoeberl et al.* [1997] related dilution to the phase lag between water vapor mixing ratios and QBO winds. *Hall and Waugh* [1997b] independently derived average lower stratospheric values for w, K, and $1/\alpha$ using the tape recorder signal in $2[CH_4]+[H_2O]$ and a long-lived trace gas with a secularly increasing trend (sulfur hexafluoride). Our study differs from those just cited in that it simultaneously derives vertical velocity, vertical diffusion, and dilution rate coefficient as functions of altitude between 100 and 10 hPa, leading to a clear picture of the vertical structure of each of these three quantities.

2. Data

The constituent (CH_4 and H_2O) data used in this paper come from the Halogen Occultation Experiment (HALOE) aboard UARS. M96 used version 17 data

ending July 1995; here we use version 18 data between September 1992 and August 1997. Time series are formed from monthly means, each comprising all tropical soundings for the month. We define the tropics as 14°S to 14°N, broad enough to include a greater number of profiles while still within the well-mixed region bounded by the subtropical mixing zones. Following M96, we use the quantity $\hat{H}=2[CH_4]+[H_2O]$, which has the advantage of being nearly conserved and homogeneous in the extratropical stratosphere, because photochemical breakdown of 1 mol of $[CH_4]$ produces approximately 2 mol of water vapor.

The vertical resolution of the data is the same as in M96 and is finer than that usually used (e.g., *Randel et al.* [1998]). HALOE level 2 data (where "level" refers to the level of processing) are available on a 0.3-km grid and are here interpolated to pressure levels 100.0, 82.5, 68.1,... hPa with a fractional spacing of $10^{1/12}$ in pressure. These pressure levels were converted to geopotential height using data from the U.K. Meteorological Office (UKMO) analyses [*Swinbank and O'Neill*, 1994], which form part of the UARS database. The spacing between HALOE pressure levels ranges from about 1.1 to 1.3 km.

3. Methods

3.1. Extended EOF Analysis

Plate 1a updates Plate 1b of M96 with about 2 more years of data. While the general sense of rising moist and dry anomalies is apparent, we wish to isolate the phenomenon of rising anomalies from other phenomena; to do this it will prove useful to apply a statistical technique known as extended EOF analysis [*Weare and Nasstrom*, 1982, *Wang et al.*, 1995].

Empirical orthogonal functions can identify coherent variations in noisy data by finding eigenvectors of the covariance matrix. In the case of tropical HALOE data, measurement noise is exacerbated by the sparse sampling that is characteristic of occultation techniques; EOF analysis can be performed using each month's profile to yield a clearer picture of vertically coherent variations. If the covariance matrix is formed by calculating covariance not of a single profile at each time but of several profiles at different lag times (in this case between −6 and +6 months), the resulting "extended EOF analysis" (EEOF analysis) yields a clearer picture of both vertically and temporally coherent variations.

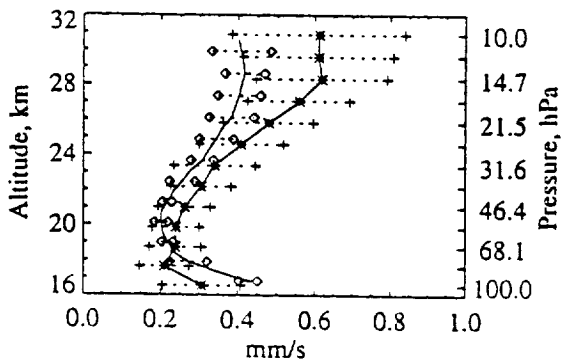

Figure 1. Profiles of time mean ascent rate w_{tr} (plain curve) of the tape recorder signal, and the vertical velocity $\bar{w}^*$ calculated by Rosenlof (curve with asterisks), with $\pm 1\sigma$ bars (diamonds for w_{tr}, plus symbols for $\bar{w}^*$).

Table 1. Definitions of Various Vertical Velocities

Term	Definition
w	true vertical velocity†
$\bar{w}^*$	vertical velocity calculated by Rosenlof
w_{tr}	ascent rate of marks on the tape
$\tilde{w}$	$\equiv w + (K/H) - K_z$
w_{synth}	like w_{tr} but for synthetic $\hat{H}$ data

†used in 1-D model

We perform EEOF analysis on the HALOE $\hat{H}$ data shown in Plate 1a, yielding a 4-year time series of coefficients since 6 months have been lost at each end. The first two EEOFs have a strong annual cycle and together they account for 68% of the variance. The next two EEOFs vary interannually and explain 17% of the variance. The coefficients of the first two EEOFs, when plotted against each other, trace nearly perfect circles with a period of one year, indicating that they are a conjugate pair. The coefficients of the next two EEOFs trace somewhat less than two orbits in 4 years, similar to the singular value decomposition results shown by *Randel et al.* [1998] for $[CH_4]$.

With the coefficients of the first two EEOFs, multiplied at each time by the zero-lag profile of the EEOFs (and the missing 6 months at each end filled in by the EEOFs at lag $\pm 1, \pm 2, \ldots \pm 6$), we construct an altitude-time plot of $\hat{H}$ anomalies (Plate 1b). When compared with the altitude-time plot of HALOE $\hat{H}$ data (Plate 1a), the first two EEOFs produce almost a pure annual cycle. In the resulting picture, ascending minima and maxima of $\hat{H}$, which are formed at the tropopause, retain their identity from the tropopause to 10 hPa (about 31 km).

From the tape recorder signal (for example, as represented smoothly in Plate 1b), two quantities can be deduced directly, both as functions of altitude: w_{tr}, the ascent rate of marks on the tape, and A, the amplitude of the signal. Both quantities depend on altitude. In the next subsection we consider A. The quantity w_{tr} (Figure 1) was obtained from the data in Plate 1b by following each ascending minimum, maximum, and zero from level to level on successive time series plots. Also shown in Figure 1 for later comparison is a transformed Eulerian mean vertical velocity $\bar{w}^*$ obtained by K. Rosenlof (personal communication, 1996), updating that of *Rosenlof* [1995]. (In section 5.2 we discuss whether we expect w_{tr} and $\bar{w}^*$ to be equal. Table 1 summarizes the definitions of these quantities.)

Rosenlof has recalculated $\bar{w}^*$ making use of more UARS data in the radiative calculation, and the agreement between her new $\bar{w}^*$ (the curve marked by asterisks in Figure 1) and our w_{tr} is excellent, at least between 19 and 24 km. The standard deviations are

calculated for 12 monthly profiles of $\bar{w}^*$, hence reflecting mainly seasonal variation, and are calculated for 20 separate features (extrema or zero-crossings of $\hat{H}$) for w_{tr}, hence reflecting both uncertainty in our method of calculating w_{tr} and possibly seasonal and interannual variation.

3.2. Definition of Amplitude

Underlying the model-fitting concept to be used here is the tentative assumption that the pattern seen in Plate 1 is "typical" in the sense that, if previous or subsequent years were visible, one would see a very similar pattern, i.e., something like the periodic extension of Plate 1 in both time directions. To the extent that this is justified, one can talk about "the annual cycle," and by implication its amplitude and phase, with less ambiguity than is strictly the case with a record only 5 years long. With this point in mind, we seek to define the amplitude and, in section 3.3, the phase.

As was already mentioned, we use $\hat{H}$ as the basis for estimating the amplitude A of the tape recorder signal. Variations in $\hat{H}$ are due almost solely to the tape recorder signal, while $[H_2O]$ is more strongly affected by other kinds of variability such as the QBO or the semiannual oscillation (SAO). Indeed, we find that the variance of $[H_2O]$ exceeds that of $\hat{H}$ above 25 km. Other sources of variability that might affect our estimation of A include the HALOE sampling pattern, instrumental or retrieval errors, or incursion of the subtropical barrier into the tropical region (14°S to 14°N). Such variability can be reduced by the use of EEOFs, since the EEOF technique identifies coherent variations.

Because of the variation in vertical velocity caused by the QBO, the temporal variations in $\hat{H}$ become slightly distorted, with extrema shifted as much as 2 months away from a perfect 12-month period [M96]. Consequently, taking the mean annual cycle or applying Fourier analysis at each level independently (as was done by *Randel et al.* [1998]) may underestimate the tropopause-related variance above 20 km or so. Similarly, EEOF analysis links variations at different altitudes so that the stretching and compressing of the tape recorder signal by the QBO [M96; *Cordero et al.*, 1997] would be smeared out a bit, possibly leading to an underestimate of the variance associated with the tape recorder signal. In contrast to the mean annual cycle, however, the coefficients of the first two EEOFs have a small degree of interannual variability, allowing for some QBO effects on the tape recorder signal. We therefore expect that an amplitude definition based on EEOF analysis will be more successful than other definitions in distinguishing between variations originating at the tropical tropopause and variations arising from other sources.

With those considerations in mind, we present plots (Figure 2) of the logarithm of amplitude defined in several ways, all but one using $\hat{H}$. Since only derivatives of $\ln A$ will be needed, the curves have been normalized by their amplitude at 100 hPa in order to emphasize their differences. Curve *a* shows the standard deviation, at each level, of the time series of $\hat{H}$ (Plate 1b, the EEOF reconstruction). Curve *b* is the annual harmonic from fast Fourier transform analysis of monthly mean HALOE data (Plate 1a). Curve *c* is based not on HALOE $\hat{H}$ data but on time series of tropical water vapor measured by the Microwave Limb Sounder (MLS) aboard UARS (see M96 for details). Curve *d* is obtained by first removing a 12-month running mean from the data in Plate 1a, then following individual maxima and minima upward, and taking the difference between the average maximum and the average minimum at each level. Curve *e* is the standard deviation of the time series at each level in Plate 1a ($\sigma(\hat{H})$). Finally, the solid curve with plus marks is the peak-to-peak amplitude of the seasonal cycle, composed of the annual and semiannual harmonics of $\hat{H}$, as derived by *Randel et al.* [1998] for the latitude range 4°S to 4°N on a subset of our levels.

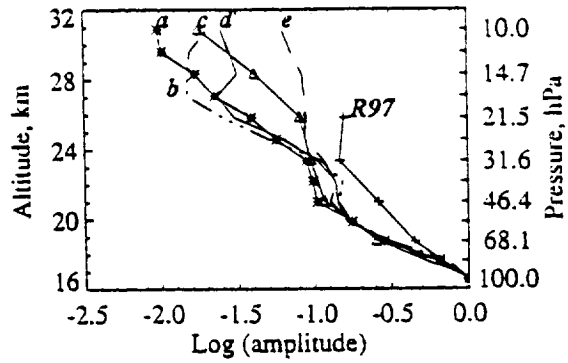

Figure 2. Amplitude of the tape recorder signal defined various ways (curves a–e); see text for details.

By most definitions, the amplitude decreases monotonically with altitude, but all show a region of near-constant A (a "cliff") somewhere between 20 and 25 km. The total attenuation from 100 to 10 hPa is greatest for curve *a* and least for curve *e*, with curves *b*–*d* clustered near the mean of these two extremes. Our amplitude curves differ from that of *Randel et al.* [1998], probably because the narrow latitude range they chose (4°S – 4°N) results in far fewer good data points (especially at 100 hPa, where noise levels are high) and a less coherent annual signal.

For calculating first and second derivatives, it will be useful to have a smooth approximation $\ln f$ for $\ln A$. As was outlined above, we expect the curve based on EEOFs, curve *a*, to provide the best definition of amplitude, and we fit smooth curves f to it and also to curve *d* in order to bracket the reasonable range of definitions of f. The data suggest that vertical attenuation rates are relatively fast at upper and lower levels of the domain, and relatively slow in the middle (near 20–23 km). It is not clear, however, how steep the cliff in the middle should be. One possibility is that the cliff is spurious. Another possibility is that the cliff is real and reflects a sharp decrease of attenuation rate in the middle layer, as might be expected in the lower part of the QBO for dynamical reasons [see *Dunkerton*, 1997].

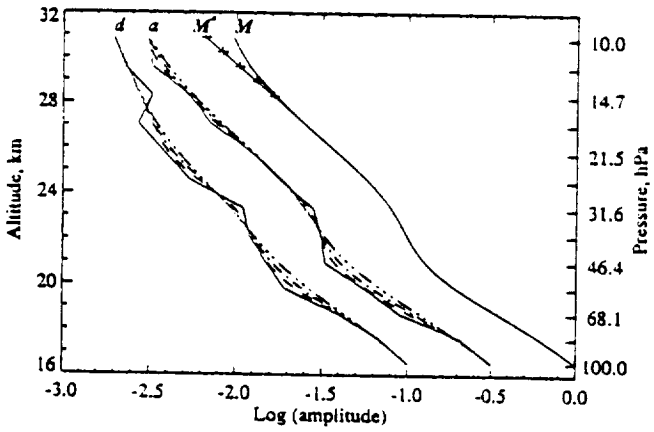

Figure 3. Profiles of variously smoothed versions of curves a and d of Figure 2, the smoothing performed as described in the text. Curve M is the same as the dash-dotted version of curve a; see text for definition of M^*. Curves have been shifted left for clarity.

We smooth the amplitude curves by first linearly interpolating them to high (approximately 70 m) vertical resolution, then applying a 1-2-1 filter to the second derivative 200, 500, or 1000 times, and finally inverting (integrating twice) to yield a set of curves f (Figure 3) with a range of behavior near the "cliff." Smoothed 1000 times, the cliff almost disappears in both cases. The curve labeled M is curve a smoothed 500 times, while curve M^* was obtained by constraining the attenuation rate to a constant above the cliff (for reasons described in section 3.4). The various curve fits provide a range of profiles spanning the uncertainty of the original estimates of A, thereby generating a range of values for w, α, and K.

3.3. One-Dimensional Model for Analysis

In order to derive vertical profiles of α and K, we assume that to within reasonable noise levels, the smoothed and meridionally averaged tropical data can be fitted to solutions of the simple one-dimensional advection-diffusion-dilution model

$$\chi_t + w\chi_z = \frac{1}{\rho}(\rho K \chi_z)_z - \alpha(\chi - \chi_{ML}) + S \qquad (1)$$

where χ is a tracer mixing ratio, w is the vertical velocity, K is the vertical diffusion coefficient, $\rho = \rho_0 \exp(-z/H)$ is the mean density profile with $H = 7$ km, α is the dilution rate, χ_{ML} is the midlatitude value of χ, and S is a chemical source-sink term (of the form $-\gamma\chi$ for $[CH_4]$, 0 for $\dot{H}$). Partial derivatives with respect to time t and height z are indicated by subscripts.

Implicit in this model are several assumptions. (1) Tropical air is horizontally homogeneous within well-defined latitude limits (here, 14°N to 14°S) and is distinct, though not completely isolated, from midlatitude air. (2) The same values of w, K, and α apply to both $[CH_4]$ and $\dot{H}$ (see *Thuburn and McIntyre* [1997], for a discussion of this assumption). (3) As is commonly done [e.g., M96; *Volk et al.*, 1996], we assume dilution by midlatitude air on a given level to be a linear relaxation process in which tropical air tends toward the midlatitude mixing ratio χ_{ML} with relaxation rate α and with zero phase lag. In fact, the seasonal cycle of water vapor (hence $\dot{H}$) in the lower stratosphere (below 20 km) at middle latitudes is strongly influenced by the tropical seasonal cycle, presumably by mixing out, with a phase lag of a month or two [e.g., *Mastenbrook and Oltmans*, 1983; *Rosenlof et al.*, 1997]. This means that especially below 20 km the assumption of uniform extratropical $\dot{H}$ fails, and dilution is a much more complex process than is assumed here.

With these caveats in mind, we first rewrite (1) as

$$\chi_t + \tilde{w}\chi_z = K\chi_{zz} - \alpha(\chi - \chi_{ML}) + S \qquad (2)$$

where

$$\tilde{w} \equiv w + (K/H) - K_z \qquad (3)$$

arises when we expand the diffusion term in (1). Note that $\tilde{w}$ does not have a physical meaning but is introduced for mathematical convenience. Some of the advective effects of diffusion are represented in $\tilde{w}$; later we compare the variants of w listed in Table 1.

One usually solves differential equations like (2) for the dependent variable, in this case χ, but we want to find the three unknowns $\tilde{w}$, K, and α, through a process that could be called "inverse solving." There are a few possible methods for inverse solving (2) for the three unknowns. After testing these methods on synthetic data that were constructed (as is explained in the next section) from known profiles of $\tilde{w}$, K, and α, we chose one method that is both accurate and concise. (Another method, involving WKBJ or slow modulation theory, is outlined in Appendix A and will prove useful in sections 3.4 and 3.5.) Our method makes use of information about $[CH_4]$ and $\dot{H}$; specifically, we represent $\dot{H}$ anomalies by the functional form $\chi = \mathrm{Re} f(z) \exp[i(\phi(z) - \omega t)]$, where $f(z)$ and $\phi(z)$ are real and are determined from $\dot{H}$ data and where the midlatitude value of $\dot{H}$ is assumed to be spatially and temporally constant at the mean value of the tropical $\dot{H}$. Applying (2) to time mean $[CH_4]$ and to the functional form of $\dot{H}$ given above yields a set of three equations in three unknowns:

$$\alpha\,([CH_4] - [CH_4]_{ML}) + \tilde{w}\,[CH_4]_z - K\,[CH_4]_{zz} = -\gamma[CH_4] \qquad (4a)$$

$$\alpha + \tilde{w}\,(\ln f)_z + K\,(m^2 - f_{zz}/f) = 0 \qquad (4b)$$

$$\tilde{w}\,m + K\,(-2m(\ln f)_z - m_z) = \omega \qquad (4c)$$

where $m \equiv \phi_z$. At each vertical grid point we solve (4a)–(4c) simultaneously for α, $\tilde{w}$, and K. This method is well-conditioned if the determinant is non singular, but well-conditionedness is no guarantee that the three quantities will be positive everywhere or have smooth profiles.

The input data needed are time mean profiles of $[CH_4]$ in the tropics and in middle latitudes, and profiles of γ, f, and m. The $[CH_4]$ profiles are taken from the climatology of *Randel et al.* [1998] using equiva-

lent latitude limits of 30°–54° in both hemispheres for $[CH_4]_{ML}$; these limits were chosen to match the "surf zone" (see their Figure 7), where midlatitude values of trace constituents have only weak meridional gradients. The chemical reaction rates γ are taken from the $2\,^1/_2$-dimensional model of *Kinnersley* [1995]. The previous subsection described how we arrived at the smooth profiles f.

We have not yet defined ϕ, the vertical phase function from which m will be defined. It is possible, in principle, to derive ϕ directly from the HALOE data in Plate 1 and then differentiate to give m. We chose instead to derive m from the velocity w_{tr} already plotted in Figure 1; as is indicated in equation (B2), features of χ such as zero crossings rise at a rate equal to w_{tr}. In this context, attenuation does not affect the phase ϕ, so it is appropriate to consider the expression $\chi(z,t) = \cos(\phi(z) - \omega t)$, where ω is the annual frequency and ϕ is the phase. Differentiating χ first with respect to z and then with respect to t and applying (B2) yields the relation

$$m w_{tr} = \omega \tag{5}$$

so that m is defined in terms of w_{tr}. The profile of m (not shown) has the shape one would expect for the reciprocal of w_{tr}, with a maximum at about 20 km.

3.4. Some Approximate Answers

In the discussion that follows, it will be useful to have rough estimates of the quantities to be calculated, as well as plausible ranges of values. It is possible to determine α directly from $[CH_4]$ data by taking the time mean of (2) and neglecting the diffusion term:

$$\alpha = \alpha_m \equiv \frac{\bar{w}\chi_z + \gamma\chi}{\chi_{ML} - \chi} \tag{6}$$

with χ=$[CH_4]$. The profile of α_m is the solid curve in Figure 4a.

Some idea of extreme values of α and K can be estimated using the WKBJ approach set out in Appendix A. More accurate calculations based on (4a)–(4c) will check these estimates. The zeroth-order WKBJ equation is similar to (A5), but with $\bar{w}$ instead of w_{tr}, while the first-order equation (A6) is

$$-\bar{w}(\ln f)_z = Km^2 + \alpha \tag{7}$$

which illustrates the simple relationship between the two observables, $\bar{w}$ and f, and the two agents of attenuation, K and α.

From this equation alone, K and α cannot be uniquely determined, but we can estimate limiting values. We assume that $\bar{w} \approx w_{tr}$ and alternately set $K = 0$ and $\alpha = 0$ to derive, respectively, the largest α (α_{max}) and the largest K (K_{max}) that are consistent with the observed attenuation of the smooth tape recorder amplitude f under the WKBJ assumption. Also, with $\alpha = \alpha_m$ in (A6), a profile of K (K_m) can be derived that is consistent with α_m. That is,

$$-\bar{w}(\ln f)_z = K_{max}m^2 = \alpha_{max} = K_m m^2 + \alpha_m \tag{8}$$

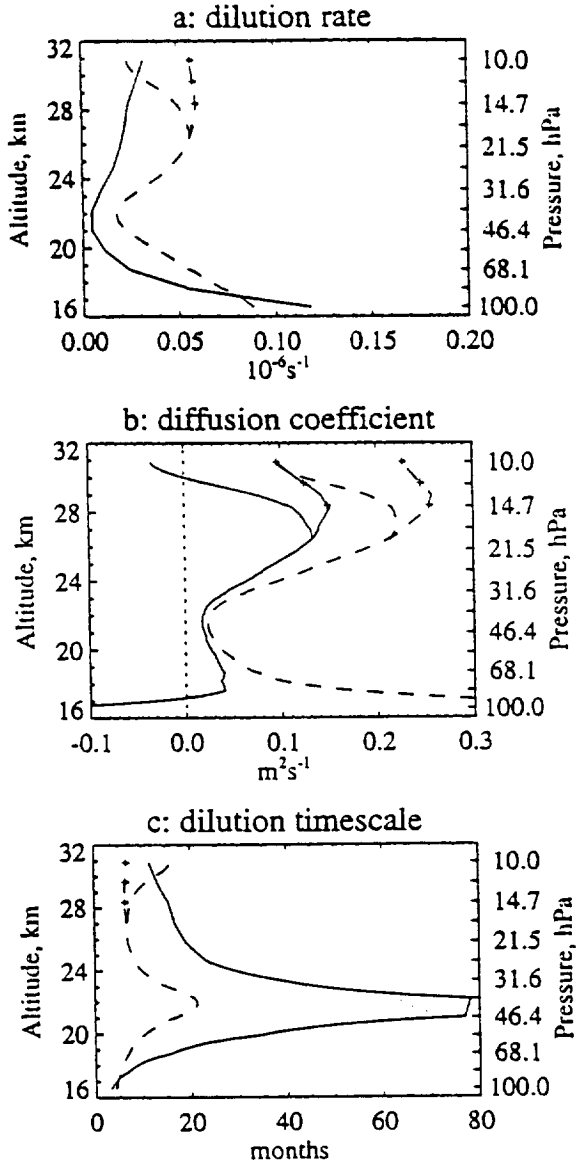

Figure 4. (a) Profiles of α_m (solid) and α_{max} (dashed) for curves M and M^* (the latter marked by plus symbols), (b) As in Figure 4a but for K_m and K_{max}, (c) As in Figure 4a but for $\tau_m = 1/\alpha_m$ (solid) and $\tau_{min} = 1/\alpha_{max}$ (dashed).

Figure 4 shows profiles of α_{max}, α_m, K_{max}, and K_m. (For $\ln f$ we have used the curves M and M^* in Figure 3, and solutions using $f = M^*$ are indicated by plus symbols.) The profiles in Figure 4a of α_m (solid curve) and α_{max} (dashed curves) both have a minimum of about 0.01–0.02 × $10^{-6}s^{-1}$ at 22 km, with values increasing toward the tropopause. K_{max} (Figure 4b, dashed curves) has a minimum of about 0.02 m^2s^{-1} also at 22 km and reaches much larger values near the tropopause. Where α_m exceeds α_{max}, K_m (solid curves) is negative; this occurs below 17 km and above 29 km (for M).

Solving (8) for the seven profiles of f shown in Figure 3, we find (results not shown) that α_{max} above 18 km always lies between 0.01 and 0.07 × $10^{-6}s^{-1}$ and

is sometimes smaller than α_m (implying that $K_m < 0$) above 27 km. Both α_{max} and K_{max} have a minimum near 22 km, since (from (A6)) they vary as the product of the fractional attenuation rate and a power (1 for α_{max}, 3 for K_{max}) of $\tilde{w}$. Curves fitted to curve *d* in Figure 2 tended to have smaller values of α_{max} and K_{max} above 24 km than did those fitted to curve *a*. The profiles of α_m and K_m for M^* were the most plausible, with α_m remaining fairly constant and K_m positive everywhere above 18 km. This is a consequence of fixing the attenuation rate to a constant above the cliff.

Most other researchers investigating the dilution of tropical air by midlatitude air [e.g., *Volk et al.*, 1996] have discussed, instead of the dilution rate α, the dilution timescale $\tau = 1/\alpha$. This quantity is shown in Figure 4c for the three profiles of α in Figure 4a. The minimum timescale (dashed curves, corresponding to maximum α) is about 5–15 months above 24 km and has a sharp peak of nearly 2 years at 22 km.

We emphasize that the curves shown in Figure 4 are not our best estimates of these quantities. The dashed curves represent extreme cases, under the WKBJ assumption, where only one of the two processes (dilution and diffusion) operates. In reality, $0 < K < K_{max}$ and $0 < \alpha < \alpha_{max}$. At each altitude there is (in the full solution) a unique combination of K and α consistent with the observed attenuation. Before solving (4a)–(4c) (the full, non-WKBJ set) to determine that unique combination, we first test the method using synthetic data.

3.5. Generation of Synthetic Data

We generate synthetic $[CH_4]$ and $\hat{H}$ data using various profiles of w, K, and α to solve (2). We can then inverse solve the synthetic data to derive profiles of w, K, and α, and compare these with the input profiles. This provides a complete, end-to-end check on the forward and inverse methods and codes, as well as a check that the inverse method, to be used on smoothed real data, is well conditioned and robust.

The simple model used to generate the synthetic data, then, is a discretized form of (2) and is run five times, using the five combinations of K and α given in Table 2. The profile of w used in each case is simply w_{tr} from Figure 1, but because equation (2) uses $\tilde{w}$ instead of w, and $\tilde{w}$ depends on K (see equation (3)), $\tilde{w}$ is slightly

Table 2. Profiles of K and α Used to Generate Synthetic Data

	Combination				
	1	2	3	4	5
K	0	0	K_m*	K_{max}	K_{max}
α	α_m	α_{max}	α_m	0	α_m

See text for definitions, and Figure 5 for profiles, of K_{max}, K_m, α_m, and α_{max}.

*The profile of K_m shown in Figure 4b was modified below about 17.5 km to increase monotonically to a value of 0.1 $m^2 s^{-1}$ at 100 hPa.

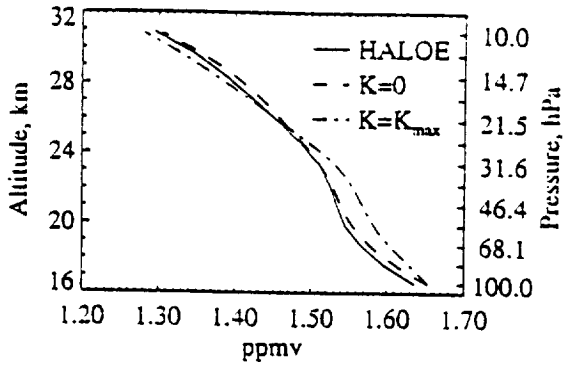

Figure 5. Time mean $[CH_4]$ in the tropics as observed by HALOE (solid curve) and as simulated by 1-D model for two values of the diffusion coefficient K: $K = 0$ (dashed curve) and $K = K_{max}$ (dash-dot curve).

different in each case. Advection is accomplished using essentially a semi-Lagrangian method, with the other terms time-split and semi-implicit; vertical resolution is quite fine (50 m), as is temporal resolution (0.5 day). To prevent error growth, the second derivative is evaluated on a reduced grid whose vertical resolution approximates that of the original HALOE data; then the result is interpolated to the 50 m grid. The chemical loss rate γ for $[CH_4]$ is again taken from the model of *Kinnersley* [1995].

The time mean $[CH_4]$ profile is calculated by integrating the model to steady state. The lower boundary value and midlatitude profiles are time mean values from *Randel et al.* [1998]. For $\hat{H}$ the lower boundary varies sinusoidally with a minimum in mid-February and an amplitude of 1. Both S (chemical source-sink) and χ_{ML} are zero. The model is integrated for 4 years, and only the last year of data is used in the subsequent calculation.

Figure 5 shows profiles of both time mean observed and steady state synthetic $[CH_4]$. The synthetic profiles were both obtained using $\alpha = \alpha_m$, one with $K = 0$ and one with $K = K_{max}$ (see Figure 4b). Over most of the domain, the synthetic profile with $K = 0$ falls within 0.01 ppmv of the observed profile. For $K = K_{max}$, however, differences are larger owing to the advective effect of $-K_z$ (equation (3)), which for K_{max} is large below 21 km.

We also calculated time-varying $\hat{H}$ for the five combinations of K and α shown in Table 2. With each of the combinations of K and α, the resulting $\hat{H}$ (Plate 2) qualitatively resembles Plate 1b. What distinguishes them is the rate of attenuation, which we will examine shortly, and the apparent ascent rate. In our 1-D model we can unambiguously identify the model's advective velocity ($\tilde{w}$, which includes diffusive effects) with the phase speed; in the real atmosphere the two quantities are not generally equal, though the tropical stratosphere is the only region where they are close [*Hall and Waugh*, 1997a]. The transit time from 100 hPa to 10 hPa of a (temporal) maximum or minimum decreases with increasing K, from 18.1 months for $K = 0$ to 17.1 months for $K = K_m$ to 16.0 months for $K = K_{max}$.

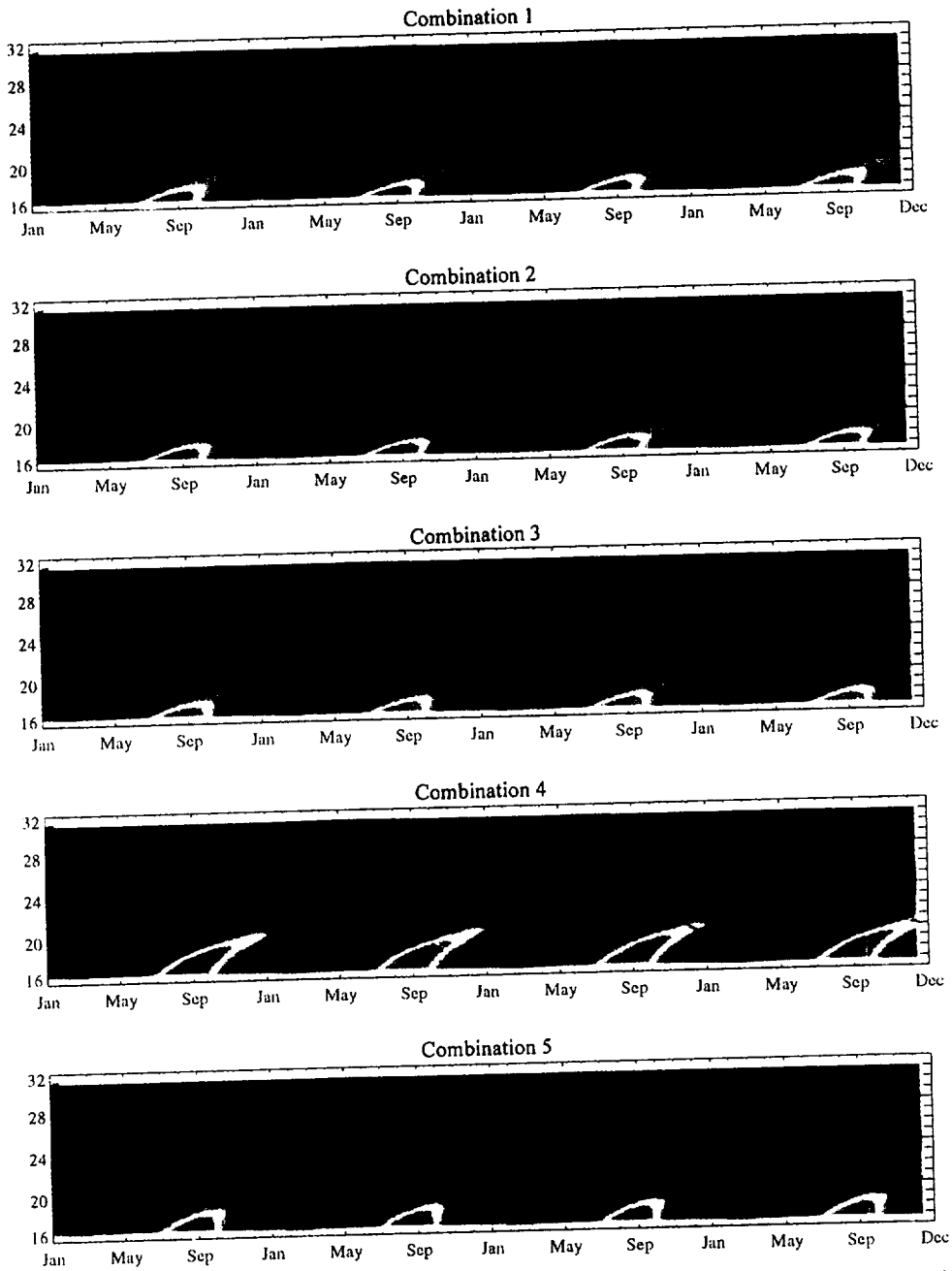

Plate 2. $\hat{\mathrm{H}}$ anomalies simulated by 1-D model for the five combinations of K and α given in Table 2.

The transit time estimated from HALOE data is 18.6 months. Note that in our 1-D model we have used $\tilde{w} = w_{\mathrm{tr}} + (K/H) - K_z$, so the faster ascent for nonzero K is to be expected. The transit time also depends weakly on α, differing by 14 days between combinations 4 ($\alpha = 0$) and 5 ($\alpha = \alpha_{\mathrm{m}}$) but only by 1.5 days between combinations 1 ($\alpha = \alpha_{\mathrm{m}}$) and 2 ($\alpha = \alpha_{\mathrm{max}}$).

The input profiles of K and α determine not just the ascent rate but also the amplitude of $\hat{\mathrm{H}}$ anomalies (Figure 6). Combination 2 reproduces the observed profile M^* fairly well. Combinations 2 and 4 represent (from (A6)) the extreme cases of no diffusion and no dilution, respectively, and since from (8) combinations 2, 3, and 4 all have the same profile of $Km^2 + \alpha$, they would produce the same attenuation were it not for the fact that $\tilde{w}$ is different for each one. For those combinations with $K \neq 0$ (3, 4, and 5) the ascent rate is quite fast in the lowest few kilometers of the stratosphere owing to the influence of diffusion; consequently, the tropical air has less time to be modified by diffusion and dilution, so there is less attenuation of the tape recorder signal at a given altitude.

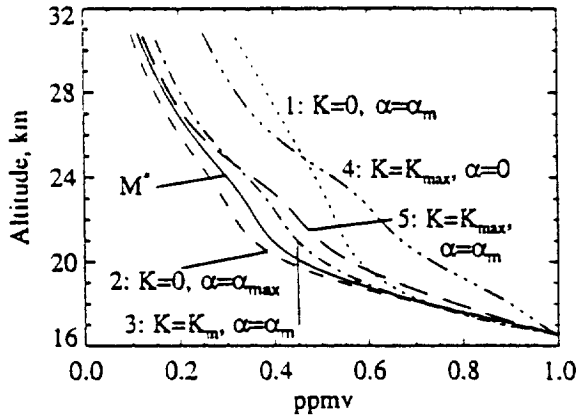

Figure 6. Amplitude of $\hat{H}$ anomalies simulated by 1-D model (broken curves). The solid curve is M^* from Figure 3, representing observations.

4. Results

4.1. Deducing Known Profiles of w, K, and α From Synthetic Data

In order to test our method of inverse-solving for K and α on the synthetic data, we must first determine m. This is done by calculating an ascent rate w_{synth} for each of the synthetic $\hat{H}$ time series, in a manner similar to that used to derive w_{tr}. Using the profile of w_{synth} for each combination, we calculate a corresponding profile of m for inverse solving equations (4a)–(4c).

For each of the five combinations of K and α in Table 2, we sample the synthetic data at vertical resolutions ranging from 1.2 km (similar to HALOE data) to the 50 m grid of the synthetic data, interpolate back to the 50 m grid, then inverse-solve (4a)–(4c) at 50 m resolution. As is shown in Figure 7 for combination 3 sampled at 1.2 km resolution, and for the other combinations and sampling resolutions (not shown), our method is fairly successful at recovering the input profiles of w ($= \tilde{w} - (K/H) + K_z$, from equation (3)), α, and K, at least between 18 and 28 km. Below 18 km the solution often differs substantially from the input values, a problem that is exacerbated at higher resolution. The problems below 18 km occur because the determinant of the matrix arising from (4a)–(4c) is small. In the high-resolution calculation, RMS errors (over the five combinations) between 18 and 28 km are small: 0.01–0.03 mm s^{-1} for w, $1-7\times10^{-9}$ s^{-1} for α, and 0.003–0.03 m^{2}s^{-1} for K. This method is clearly well suited for our purposes.

4.2. Deducing K and α From HALOE Data

With some confidence that our method will give good results above 18 km, we apply it to each of the seven smooth amplitude curves shown in Figure 3. We use the observed [CH_4] profile in Figure 5 and other input data as described in section 3.3. As with synthetic data, the HALOE data are interpolated to a 50 m vertical grid for calculations, then subsampled on a 1.2-km vertical grid for plotting. The results are shown in Figure 8. In each panel the mean is shown as the solid curve, bounded by $\pm1\sigma$, where σ is calculated over the six smooth curves (not including M^*). The derived profile of w is very similar to w_{tr} (long-dashed curve) but is somewhat lower above 24 km.

All seven definitions of f yield results for α that are substantially similar to each other and to α_m (Figure 8b), for reasons that will be discussed shortly.

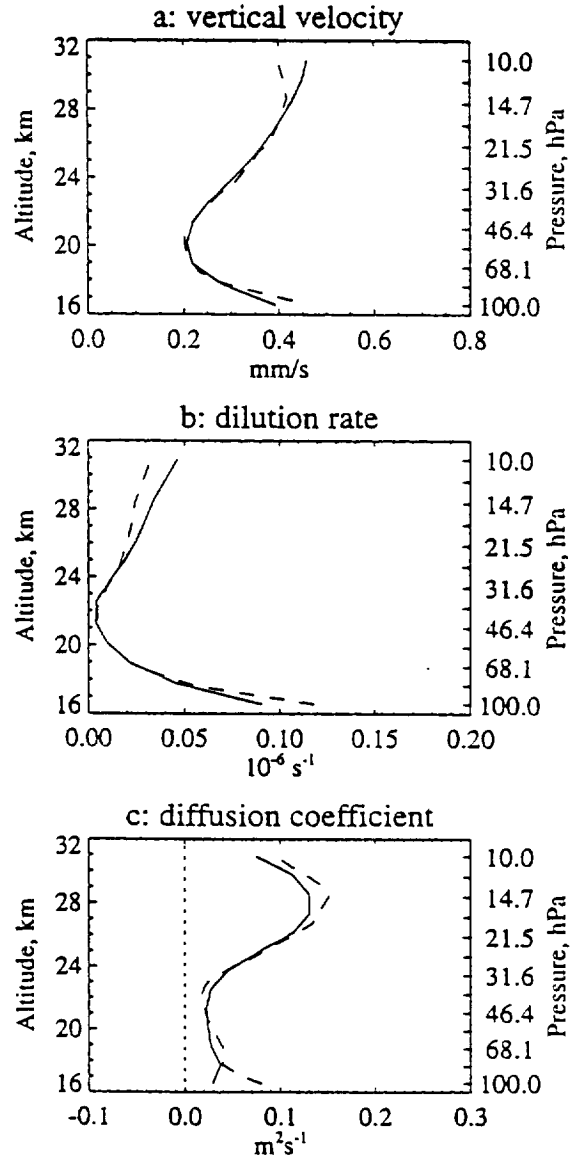

Figure 7. End-to-end consistency check by forward solving and then inverse solving equation (1). Dashed curves are the profiles used for forward solution and are, respectively, the same as (for w in Figure 7a) the plain solid curve in Figure 1, (for α in Figure 7b) the solid curve in Figure 4a, and (for K in Figure 7c) the solid curve with plus symbols in Figure 4b, modified as noted in Table 2. Solid curves in this figure are profiles derived from inverse solving. Differences give an idea of the effects of numerical truncation error.

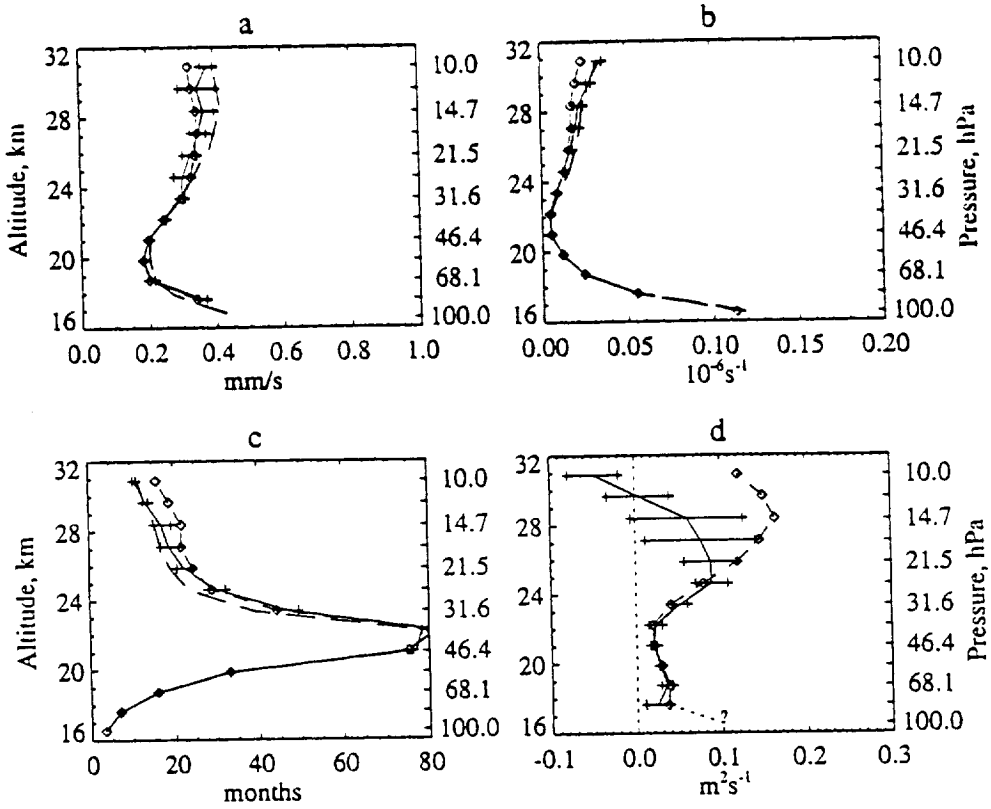

Figure 8. Profiles of (a) w, (b) α, (c) $\tau = 1/\alpha$, and (d) K calculated by inverse solving the 1-D model with HALOE data, using equations (4). In each panel the mean of six solutions using the six broken curves in Figure 3 is shown as the solid curve, bounded by $\pm 1\sigma$. Also plotted are the results when $f = M^*$ (diamonds). The calculation is performed on a 50-m grid, but the results are plotted on HALOE levels. Long-dashed curves in Figures 8a, 8b, and 8c represent w_{tr}, α_m, and $1/\alpha_m$, respectively. The solution for K (with $f = M^*$) has been extended to 100 hPa as is discussed in section 5.2.

The minimum values are less than $1.0 \times 10^{-8}s^{-1}$, and $\alpha < 4.0 \times 10^{-8}s^{-1}$ everywhere above 18 km. The reciprocal of α, τ (Figure 8c), indicates far longer timescales than in previous research, for reasons that we discuss in section 5.4. At this point it is sufficient to note that the range of values above 18 km is 1.5–7 years, much longer than the advective timescale.

Profiles of K are reasonably consistent for all seven curves between 18 and 25 km, but differ markedly from each other above and below this altitude range. For most definitions of f, K decreases again above 24 km and for many, K becomes negative at some altitude. The profiles with $f = M^*$ and with curve a smoothed 1000 times are the only ones for which $K > 0$ everywhere above 18 km. Below 18 km, most profiles are negative. The tentative extension of the solution to 100 hPa will be explained in section 5.2.

It is worth noting that a conceptually simpler approach, the WKBJ method outlined in Appendix A, yields very similar results. In essence, the WKBJ method says that $w = w_{tr}$, $\alpha = \alpha_m$ (from equation (6)), and $K = K_m$. That is, $[CH_4]$ tells us about dilution, and the role of diffusion can be deduced from the excess attenuation of the $\tilde{H}$ anomalies above that expected from dilution alone.

5. Discussion and Conclusions

The ability of the first pair of EEOFs to reproduce the essential features of the tape recorder signal (Plate 1) underscores the simplicity of the phenomenon; marks left in the air by annual variations of tropopause temperature are the dominant variation in tropical water vapor below 10 hPa. The somewhat ragged HALOE data are smoothed nicely by EEOFs, allowing us to estimate directly the ascent rate of the tape recorder signal, w_{tr}. Knowing K allowed us to extract a profile of w (Figure 8a) from $\tilde{w}$.

Having simultaneously derived profiles of the three quantities w, α, and K, we now consider in more detail the assumptions and weaknesses in the calculation. We also discuss the implications of our findings and compare them to those of other researchers.

5.1. Comments on the Method of Deriving K and α

Several aspects of the calculation bear consideration: the reliability of the data, our definition of tape recorder amplitude, the curve-fitting techniques used, the appropriateness of equation (1), and our numerical approach to finding K and α (equations (4a)-(4c)).

The papers validating HALOE H_2O [*Harries et al.*, 1996] and CH_4 [*Park et al.*, 1996] provide estimates of the systematic and random errors of these two quantities (their Tables 1). The errors grow with pressure in the lower stratosphere; for example, the root-sum-square of all sources of error for CH_4 is 11% at 10 hPa and 19% at 100 hPa. While the larger errors at 100 hPa may affect our results, we believe this effect is minimal for several reasons. First, the error tables refer to individual profiles, but we have used monthly means; for large numbers of profiles (usually 50 or more) the random errors average to zero, leaving systematic errors at 100 hPa of 15% for CH_4 and 24% for H_2O. Second, $\hat{H}$ data enter the solution mainly through $(\ln f)_z$. The only systematic errors that could have a significant effect on $(\ln f)_z$ are those with a seasonal, altitude-dependent bias; a uniform positive or negative bias at any level would have no effect on f at that level, nor would a seasonal bias that was independent of altitude. While it is possible that a seasonal, altitude-dependent bias exists, it would probably not be the largest component of the systematic errors. A known bias exists in the lower stratosphere between profiles taken during sunrise and those taken during sunset, but over the 5 years there is no seasonal bias between sunrise and sunset profiles. Finally, one can estimate the seasonal variations in $\hat{H}$ at 100 hPa using observed 100 hPa temperatures to calculate saturation mixing ratios [M96]; these place an upper bound of about 3 ppmv on the amplitude, compared to 1.1–1.5 ppmv using the various definitions employed here. If we have underestimated the amplitude, that would merely serve to increase α and K below 18 km, where they are already large and perhaps unreliable.

A potential weakness of our calculation is the actual definition of the amplitude of the tape recorder signal. As is discussed in section 3.2, this definition should distinguish variations whose source is the tropical tropopause from all other variations. Furthermore, since α and K must be positive, and since w_{tr} is observed to be positive, by (A6) the smoothed amplitude profile f must be monotonically decreasing with altitude. In our opinion, the definition using EEOFs (curve *a* in Figure 2) is the best one because the variations seen in Plate 1b are clearly linked to the tropopause. By some other definitions the amplitude decreases less quickly with altitude above 24 km, but these other definitions are more susceptible to variations attributable to other causes as discussed in section 3.2. Only two curves, one of them M^*, lead to positive K above 28 km, and it seems reasonable to conclude that the other curves are not decreasing fast enough above 28 km.

The next point of concern is the curve fitting. For a model like (1) to succeed, smoothing must be performed on the profiles of w_{tr} and especially the amplitude A. We have attempted to bracket the range of plausible curves by using two definitions of amplitude and three degrees of smoothing.

One might well ask whether the 1-D model represented in equation (1) accurately depicts the dynamics of the tropical stratosphere. Perhaps the greatest weakness in the model is the treatment of dilution as a linear relaxation process, especially below 20 km, where the tropics and middle latitudes are influenced by the swirl of monsoonal and other three-dimensional circulations protruding from the troposphere [*Dunkerton*, 1995]. Vertical diffusion too has more complex characteristics below 20 km. For these reasons and because of the poorer performance of the inverse solving method below 18 km even with "perfect" data (Figure 7), we have little confidence in our results below 18 km, especially for K.

Finally, we discuss our approach to inverse solving (2). Our method tests well on synthetic data except below about 18 km. It gives a definite result at every altitude, but with HALOE data at upper and lower levels it tends to give small or negative K except for the best profile M^*. Note that by assuming that temporally constant profiles of w_{tr}, α, and K apply to both $[CH_4]$ and $\hat{H}$, we ignore covariance terms like $w'\chi'_z$, leaving just $[w][\chi_z]$ (where $[w]$ represents a time mean and w' is a departure from that mean) and similar terms. Seasonal variations in w_{tr} [see *Rosenlof*, 1995], α [see *Bowman and Hu*, 1997], and K appearing in covariance terms would be interesting, but their calculation is beyond the scope of this work.

5.2. Vertical Velocity

A preliminary version of our Figure 1 was presented by *Dunkerton* [1997], who compared a profile of w_{tr} derived from the (shorter, version 17) data used by M96 with the radiatively derived transformed Eulerian mean vertical velocity $\bar{w}^*$ of *Rosenlof* [1995] (which constrains the global vertical mass flux to zero); both showed a minimum ascent rate of about 0.2 mm s^{-1} at about 21 km. *Eluszkiewicz et al.* [1997] have also calculated $\bar{w}^*$, and a profile formed by averaging five of their profiles calculated using different inputs (not shown) generally falls within the error bars of the two curves in Figure 1 but has less vertical variation.

We now discuss the significance of similarities and differences among the quantities w, $\bar{w}^*$, w_{tr}, and $\tilde{w}$ (Table 1). In principle, $\bar{w}^*$ should be the same as the vertical advection velocity w. We consider two questions: (1) whether w_{tr} calculated mathematically with (B3) using the results of our inverse-solving method ($\tilde{w}$ and K) agrees with w_{tr} found using Plate 1b and (2) the implications of the differences between w_{tr} and $\bar{w}^*$ above 24 km and below 18 km.

To address the first question, we calculate the terms in the definitions of $\tilde{w}$ (equation (3)) and w_{tr} (equation B4) and plot the results in Figure 9. For K we have used the profile indicated by diamonds in Figure 8d, extended to 0.1 $m^2 s^{-1}$ at 100 hPa as indicated, for reasons that will shortly become clear. The vertical advection velocity w is shown as the solid curve; of all the curves, it has the smallest variation, being generally near 0.3 mm s^{-1}, but like the others it has a pronounced minimum at 20 km. Figure 9 implies that the true advection velocity is slower than the ascent rate of

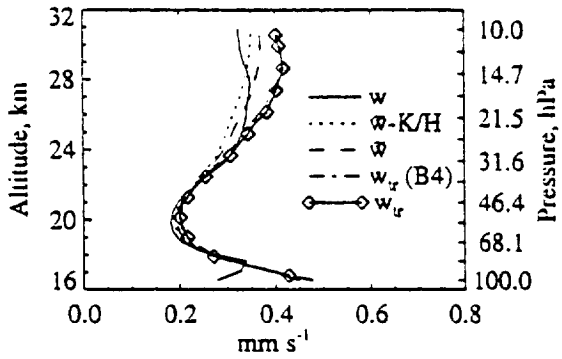

Figure 9. Plots of $w = \bar{w} - (K/H) + K_z$, $\bar{w}$, $\bar{w} - (K/H)$, w_{tr} as predicted by approximate formula (B4), and w_{tr} as originally estimated from Plate 1b. Solutions correspond to $f = M^*$, the case shown by diamonds in Figure 8. See text for details.

marks on the tape (w_{tr}) and that this difference is due to diffusion. The K/H term (dotted curve) amounts to no more than 10% of $\bar{w}$. The profile of w_{tr} derived mathematically from (B4) (dash-dot curve) is virtually identical to w_{tr} itself (diamonds), which is an encouraging demonstration of the consistency of $\bar{w}$, K, and the derivatives used in calculating the approximation $1/h$ in (B5).

To address the second question, we consider first the differences above 24 km, where $\bar{w}^*$ is significantly larger than w_{tr}, which in turn is larger than w. Assuming for the moment that our estimate of K is inaccurate and also that $\bar{w}^* = w$, (B4) could explain the difference only if K were large and negative, or K_z were large and positive, because the K terms compete with the $-K_z$ term. Because of this competition, only absurdly large values of K could explain the difference between $\bar{w}^*$ and w_{tr}. It therefore seems that $\bar{w}^* \neq w$; either our estimate of w_{tr} is too small, or Rosenlof's $\bar{w}^*$ is too large. We note that Eluskiewicz's estimates of $\bar{w}^*$ are also smaller than Rosenlof's, generally 0.3–0.4 mm s^{-1}, and that a significantly larger w, and hence w_{tr}, would mean that (for plausible values of K) $\hat{H}$ anomalies would arrive at 10 hPa much faster than is observed.

Below 18 km our results generally suggest an increase of $\bar{w}$, α, and K approaching the tropopause, but the uncertainty of K is relatively large, and more than one interpretation is possible. On the one hand, if $\bar{w}^*$ is qualitatively correct in this region, then a rapidly decreasing K might be responsible for the difference of about 0.2 mm s^{-1} between $\bar{w}^*$ and w_{tr}. Such a profile of K would be expected if vertical mixing were enhanced in a shallow layer owing to overshooting deep convection, as well as the local breaking of slow Kelvin and gravity waves launched by convective systems. Assuming a linear profile of K between 100 hPa and 83 hPa (as indicated by the dotted line in Figure 8d), it turns out that $K = 0.1$m^{2}s^{-1} at 100 hPa will produce the difference of 0.2 mm s^{-1} between w and w_{tr}.

On the other hand, if $w_{tr} \simeq w$, i.e., increasing rapidly approaching the tropopause (as in *Dunkerton*'s [1997] model of the QBO, for example) then K at 100 hPa must be much smaller and something must be missing from Rosenlof's radiative model, such that the actual diabatic heating rates are significantly larger at, and just above, the tropopause. One possibility is that heating associated with subvisible cirrus [*Wang et al.*, 1996], not included in Rosenlof's calculation, contributes to enhanced ascent in this layer.

Another explanation of the observed tape signal near the tropopause is that the "recording head," in reality, has a finite depth due to spatial and temporal variations of tropopause altitude, so that the source of the $\hat{H}$ signal is somewhat fuzzy, giving the appearance of enhanced apparent ascent. To be sure, the observed vertical displacements of tropopause altitude occupy a significant fraction of the layer in which enhanced ascent is observed, and might therefore account, to some extent, for the observed signal. Nevertheless, none of the physical mechanisms described in the previous paragraph can be readily dismissed, and they merit further study. For example, knowledge of the population of overshooting convection, along the lines discussed by *Zhang* [1993], could (in principle) be used to model $K(z)$ for comparison to derived estimates. Similar models of diffusivity might be obtained from examination of breaking waves in long records of aircraft and rawinsonde data. A more thorough examination of these mechanisms will improve our understanding of stratosphere-troposphere exchange, dehydration, and radiative balance.

5.3. Diffusion

The derived profile of K has a minimum of about 0.02 m^{2}s^{-1} near 21 km; between 18 and 24 km, the values of K are similar for all definitions of f. Below 18 km the values of K are unreliable but probably increase downward. Above 24 km our results suggest a value of K around 0.1 m^{2}s^{-1}. These values are somewhat greater than the value of 0.01 m^{2}s^{-1} *Hall and Waugh* [1997b] derived for the layer between the 100- and 31.6-hPa HALOE levels, but they used *Randel et al.*'s [1998] definition of amplitude (plus symbols in Figure 2), which has smaller vertical derivative. Our values of K are somewhat less than the 0.07 m^{2}s^{-1} derived by *Remsberg* [1980] for 19°N, and are considerably less than the 1–7 m^{2}s^{-1} derived by *Patra and Lal* [1997] for 18°N, but the latter authors neglected vertical advection. The profiles of K that they showed, from their work and from several papers in the 1970s and 1980s, were otherwise qualitatively similar to ours, with a minimum around 19–21 km, sharp increases toward the tropopause, and slow increases up to 50 km.

Above 24 km the uncertainty in our derived K is large and depends sensitively on the definition of the amplitude curve f. For most curves f in Figure 3, K becomes negative at some altitude. Only for $f = M^*$ and a highly-smoothed curve a does K remain positive.

The diffusion coefficient included in (1) represents the effects of a number of processes. These include small-scale processes such as turbulence due to gravity-wave breaking, but also larger-scale processes such as the di-

abatic dispersion discussed by *Sparling et al.* [1997]. In the tropical context the latter is likely to arise from the fact that as air parcels move longitudinally they experience different histories of radiative heating, due to the temporal and spatial variation of the heating field. Such variations may occur on the largest scales, e.g., in association with the warm pool region, or on mesoscales, e.g., in association with radiative effects of cirrus decks associated with individual convective systems.

5.4. Dilution

Unlike K, α is not very sensitive to the definition of f. All curves have a minimum of about 5×10^{-9} s^{-1}, somewhat smaller than for α_m (Figure 4b). Above 24 km, α is close to 2×10^{-8} and values are much larger below 18 km. The small values of α between 18 and 24 km approach the zero-dilution limit of *Plumb*'s [1996] "tropical pipe" model.

The reciprocal of α (τ) is the timescale for dilution by midlatitude air, and has a maximum at about 22 km (Figures 4c and 8c). Our maximum value of τ (80 months) is, however, extremely large compared to the values reported by M96 (15–18 months between 46 and 22 hPa), *Minschwaner et al.* [1996] (maximum 12–16 months), *Volk et al.* [1996] (13.5 months between 16 and 21 km), *Schoeberl et al.* [1997] (18 months between 20 and 28 km), *Hall and Waugh* [1997b] (16 months betwen 100 and 32 hPa), and *Randel et al.* [1998] (15 months between 68 and 32 hPa). While some previous studies [*Hitchman et al.*, 1994; *Minschwaner et al.*, 1996; M96; *Remsberg and Bhatt*, 1996] have suggested that there is an altitude range where air is more isolated from middle latitudes, our results indicate a much greater degree of isolation than other studies.

To understand why this is so, we mention a few relevant observations. First, the profiles of α and τ give different impressions; α contrasts the rapidity of dilution below about 18 km with the slowness above 18 km, while τ emphasizes the very long timescale over the 20–24 km altitude range. Coarser resolution of τ would diminish the maximum; in fact, over the 20–28 km altitude range of *Schoeberl et al.* [1997], the reciprocal of our average α is 33 months. Second, since most other estimates of the dilution rate have neglected the role of diffusion, their estimates of τ should be viewed as lower limits, and indeed, when we neglect diffusion (Figure 4c), our profile of τ resembles that of other studies. Third, other studies have generally assumed a vertical velocity profile that is constant with altitude, but when the vertical velocity profile has a minimum (as does w_{tr}), the timescale for dilution necessarily increases at the altitude of the velocity minimum.

Fourth, other studies have not shown the cliff, that is, the sharp reduction in the vertical gradient of $[CH_4]$ and $\hat{H}$ from HALOE and of $[H_2O]$ from MLS between about 20 and 23 km (Figures 2 and 5). We raised the possibility earlier that the cliff is spurious. However, it appears consistently not just in the quantities mentioned but also in HALOE HF [e.g., *Cordero et al.*, 1997] and CLAES CH_4 and N_2O [*Roche et al.*, 1996]. The cliff occurs just at the flight ceiling of the ER-2 research aircraft (about 21 km).

This cliff, together with the minimum in vertical velocity, gives rise to much smaller values of α, hence larger values of τ. The actual values of τ are so much longer than the timescale for vertical advection as to be practically infinite (i.e., the transport barrier between tropics and middle latitudes is almost perfect) at these levels.

5.5. Final remarks

Using the WKBJ approach (equation (A6)) and considering only the attenuation rate of the tape recorder signal in $\hat{H}$, we derived profiles of the maximum dilution rate α_{max} and of the maximum vertical diffusion K_{max} for the extreme scenarios where (respectively) $K = 0$ and $\alpha = 0$. We can use α_{max} and K_{max}, along with our derived profiles of K and α, to estimate the fractional attenuation due to dilution, α/α_{max}, and the fractional attenuation due to vertical diffusion, K/K_{max}. In Figure 10 we show these quantities for $f = M$ and $f = M^*$. For virtually all the curve fits, the results resemble those for $f = M$: dilution dominates below 18 km, diffusion dominates between 18 and 28 km, and dilution again dominates above 28 km. For our "best" curve fit $f = M^*$, however, diffusion dominates over nearly the entire stratosphere.

Our analysis therefore shows that despite the fairly small values of K (as low as 0.02 m^{2}s^{-1}) in the altitude range 18–28 km, vertical diffusion plays a significant role in attenuating the tape signal. From Figure 6, even modest values of K can make a significant difference in the net attenuation at 10 hPa (compare curves (1) and (3)). While these values of K will have little impact on the budget of a monotonically varying constituent like $[CH_4]$, it is clear that one cannot neglect diffusion when considering a constituent whose second derivative is large, like water vapor or perhaps (at some altitudes) ozone. Improvements to 1-D models like those of *Avallone and Prather* [1996] or *Patra and Lal* [1997] would include all of the processes represented in equation (1).

The results presented here suggest that the tropical air column can be divided into three regions. Below about 18 km, α and w_{tr} are comparatively large, and diffusion is probably large there as well. *Holton et al.* [1995] and *Rosenlof et al.* [1997] distinguished this region from the stratospheric "overworld," and it falls under the direct influence of tropospheric circulations, as was noted in section 5.2. When the air rises to the second region, about 19 km, it finds itself extremely isolated from middle latitudes up to about 23 km, and this isolated air rises very slowly (it takes 6 months to travel those 4 km). In this region, dilution is so weak that the amplitude of $\hat{H}$ anomalies is approximately constant with altitude (Figure 2), and $[CH_4]$ decreases at a markedly reduced rate (Figure 5); what loss of $[CH_4]$ occurs there can be attributed mostly to photochemistry. Also, although K too has a minimum there, it appears to be largely responsible for the weak attenuation that does occur (Figure 10). This extreme iso-

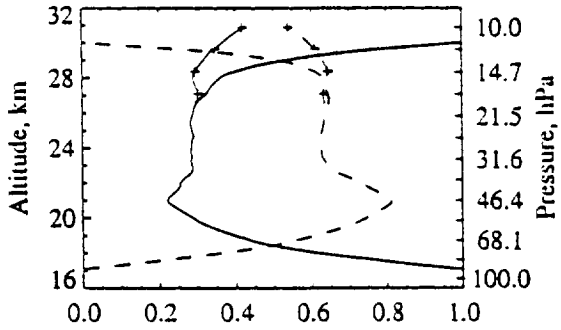

Figure 10. Fraction of attenuation of the observed $\dot{H}$ signal due to diffusion (dashed curve) and dilution (solid curve) for $f = M$ and $f = M^*$ ('+' symbols). Curves do not quite add to 1 because results are shown as the ratio of the full solution to the maximum allowed with the WKBJ approximation.

lation is consistent with the remarkably long duration of QBO westerlies below 23 km. When the air reaches the third region, above 23 km, α, K, and w_{tr} are again larger, and the air again feels the influence of middle latitudes. In contrast to the region below 18 km, where the swirl of tropospheric circulations is responsible for dilution, the agents of dilution above 23 km are probably Rossby waves propagating from middle latitudes [*O'Sullivan and Dunkerton*, 1997].

Appendix A: WKBJ Solution: Advection-Diffusion-Dilution Equation

For the purposes of section 3.4 and elsewhere, we consider approximate solutions to (2) applied to $\dot{H}$, so that $S = 0$. Regarding the tape signal as a slowly modulated sinusoid, so that WKBJ (Wentzel-Kramers-Brillouin-Jeffreys) theory will be applicable, we assume a solution of the form $\chi(z,t) = \mathrm{Re}A(Z)\exp[i(\phi(z) - \omega t)]$, where $Z = \mu z$ is a slow height variable, $A(Z)$ is a slowly varying amplitude, and ϕ is now defined by $\phi_z = m(Z)$, so that m, though not ϕ, is assumed slowly varying. As in section 3.3, we may take both A and ϕ to be real; note that apart from restricting it to be a function of Z alone, hence slowly varying, A is the same as the $f(z)$ of section 3.3. Defining $\hat{\phi} = \phi(z) - \omega t$, we have

$$\chi_z = \mathrm{Re}\left\{(\mu A' + imA)\exp i\hat{\phi}\right\} \tag{A1a}$$

$$\chi_{zz} = \mathrm{Re}\left\{(\mu^2 A'' + 2im\mu A' + im'\mu A - m^2 A)\exp i\hat{\phi}\right\} \tag{A1b}$$

where primes denote differentiation with respect to Z, so that (2) with $S = 0$ becomes

$$-i\omega A + \tilde{w}(\mu A' + imA) = K(\mu^2 A'' + 2im\mu A' + im'\mu A - m^2 A) - \alpha A \tag{A2}$$

Forward solution of this equation when $\tilde{w}$ and K are prescribed functions of Z alone proceeds with an expansion of A in powers of μ:

$$A = A_0 + \mu A_1 + \mu^2 A_2 + \cdots \tag{A3}$$

so that at zeroth order in μ,

$$-i\omega A_0 + im\tilde{w}A_0 = -(Km^2 + \alpha)A_0. \tag{A4}$$

For real m it will be assumed that Km^2/ω and α/ω are $O(\mu)$ whence

$$m\tilde{w} = \omega \tag{A5}$$

This is the approximate WKBJ counterpart, at this order, of the exact relation (5). In general, the three terms of $\tilde{w} = w + (K/H) - \mu K'$ contribute to the apparent upwelling, including terms involving K, but under the WKBJ approximation K is small, so to leading order, m is determined by w. At first order in μ, we then have

$$\tilde{w}A_0' = -(Km^2 + \alpha)A_0 \tag{A6}$$

for the slowly varying amplitude, with $\tilde{w} \approx w$.

According to (A5) and (A6), vertical advection has two effects on the oscillatory solution. At zeroth order, it creates a wavy vertical structure, translating information from the lower boundary upward along characteristics

$$\left(\frac{dz}{dt}\right)_\chi \approx \tilde{w}. \tag{A7}$$

At first order, advection maintains the amplitude envelope of χ against attenuation due to vertical diffusion of the wavy vertical structure and linear damping.

Appendix B: The Relationships Among w, $\tilde{w}$, and w_{tr}

Recall that w is defined as the vertical advection velocity, $\tilde{w} = w + (K/H) - K_z$ is the quantity found by inverse solving (4a)–(4c), and w_{tr} is the ascent rate of $\dot{H}$ anomalies, defined graphically from the EEOF-reconstructed plot, Plate 1b. We begin by noting that diffusion can change the apparent tape speed much more than dilution can, as is discussed in section 3.5; variations in K for fixed α had a much greater effect on the transit time from 100 to 10 hPa than did variations in α for fixed K.

Taking (2) with χ redefined as the $\dot{H}$ anomaly, i.e., the departure from the mean, in other words the tape signal alone:

$$\chi_t + \tilde{w}\chi_z = K\chi_{zz} - \alpha\chi - \gamma\chi \tag{B1}$$

Now, every extremum ($\chi_z = 0$) and zero crossing ($\chi = 0$) must ascend with velocity w_{tr}. The following result can be obtained using either fact, but it is simpler to use the zero crossings. We have

$$\chi_t + w_{tr}\chi_z = 0 \tag{B2}$$

at those altitudes and times for which $\chi = 0$. By com-

paring (B1) with (B2), we readily obtain, regardless of the values of α and γ,

$$w_{tr} = \bar{w} - \left.\frac{K\chi_{zz}}{\chi_z}\right|_{\chi=0} \quad \text{(B3)}$$

whence, using equation (3),

$$w_{tr} = w + K/H + K/h - K_z \quad \text{(B4)}$$

where $h = -\chi_z/\chi_{zz}$; note that no approximations have yet been made. We can calculate h by substituting into the above from (A1a) and (A1b), and keeping only the leading order terms in the WKBJ sense, yielding

$$1/h \simeq -2(\ln A)_z - (\ln m)_z \quad \text{(B5)}$$

Variations of h about its mean value of 3.6 km are small. Figure 9 compares w, $\bar{w}$, w_{tr}, and w_{tr} calculated using (B4) with the approximation for $1/h$. The similarity of the two w_{tr} curves provides a valuable end-to-end check of our method, since the derivation in (B4) relies on A and m and on $\bar{w}$ and K found by inverse solving (4a)–(4c).

Acknowledgments.

We thank the HALOE science team for the high-quality HALOE data set, Jonathan Kinnersley for the chemical reaction rates, Bill Randel for the constituent climatology, and Tim Hall and Don Delisi for fruitful conversations and helpful comments on the manuscript. This work was supported by National Aeronautics and Space Administration contracts NAS1-96071 and NAS5-32862.

References

Avallone, L.M., and M.J. Prather, Photochemical evolution of ozone in the lower tropical stratosphere, *J. Geophys. Res., 101*, 1457–1461, 1996.

Bowman, K.P., and Y. Hu, Tropical mixing barriers in the lower stratosphere in the Geophysical Fluid Dynamics Laboratory SKYHI model, *J. Geophys. Res., 102*, 21,465–21,478, 1997.

Chen, P., J.R. Holton, A. O'Neill, and R. Swinbank, Isentropic mass exchange between the tropics and extratropics in the stratosphere, *J. Atmos. Sci., 51*, 3006–3018, 1994.

Cordero, E.C., S.R. Kawa, and M.R. Schoeberl, An analysis of tropical transport: Influence of the quasi-biennial oscillation, *J. Geophys. Res., 102*, 16,453–16,461, 1997.

Dunkerton, T.J., Evidence of meridional motion in the summer lower stratosphere adjacent to monsoon regions, *J. Geophys. Res., 100*, 16,675-16,688, 1995.

Dunkerton, T.J., The role of gravity waves in the quasi-biennial oscillation, *J. Geophys. Res., 102*, 26,053–26,076, 1997.

Eluszkiewicz, J., D. Crisp, R. G. Grainger, A. Lambert, A. E. Roche, J. B. Kumer, and J. L. Mergenthaler, Sensitivity of the residual circulation diagnosed from the UARS data to the uncertainties in the input fields and to the inclusion of aerosols, *J. Atmos. Sci., 54*, 1739–1757, 1997.

Hall, T.M., and D.W. Waugh, Timescales for the stratospheric circulation derived from tracers, *J. Geophys. Res., 102*, 8991–9001, 1997a.

Hall, T.M., and D.W. Waugh, Tracer transport in the tropical stratosphere due to vertical diffusion and horizontal mixing, *Geophys. Res. Lett., 24*, 1383–1386, 1997b.

Harries, J.E., J.M. Russell III, A.F. Tuck, L.L. Gordley, P. Purcell, K. Stone, R.M. Bevilacqua, M. Gunson, G. Nedoluha, and W.A. Traub, Validation of measurements of water vapor from the Halogen Occultation Experiment, *J. Geophys. Res., 101*, 10,205–10,216, 1996.

Hitchman, M.H., M. McKay, and C.R. Trepte, A climatology of stratospheric aerosol, *J. Geophys. Res., 99*, 20,689–20,700, 1994.

Holton, J.R., P.H. Haynes, M.E. McIntyre, A.R. Douglass, R.B. Rood, and L. Pfister, Stratosphere-troposphere exchange, *Rev. Geophys., 33*, 405–439, 1995.

Kinnersley, J.S., A realistic three-component planetary wave model, with a wave-breaking parametrisation, *Q. J. R. Meteorol. Soc., 121*, 853–881, 1995.

Mastenbrook, H.J., and S.J. Oltmans, Stratospheric water vapor variability for Washington DC/Boulder, CO: 1964–1982, *J. Atmos. Sci., 40*, 2157–2165, 1983.

Minschwaner, K., A.E. Dessler, J.W. Elkins, C.M. Volk, D.W. Fahey, M. Loewenstein, J.R. Podolske, A.E. Roche, and K.R. Chan, The bulk properties of isentropic mixing into the tropics in the lower stratosphere, *J. Geophys. Res., 101*, 9433–9439, 1996.

Mote, P.W., K.H. Rosenlof, R.S. Harwood, J.R. Holton, and J.W. Waters, Seasonal variations of water vapor in the tropical lower stratosphere, *Geophys. Res. Lett., 22*, 1093–1096, 1995.

Mote, P.W., K.H. Rosenlof, M.E. McIntyre, E.S. Carr, J.C. Gille, J.R. Holton, J.S. Kinnersley, H.C. Pumphrey, J.M. Russell III, and J.W. Waters, An atmospheric tape recorder: The imprint of tropical tropopause temperatures on stratospheric water vapor, *J. Geophys. Res., 101*, 3989–4006, 1996.

O'Sullivan, D.J., and T.J. Dunkerton, The influence of the quasi-biennial oscillation on global constituent distributions, *J. Geophys. Res., 102*, 21,731–21,743, 1997.

Park, J.H., et al., Validation of Halogen Occultation Experiment CH_4 measurements from the UARS, *J. Geophys. Res., 101*, 10,183–10,204, 1996.

Patra, P.K., and S. Lal, Variability of eddy diffusivity in the stratosphere deduced from vertical distributions of N_2O and CFC12, *J. Atmos. Terr. Phys., 59*, 1149–1157, 1997.

Plumb, R.A., A "tropical pipe" model of stratospheric transport, *J. Geophys. Res., 101*, 3957–3972, 1996.

Randel, W.J., F. Wu, J.M. Russell III, A. Roche, and J.W. Waters, Seasonal cycles and QBO variations in stratospheric CH_4 and H_2O observed in UARS HALOE data, *J. Atmos. Sci., 55*, 163–185, 1998.

Remsberg, E.E., Diffusion in the lower stratosphere as determined from lidar measurements of volcanic aerosol dispersion, *J. Atmos. Sci., 37*, 2105–2112, 1980.

Remsberg, E.E., and P.P. Bhatt, Zonal variance of nitric acid vapor as an indicator of meridional mixing in the subtropical lower stratosphere *J. Geophys. Res., 101*, 29,523–29,530, 1996.

Roche, A.E., et al., Validation of CH_4 and N_2O measurements by the cryogenic limb array etalon spectrometer instrument on the Upper Atmosphere Research Satellite, *J. Geophys. Res., 101*, 9679–9710, 1996.

Rosenlof, K.H., Seasonal cycle of the residual mean meridional circulation in the stratosphere, *J. Geophys. Res., 100*, 5173–5191, 1995.

Rosenlof, K.H., A.F. Tuck, K.K. Kelly, J.M. Russell III, and M.P. McCormick, Hemispheric asymmetries in water vapor and inferences about transport in the lower stratosphere, *J. Geophys. Res., 102*, 13,213–13,234, 1997.

Schoeberl, M.R., A.E. Roche, J.M. Russell III, D. Ortland, P.B. Hays, and J.W. Waters, An estimation of the dynamical isolation of the tropical lower stratosphere us-

ing UARS wind and trace gas observations of the quasi-biennial oscillation. *Geophys. Res. Lett.*, *24*, 53–56, 1997.

Sparling, L.C., J.A. Kettleborough, P.H. Haynes, M.E. McIntyre, J.E. Rosenfield, M.R. Schoeberl, and P.A. Newman, Diabatic cross-isentropic dispersion in the lower stratosphere, *J. Geophys. Res.*, *102*, 25,817–25,829, 1997.

Swinbank, R., and A. O'Neill, A stratosphere-troposphere data assimilation system, *Mon. Weather Rev.*, *122*, 686–702, 1994.

Thuburn, J., and M.E. McIntyre, Numerical advection schemes, cross-isentropic random walks, and correlations between chemical species, *J. Geophys. Res.*, *102*, 6775–6798, 1997.

Volk, C.M., et al., Quantifying transport between the tropical and mid-latitude lower stratosphere. *Science*, *272*, 1763–1768, 1996.

Wang, P.-H., P. Minnis, M.P. McCormick, G.S. Kent, and K.M. Skeens, A 6-year climatology of cloud occurrence frequency from Stratospheric Aerosol and Gas Experiment II observations (1985–1990), *J. Geophys. Res.*, *101*, 29,407–29,429, 1996.

Wang, R., K. Fraedrich, and S. Pawson, Phase-space characteristics of the tropical stratospheric quasi-biennial oscillation, *J. Atmos. Sci.*, *52*, 4482–4500, 1995.

Waugh, D.W., Seasonal variation of isentropic transport out of the tropical stratosphere, *J. Geophys. Res.*, *101*, 4007–4023, 1996.

Weare, B.C., and J.S. Nasstrom, Examples of extended empirical orthogonal function analysis, *Mon. Weather Rev.*, *110*, 481–485, 1982.

Weinstock, E.M., E.J. Hinsta, A.E. Dessler, and J.G. Anderson, Measurements of water vapor in the tropical lower stratosphere during the CEPEX campaign: Results and interpretation, *Geophys. Res. Lett.*, *22*, 3231–3234, 1995.

Zhang, C., On the annual cycle in highest, coldest clouds in the tropics, *J. Clim.*, *6*, 1987–1990, 1993.

T.J. Dunkerton and P.W. Mote, Northwest Research Associates, P.O. Box 3027, Bellevue WA 98009, (e-mail: mote@nwra.com; http://www.nwra.com/)

P.H. Haynes and M.E. McIntyre, Department of Applied Mathematics and Theoretical Physics, Cambridge University, CB3 9EW, England. (http://www.atmos-dynamics.damtp.cam.ac.uk/)

E.A. Ray, NOAA/CMDL Mail Stop R/E/CG1, 325 Broadway, Boulder, CO 80303.

J.M. Russell III, Department of Physics, Hampton University, Hampton VA 23668.

(Received September 18, 1997; revised December 24, 1997; accepted December 30, 1997.)

ROSSBY WAVE PROPAGATION

JOURNAL OF GEOPHYSICAL RESEARCH, VOL. 102, NO. D16, PAGES 19,461–19,469, AUGUST 27, 1997

Interaction of extratropical Rossby waves with westerly quasi-biennial oscillation winds

Donal O' Sullivan
Northwest Research Associates, Incorporated, Bellevue, Washington

Abstract. The role of laterally radiating stratospheric Rossby waves from the winter hemisphere in the momentum balance of the quasi-biennial oscillation (QBO) remains an unresolved issue. Observations of extratropical Rossby waves penetrating close to the equator suggest that Rossby wave absorption in the tropics must occur at least occasionally. This paper presents numerical simulations using a global shallow water model to examine the pattern of wave absorption at low latitude during the westerly wind phase of the QBO. Earlier results indicating that extratropical Rossby waves radiating to the equator do not break there when the QBO phase is westerly are reproduced. It is shown that the westerly QBO jet can persist, undiminished at its core, over seasonal length integrations, because the laterally radiating Rossby waves are absorbed along the QBO jet's flanks, where easterly acceleration occurs. The net effect of the Rossby waves on the westerly QBO jet is a reduction in the width of its meridional profile but not its core strength. This behavior is interpreted by considering the filtering of equatorward radiating Rossby waves by critical layer absorption, a process that depends on the background zonal mean wind and the waves' phase speed and amplitude. The simulations also show that adequate horizontal resolution is needed to capture the suppression of wave breaking at the QBO jet core and persistence of the jet core strength over seasonal timescales. The implications of this result for simulations of the QBO in general circulation models are considered.

1. Introduction

Planetary Rossby waves in the stratosphere radiate upward and equatorward from their tropospheric sources during the winter season. Their wave breaking and absorption at low and middle latitudes lead to the formation of the isentropically well mixed surf zone in the stratosphere. Though most equatorward radiating Rossby waves are absorbed at low latitudes, the absorption process must not be complete, as extratropical Rossby waves have been observed at the equator [*Hitchman et al.*, 1987].

Radiation of some extratropical Rossby waves into the tropics is also suggested by the occurrence of a robust correlation between the winter extratropical circulation and the phase of the quasi-biennial oscillation (QBO). The tendency is for the winter stratospheric vortex to be stronger and colder during winters, when the QBO phase is westerly rather than easterly [*Holton and Tan*, 1980, 1982; *Wallace and Chang*, 1982; *Labitzke*, 1982, 1987; *van Loon and Labitzke*, 1987; *Baldwin and Dunkerton*, 1991; *Dunkerton and Baldwin*, 1991]. Stratospheric Rossby waves have been shown to play a role in this tropical extratropical coupling [*Dunkerton and Baldwin*, 1991]. This finding raises a paradox, however, as the observed QBO winds do not show any evidence for wave absorption during either winter season, yet the QBO winds somehow influence the Rossby wave activity so as to modulate the extratropical Rossby wave activity. Similarly, given the long timescale of the QBO, it is apparent that the survival of the narrow westerly wind jet depends upon Rossby wave absorption not occurring in the westerly jet core, particularly at lower stratospheric levels, where the westerly QBO phase is of longer duration.

The purpose of this paper is to discuss the propagation of stratospheric extratropical Rossby waves into the tropics during periods with QBO westerlies. It will be shown that wave breaking is not expected within the zone of westerlies as a result of the absence of any Rossby waves possessing a critical latitude there. This occurs because easterly or weak westerly winds, which typically occur equatorward of the polar night jet, act to filter out those Rossby waves whose phase speeds match the QBO westerlies.

2. Background

Observations show that QBO westerlies are narrow and appear unaffected by Rossby wave absorption during solstitial seasons [*Dunkerton and Delisi*, 1985; *Naujokat*, 1986], suggesting tropical isolation from extrat-

Paper number 97JD01524.
0148-0227/97/97JD-01524$09.00

ropical Rossby wave breaking. Indeed, it has long been known that laterally propagating extratropical Rossby waves do not play a major role in forcing the QBO [*Wallace and Holton*, 1968], a view supported by recent numerical calculations, which show that reasonable idealized QBO-like cycles can be simulated without the need for such westward forcing [*Dunkerton*, 1997].

It is still possible, however, that extratropical Rossby waves contribute significantly to the QBO's momentum budget [*Dunkerton*, 1983; *McIntyre*, 1994]. It is notable that numerical models readily display Rossby wave radiation to the equator [*Juckes and McIntyre*, 1987; *O'Sullivan and Salby*, 1990; *O'Sullivan and Dunkerton*, 1994; *Waugh et al.*, 1994; *Polvani et al.*, 1995], though the wave flux is sensitively dependent on the subtropical zonal mean wind profile in the winter subtropics [*Polvani et al.*, 1995; *Chen*, 1996]. Thus there is great uncertainty surrounding the interaction of the QBO and Rossby waves from the winter hemisphere.

The present study examines this issue, motivated by the tracer transport study of *O'Sullivan and Chen* [1996], which investigated how the QBO affects isentropic transport at low latitudes over a solstitial season. Horizontal winds from the 650 K level of a three-dimensional middle atmospheric simulation were used to advect a tracer. Comparing simulations in which the model had either an easterly or a westerly QBO phase, they showed a well-mixed stratospheric surf zone forming at low latitudes for each QBO phase. The westerly QBO phase simulation was interesting, however, in that a second, smaller wave-breaking zone developed in the summer hemisphere at low latitudes. This effect was again seen in a barotropic simulation by *Chen* [1996]. This secondary wave-breaking zone was due to winter hemisphere Rossby waves propagating across the equator from the winter hemisphere. Wave breaking was dramatically suppressed in the westerly QBO jet at the equator, however.

The results of *O'Sullivan and Chen* [1996] suggest a possible solution to the puzzle of why Rossby waves reaching the equator do not break and decelerate the narrow QBO westerlies (~10° half width [*Newell et al.*, 1974]), in spite of the tropical winds exerting a strong influence on the interannual variability of the extratropical winter circulation [*Holton and Tan*, 1980, 1982]. The pattern of wave breaking seen at low latitudes by O'Sullivan and Chen can be explained by considering the selective absorption of southward radiating Rossby waves as they approach their critical latitude (where the zonal mean wind matches the wave's phase speed) and by considering the latitudinal profile of the zonal mean wind [*Randel and Held*, 1991; *Bowman*, 1996]. Most extratropical Rossby waves have eastward phase speed or are quasi-stationary and break in the weak westerlies or easterlies normally present in the winter subtropics. (The wave breaking is dependent on wave amplitude as well as intrinsic phase speed [*Fyfe and Held*, 1990].) The waves that propagate southward past the weak wind zone into the QBO westerlies and across the equator will not encounter a critical latitude until they reach the summer easterlies. Thus filtering of southward propagating Rossby waves by the weak winds of the winter subtropics prevents Rossby wave breaking in the QBO westerlies. This shielding effect may explain how narrow QBO westerlies can survive for periods longer than a year in the low and middle stratosphere. The Rossby waves that penetrate the tropics have critical latitudes in the summer hemisphere low latitudes, not in the westerly QBO winds.

To illustrate this effect, the zonal mean wind, $\bar{u}$, for January 1993 is shown in Figure 1, using the United Kingdom Meteorological Office (UKMO) assimilated winds. This shows the strong polar night jet at high latitudes in the winter hemisphere, while at the equator a westerly QBO jet is seen, slightly displaced into the winter hemisphere. (Singapore observations show that January 1993 had QBO westerlies stronger than 15 ms^{-1} from about 30 to 10 mbar.) The surf zone occupies the region of weak meridional potential vorticity (PV) gradient from about 20°N to the polar jet core. The zonal mean winds near 20°-30°N appear unusually strong for this January in comparison with climatology [*Dunkerton and Delisi*, 1985; *Randel*, 1992]. This profile nevertheless illustrates the point: since linearly propagating Rossby waves require westward intrinsic phase speed, $c_{Rw} - \bar{u} < 0$, waves radiating towards the equator from the winter extratropics will reach a critical latitude and will be absorbed before reaching the equator, unless their phase speed, c_{Rw}, is less than the zonal mean wind's local minimum in the winter subtropics, $\bar{u}_{min}$, i.e., $c_{Rw} < \bar{u}_{min}$. Rossby waves satisfying this criterion can radiate into the southern hemisphere until they reach their critical latitude. During January 1993, for example, Figure 1 indicates that southward radiating linear Rossby waves, with a broad phase speed spectrum, will show critical latitude absorption at latitudes north of the zonal wind minimum near 22°N and south of about 5°S (where $\bar{u} = \bar{u}_{min}$). The zone between 5°S and 22°N is sheltered from Rossby wave absorption.

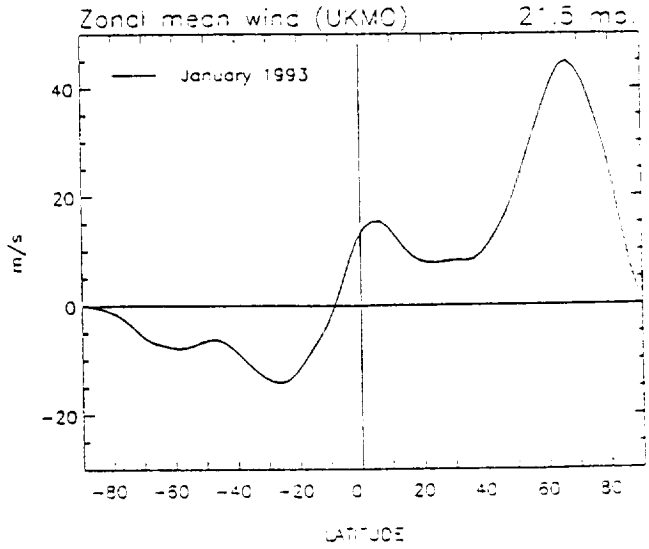

Figure 1. Zonally averaged UKMO assimilated zonal wind at 21.5 mbar, averaged over January 1993, during the westerly phase of the QBO.

however, in linear theory. Thus the isolated westerly QBO jet maximum does not experience wave breaking or wave drag. In reality, the filtering of Rossby waves will be more efficient, as finite amplitude Rossby waves will break before reaching their critical latitude [*Fyfe and Held*, 1990; *Waugh et al.*, 1994], so radiation to the equator past the wind minimum requires finite amplitude waves to have a westward intrinsic phase speed there, $c_{Rw} - \bar{u}_{min} < \delta < 0$, where $|\delta|$ increases with incident wave amplitude.

The sensitivity of Rossby wave propagation and absorption at low latitudes to the zonal mean wind was recently discussed by *Polvani et al.* [1995] and *Chen* [1996]. *Polvani et al.* [1995] performed simulations of the northern winter stratosphere, using a shallow water model similar to that described below. They concluded from their simulations (which had tropical easterlies) that confinement of wave breaking to the main surf zone was a consequence of strong subtropical shear of the zonal mean wind.

Chen [1996] undertook similar simulations with a non-divergent barotropic model and emphasized the importance of the subtropical winds in determining how active the winter hemisphere surf zone mixing was. In particular, he showed that the QBO may or may not have a significant influence on the extratropical circulation in the lower stratosphere, depending on the mean zonal winds in the winter hemisphere subtropics. The results presented here are consistent with the results of these earlier papers concerning the importance of the winter hemisphere's zonal mean wind.

The objective here, however, is to clarify the nature of extratropical Rossby waves' interaction with a westerly QBO jet, while the extratropical winds evolve in response to wave absorption. The filtering of equatorward radiating Rossby waves by the background winds and the absence of wave breaking in an isolated westerly QBO-like jet is demonstrated next in a shallow water model simulation representative of the solstitial stratosphere.

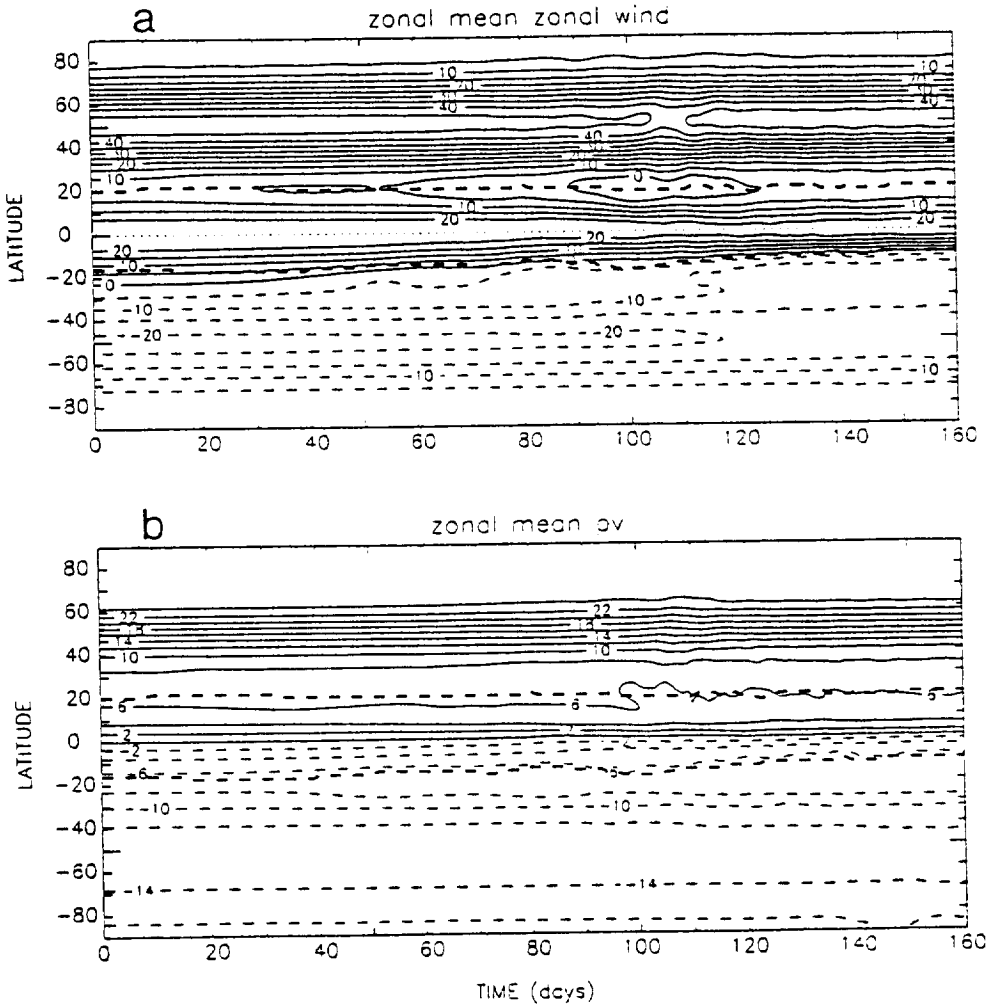

Figure 2. Evolution of the modeled (a) zonal mean wind and (b) potential vorticity, when the Rossby wave forcing amplitude, $h_B = 300$ m. The heavy dashed line in the northern hemisphere shows the location of the subtropical wind minimum, $\bar{u}_{min}$, while the line in the southern hemisphere demarks the latitude at which $\bar{u} = \bar{u}_{min}$. Rossby waves radiating from the winter extratropics do not encounter a critical latitude within this sheltered zone, where linear theory predicts no wave absorption. Units are (a) m s^{-1} and (b) 10^{-9} m^{-1} s^{-1}.

3. Numerical Simulations

3.1. Response of the QBO to Lateral Rossby Wave Radiation

A two-dimensional (2-D) global shallow water model has been used to demonstrate the behavior of extratropical Rossby waves radiating into the tropics during westerly QBO phase. Two-dimensional models such as this one have been used previously to study the quasi-horizontal dynamics and transport associated with stratospheric Rossby waves and the polar vortex. They may be viewed as representing flow on a quasi-horizontal isentropic surface or the vertically integrated flow of a layer of the stratosphere [*Juckes and McIntyre*, 1987; *Salby*, 1988; *Salby et al.*, 1990]. A 2-D shallow water model is ideally suited to the present study, as it is horizontal wave propagation and breaking that is of interest. The westerly phase of the QBO has large amplitude from near the 50 mbar (~21 km) level to above 5 mbar (where it merges with a westerly phase of the semiannual oscillation). The model may therefore be considered to represent the vertically integrated flow of any sublayer within this altitude range. The interaction of extratropical Rossby waves with QBO should be stronger near the middle stratosphere than near the lower stratosphere, however, since Rossby wave amplitudes increase exponentially with altitude.

The model used here is the spectral transform shallow water model of *Hack and Jakob* [1992], available from the National Center for Atmospheric Research and slightly modified as described below. The vorticity, divergence and continuity equations are integrated forward in time by using explicit, centered differencing time integration. The model is used with horizontal resolution T-85, a time step of 180 s, and a global mean depth of 8 km. The simulation is adiabatic, except for sixth-order hyper diffusion, which is included to control the enstrophy cascade near the limit of resolution. The diffusion coefficient is chosen to give an e-folding damping time of 1 hour at the smallest scales. The model is initialized with a zonally symmetric flow typical of the midwinter and is run for 120 days. Rossby wave forcing is imposed by introducing zonal wave one topography, $h_T(x, y)$, having a Gaussian latitudinal profile centered at 55°N, with a half width of 12.6° and having amplitude h_B. The forcing varies in time as $h(t) = h_T(1 - \exp(-t/\tau))(1 - \exp((t - 130))/\tau))$ until day 130 and is zero thereafter, where t is time in days and τ is 5 days. Thus the forcing amplitude is smoothly increased to a constant value over the first 10 days or so and smoothly turned off between day 120 and day 130. Simulations with this idealized adiabatic model are used to study the propagation of Rossby waves from the winter extratropics and their interaction with a QBO westerly jet at the equator. The QBO jet is specified in the initial conditions, but no QBO forcing is included during the simulation in order to highlight the interaction of the Rossby waves with the QBO jet. The disturbed polar vortex is mainly of interest as a source of equatorward radiating Rossby waves; thus obtaining the most realistic simulation of the extratropical stratospheric circulation is not a primary concern here. The model approximately simulates quasi-horizontal stratospheric flow. No parameterization of tropical wave forcing is included, so the QBO is not explicitly forced.

A simulation having zonal wave one topography with $h_B = 300$ m is first shown to discuss the behavior of weak lateral Rossby wave radiation into the tropics, followed by a more strongly forced case, $h_B = 900$ m. Both of these simulations demonstrate the tendency for the tropical westerly jet core to survive despite lateral Rossby wave radiation from the winter extratropics. Figure 2 shows the evolution of the zonal mean wind and potential vorticity when $h_B = 300$ m. This weakly forced case shows the zonal mean polar night jet to be barely affected by the Rossby wave forcing. The forced extratropical Rossby waves radiate equatorward, where wave breaking in the weak westerlies of the winter subtropics creates a well-mixed subtropical surf zone of homogenized PV and westward zonal mean acceleration. As *O'Sullivan and Chen* [1996] observed, a weaker secondary surf zone develops in the summer subtropics, between 10° and 20°S, due to the absorption of Rossby waves from the winter hemisphere extratropics. Westward propagating Rossby waves radiated into the southern hemisphere were also noted in the simulations of *Polvani et al.* [1995] and *Chen* [1996].

Thus wave breaking and zonal mean deceleration occur at low latitudes on both sides of the tropical westerly jet, but very little deceleration occurs at the jet core. The westerly jet core at the equator does experience a temporary, reversible deceleration of up to ~5 ms^{-1} during the simulation, however, due to the presence of nonbreaking Rossby wave activity there. The wind speed at the jet core relaxes back toward its initial value after day 130, when wave forcing is turned off, as wave amplitudes diminish. The jet core does not completely regain its initial strength by the end of the simulation, however, as the isolated westerly jet and its strong PV gradient act as a waveguide containing some Rossby wave activity, which is slow to decay.

Latitudinal profiles of zonal mean wind during the simulation, shown in Figure 3, are helpful for highlighting the regions of wave mean flow interaction. The northern hemisphere subtropics experiences continual deceleration during the first 120 days but strengthens again slightly after the wave forcing is turned off. Westward acceleration occurs in the southern hemisphere subtropics around the latitude at which $u = \bar{u}_{min}$, as expected. Rossby waves with westward intrinsic phase speed at the northern subtropical wind minimum, $c_{Rw} < \bar{u}_{min}$, are freely radiating into the southern hemisphere and cause the eastward acceleration farther south where their critical latitudes occur, for example, over the range ~10°S to ~40°S during the period from day 80 to day 120. Wave propagation south of ~40°S is negligible. The net effect of the extratropical Rossby waves on the QBO westerly jet has been to make the jet narrower on both sides. Continued encroachment of the southern hemispheric easterlies into the QBO westerly jet is halted by the deepening of the northern hemisphere subtropical wind minimum, which

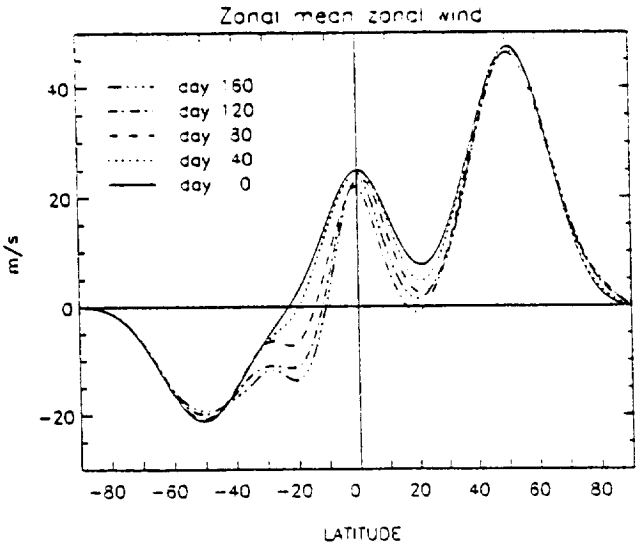

Figure 3. Latitudinal profiles of the modeled zonal mean wind in the simulation with the Rossby wave forcing amplitude, h_B, = 300 m.

effectively blocks lateral radiation of stationary Rossby waves into the tropics by day 120. The westward propagating Rossby waves are not directly forced in this model but are apparently generated by the large-scale wave breaking in the surf zone [*Polvani et al.*, 1995; *O'Sullivan and Chen*, 1996].

The numerical simulation indicates that the linear view of wave breaking determined by $\bar{u}(o)$ and c_{Rw} is modified by nonlinearity. On day 40, for example, southward radiating linear waves with appropriate phase speeds would find critical latitudes at northern latitudes down to ~21°N, the latitude of the subtropical wind minimum $\bar{u}_{min}$, but not again until about 15°S and southward, where $\bar{u} < \bar{u}_{min}$ again. The simulation shows, however, that deceleration occurs within the "sheltered zone" of linear theory. This effect is due to the finite width of finite amplitude critical layers, which PV maps show extending into the linearly "sheltered zone", so wave breaking reaches closer to the jet core than would be expected from linear theory. Secondary circulations induced by wave breaking may also extend the deceleration beyond the breaking zone.

The PV field (Figure 2) shows that the meridional PV gradient near the equator steepens as a result of the growth of subtropical surf zones on either side. This stronger gradient is associated with narrowing of the westerly jet's meridional profile, as there is no strengthening of the jet core speed.

This simulation is next compared with a more strongly forced case, h_B = 900 m, in which wave amplitudes are

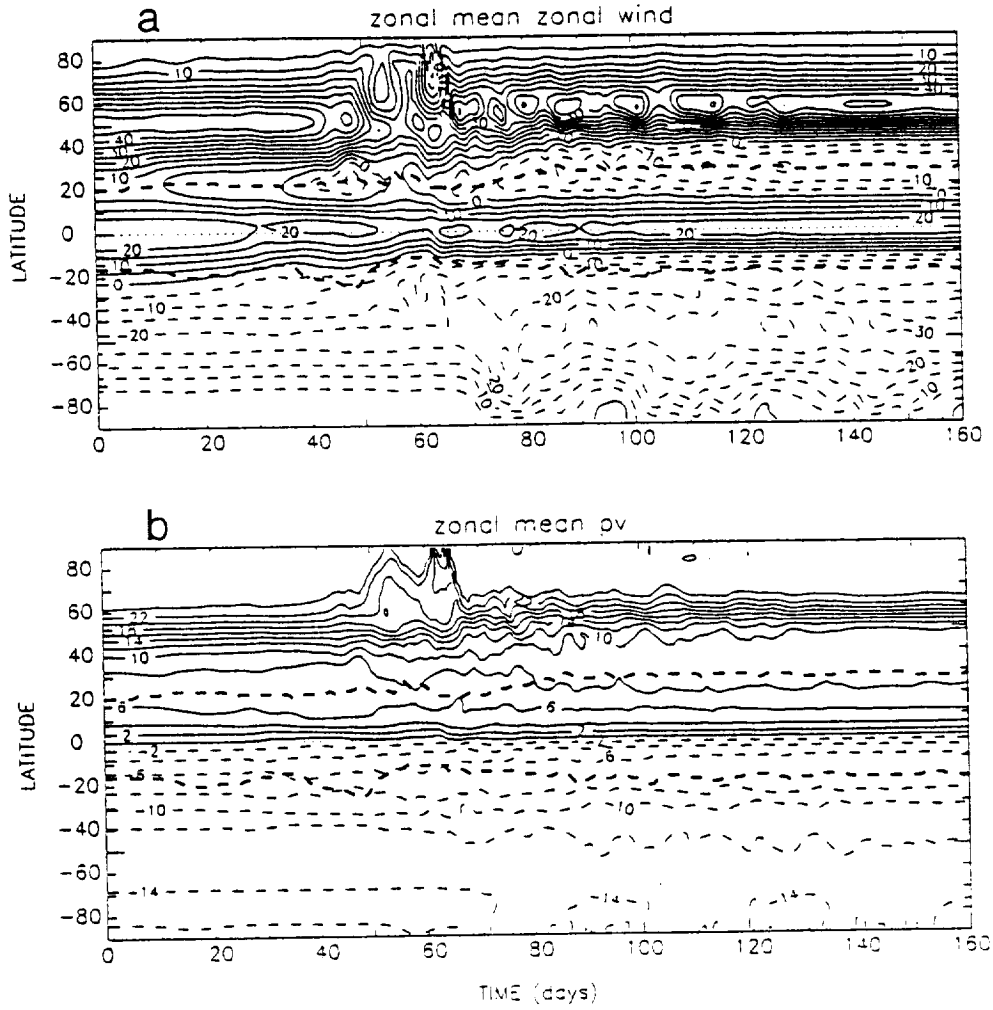

Figure 4. As in Figure 2 but with h_B = 900 m.

more representative of the winter stratosphere, to judge from the disturbance to the polar vortex. The evolution of the zonal mean wind and PV are shown in Figure 4 and wind profiles are shown in Figure 5. In this case the stronger forcing strongly disrupts the winter vortex, causing minor "polar stratospheric warming events" between days 50 and 70. Subsequently, the vortex reestablishes itself near the pole and experiences minor disruptions until forcing is turned off between day 120 and day 130. The stronger wave forcing leads to greater wave absorption and zonal mean easterly acceleration in the winter subtropics, with strongest easterlies of about -16 ms^{-1} developing near 30°N. This compares with approximately -3 ms^{-1} when h_B = 300 m. The PV field (Figure 4b) correspondingly shows a wider, more active subtropical surf zone when the forcing is stronger. The summer hemisphere extratropics show that wave breaking and PV mixing extend to the pole following the northern hemisphere's polar warming event. *Polvani et al.* [1995] and *Chen* [1996] noted similar wave breaking extending to high latitudes in the summer hemisphere. The southern hemisphere extratropics experiences much more easterly acceleration than occurred in the weakly forced case. The most striking feature of this simulation, though, is the preservation of the QBO westerly jet despite the stronger lateral Rossby wave radiation from the winter hemisphere. Aside from transient zonal mean decelerations the jet core experiences very little net deceleration over the course of the simulation.

The easterly acceleration in the winter subtropics plays an important role in isolating the tropical westerlies from wave breaking as it increases the range of Rossby wave phase speeds, which are absorbed and prohibited from radiating into the tropics. The value of $\overline{u}_{min}$ determines the phase speed filter cutoff for equatorward Rossby wave radiation, so a more westward $\overline{u}_{min}$ reduces the fraction of the extratropical Rossby waves that can reach the tropics, whereupon their fate depends strongly on the phase of the QBO. It is the value of $\overline{u}_{QBO} - \overline{u}_{min}$ that is of most relevance to the absence of wave breaking at the jet core, however. At the equator, increased westerly jet speed, u_{QBO}, implies increased intrinsic phase speed for the Rossby waves that can reach the equator, thus making it increasingly difficult for wave breaking and mean flow forcing to occur [*Fyfe and Held*, 1990]. In these simulations the quantity $\overline{u}_{QBO} - \overline{u}_{min}$ is initially about 16 ms^{-1}, a reasonably realistic value.

The QBO profile used here is unrealistically strong at 25 ms^{-1} but is chosen to highlight the pattern of wave absorption associated with a westerly QBO jet. An additional simulation is presented next to examine how sensitively the jet's isolation depends on the value of $\overline{u}_{QBO}$. The strongly forced simulation is repeated identically, except that the westerly QBO jet is weakened: $\overline{u}_{QBO}$ = +10 ms^{-1}. The profiles of zonal mean wind (Figure 6) show that the westerly QBO jet core still survives undiminished, even though $\overline{u}_{QBO} - \overline{u}_{min} \sim +5$ ms^{-1} initially. The QBO jet survives, because easterly acceleration in the winter subtropics rapidly increases $\overline{u}_{QBO} - \overline{u}_{min}$, giving a value of about +20 ms^{-1} by day 40. In this simulation the northern hemisphere subtropical zonal wind decelerates more rapidly and becomes more easterly than it does in the case with a $\overline{u}_{QBO}$ = +25 ms^{-1} jet. This behavior has the effect of absorbing and filtering out more of the southward radiating Rossby waves, so the southern hemisphere experiences less Rossby wave absorption and easterly acceleration.

The simulations highlight the difficulty Rossby waves have in decelerating the QBO westerly jet core: Filtering by the subtropical wind minimum removes Rossby waves with critical latitudes near the QBO jet core, so wave breaking can only occur there if wave amplitudes are large. Large amplitude, laterally radiating Rossby waves, will first break in the subtropics, however, further protecting the tropics by making $\overline{u}_{min}$ more easterly.

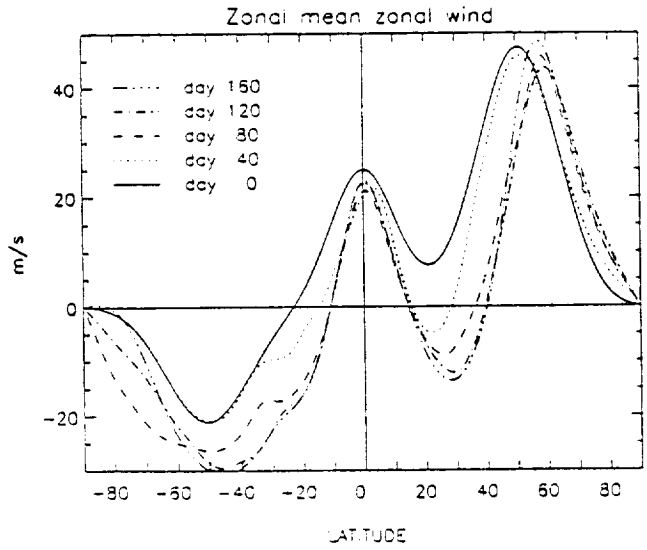

Figure 5. As in Figure 3 but with h_B = 900 m.

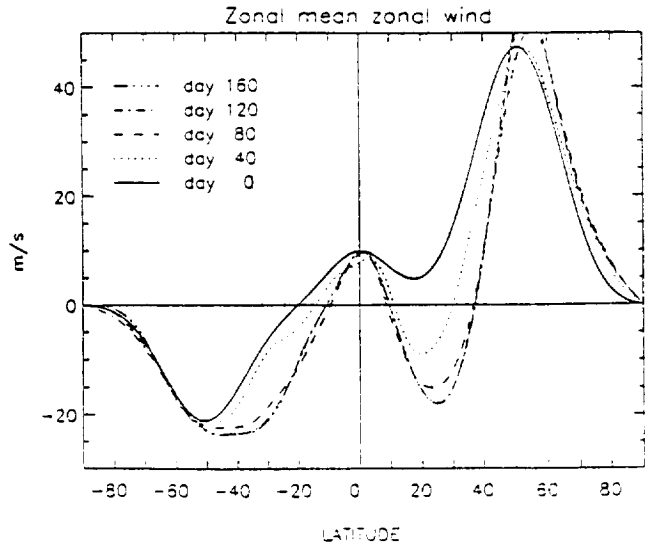

Figure 6. As in Figure 5 but with $\overline{u}_{QBO}$ = +10 m s^{-1}.

3.2. Sensitivity of QBO Simulations to Model Resolution

These simulations also raise the issue of model resolution requirements in simulating the westerly QBO phase, if extratropical Rossby waves radiate into the tropics as simulated in barotropic models or in the 3-D model of *O'Sullivan and Chen* [1996].

The importance of model resolution for the westerly QBO jet is dramatically shown by repeating the first simulation (h_B = 300 m) unchanged but with horizontal resolution reduced from T85 to T42. Small-scale dissipation must be increased for the lower T42 simulation, where a coefficient value of $\nu^6 = 6.30 \times 10^{27}$ m^6 s^{-1} is used compared to $\nu^6 = 4.75 \times 10^{25}$ m^6 s^{-1} before. Figure 7 contains meridional profiles of $\bar{u}$ during the simulation showing that the westerly QBO jet is essentially destroyed. A similar result was found in a T42 version of the second simulation (h_B = 900 m). The zonal mean momentum budget for this run shows that the loss of the westerly QBO jet is not due to the model's small-scale dissipation acting directly on the zonal mean, however. The reason for the different evolution from the T85 case is related to the effect of increased small-scale dissipation on wave absorption at low latitudes, by broadening the meridional width of the absorbing zone in comparison with that found when small-scale dissipation is weaker. The broadened subtropical wave-breaking zones on both sides of the QBO jet gradually weaken the jet, slowly at first but more rapidly by day 100, in a manner not seen in the less dissipative T85 simulations. This sensitivity to resolution is a subtle effect, which is not so apparent in shorter (~80 day) integrations. The effect should, nevertheless, be important in longer simulations of the QBO and may help explain some of the difficulties experienced in trying to produce a spontaneous QBO in general circulation models.

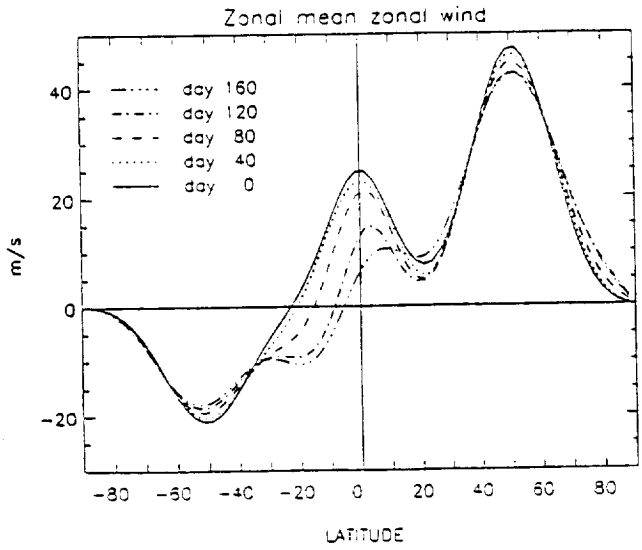

Figure 7. As in Figure 3 but with small-scale dissipation increased for this lower-resolution (T42) simulation.

4. Discussion

The modeled northern hemisphere Rossby wave forcing generates a considerable amount of westward traveling Rossby wave activity, especially later in the simulations, which radiate into the summer hemisphere and account for the strong forcing of the summer hemisphere by lateral Rossby wave radiation. (In the absence of these westward Rossby waves the summer subtropical wind minimum would not experience wave absorption and mixing [*Bowman and Hu*, 1997].) It is difficult to gauge which Rossby wave forcing strength is most appropriate for comparison with the middle and lower stratosphere. The strong forcing, h_B = 900 m, causes more realistic perturbations to the extratropical flow than occurs with the weaker forcing, h_B = 300 m. On the other hand, comparison of the winter subtropical deceleration suggests that the weaker forcing is more realistically representing equatorward Rossby wave radiation intensity. In addition, the simulation with stronger forcing shows too much Rossby wave radiation into the summer hemisphere judging by the westward acceleration there (Figure 5 and Figure 1), while the simulation with weaker forcing is more modest and apparently realistic (Figure 3). The Rossby wave perturbation amplitudes in the summer subtropics of the weaker forced case are also more consistent with analysis of cross-equatorial Rossby wave radiation deduced from UARS constituent data [*O'Sullivan*, 1997].

The shielding of the deep tropics from extratropical Rossby wave breaking during the westerly QBO phase is consistent with the long survival of the water vapor "tape recorder effect" [*Mote et al.*, 1996; *Holton et al.*, 1995]. This annually varying water vapor mixing ratio signal is imprinted at the tropopause and advected upward through the tropical lower stratosphere by the large-scale upwelling circulation. As with the westerly QBO winds themselves, this signal would be quickly destroyed by Rossby wave breaking and irreversible mixing in the tropics.

Meridional advection across the equator was negligible in these adiabatic simulations. This finding is acceptable, however, considering the weak contribution meridional advection makes to the zonal mean budget of PV or a long-lived tracer in the tropical stratosphere below 10 mbar [*Dunkerton*, 1996].

5. Conclusions

Idealized simulations of extratropical stratospheric Rossby waves radiating to the tropics during the QBO's westerly phase show that the equatorial core of the QBO westerly jet is remarkably unaffected by the incident Rossby waves, with the maximum wind speed essentially unchanged over the duration of the simulation. The QBO is unforced and free to evolve in response to Rossby wave absorption in these simulations. Although most of the winter hemisphere's extratropical Rossby wave activity is absorbed in the winter subtropical surf zone, a significant fraction traverses the QBO jet before being absorbed in the summer hemisphere subtropics.

Thus the flanks of the QBO jet in both hemispheres experience westward acceleration in response to Rossby wave absorption. The net effect of this is that the QBO jet becomes narrower meridionally during solstitial seasons than it was initially. There is evidence of such behavior in assimilated UKMO zonal mean wind data for the middle and lower stratosphere during the westerly QBO phase, which was centered on the northern winter of 1992-1993 (not shown). It is not clear how significant this tendency is for determining the meridional width of westerly QBO phases, however.

The simulations presented here are interpreted in terms of the filtering effect of the winter subtropical zonal mean wind on equatorward radiating extratropical Rossby waves, as discussed by *Bowman* [1996]. This process depends on the background zonal mean wind as well as the waves' phase speed and amplitude. Thus the waves that reach the westerly QBO jet do not encounter critical latitudes until they reach the summer subtropics. In these simulations, and in reality, the subtropical weak zonal wind "filter" evolves to become more effective in shielding the tropics during winter as the subtropical wind minimum becomes more easterly. Hence wave propagation across the equator, when the QBO phase is westerly, is most likely in early winter. Analysis of UARS constituent fields at the 10 mbar level during the winter 1992-1993, where the QBO was westerly, shows that significant cross-equatorial radiation of quasi-stationary and westward propagating Rossby waves does occur, particularly in early winter, when the northern subtropical winds are more favorable to propagation [*O'Sullivan*, 1997].

These results help clarify the paradox of how the extratropical Rossby waves apparently interact with, and are influenced by, the QBO without the QBO itself, close to the equator, being noticeably affected by the Rossby waves. The QBO's westerly phases are long-lived and do not show evidence of easterly acceleration from Rossby wave absorption during winter season, according to long-term equatorial rawinsonde observations (e.g., Singapore, at 1°N). The simulations presented here have shown that the laterally radiating Rossby waves interact with the QBO but do not break near the westerly jet core, allowing the jet core to persist.

This work suggests the interaction of extratropical Rossby waves with westerly QBO winds, and communication of the QBO signal to the extratropical circulation, should be strongest in early winter (especially December). This is the time of year when the low-latitude stratospheric winds of the winter hemisphere (and $\overline{u}_{min}$) are most westerly and the extratropical Rossby waves are strong.

This paper has focused on the dynamical interaction of Rossby waves with the westerly QBO jet. The absence of wave breaking in the westerly QBO jet core implies a lack of horizontal mixing across the jet axis, which could manifest itself in long-lived constituent concentration fields as a cross-jet gradient if surf zone mixing reached close to the equator. The concentration of long-lived constituents usually does not show strong meridional gradient at the equator during westerly QBO, however, [e.g., *Roche et al.*, 1996], probably because the eddy-mixing rate usually increases gradually away from the equator. A case in which mixing did reach close to a westerly QBO jet, producing a strong meridional gradient of long-lived constituent at the equator, was seen at 10 mbar and above during late winter of 1992, however [*Dunkerton and O'Sullivan*, 1996].

Finally, the sensitivity of the westerly QBO jet's evolution to model resolution (i.e., small-scale dissipation strength) demonstrated here shows that high horizontal resolution may be required to capture the persistence of the westerly QBO jet when Rossby waves radiate into it from the winter extratropics. This conclusion depends on the simulated flux of Rossby wave activity radiating across the equator having reasonably realistic intensity, however, a quantity poorly known in reality. The fact that the westerly QBO jet was obliterated in the lower-resolution simulation even for the weakly forced case suggests that this conclusion is likely to be relevant for actual lateral Rossby wave radiation strengths.

Acknowledgments. This research was supported by the National Science Foundation (NSF), Grant ATM-9301105 and the National Aeronautics and Space Administration, Contract NAS5-32862. Numerical simulations were performed at the National Center for Atmospheric Research (NCAR), which is sponsored by the NSF. The author would like to thank NCAR for providing the barotropic model code used here, and the anonymous reviewers for their comments. Conversations with T. J. Dunkerton are gratefully acknowledged.

References

Baldwin, M. P. and T. J. Dunkerton, Quasi-biennial oscillation above 10 mb, *Geophys. Res. Lett.*, *18*, 1205-1208, 1991.

Bowman, K. P., Rossby wave phase speeds and mixing barriers in the stratosphere, Part 1; Observations, *J. Atmos. Sci.*, *53*, 907-916, 1996.

Bowman, K. P. and Y. Hu, The tropical mixing barrier in the GFDL SKYHI model, *Geophys. Res. Lett.*, in press, 1997.

Chen, P., The influences of zonal flow on wave breaking and tropical-extratropical interaction in the lower stratosphere, *J. Atmos. Sci.*, *53*, 2379-2392, 1996.

Dunkerton, T. J., Laterally propagating Rossby waves in the easterly acceleration phase of the quasi-biennial oscillation, *Atmos. Ocean.*, *21*, 55-68, 1983.

Dunkerton, T. J., The role of gravity waves in the quasi-biennial oscillation, *J. Geophys. Res.*, in press, 1997.

Dunkerton, T. J. and M. P. Baldwin, Quasi-biennial modulation of planetary wave fluxes in the northern hemisphere winter, *J. Atmos. Sci.*, *48*, 1043-1061, 1991.

Dunkerton, T. J. and D. P. Delisi, Climatology of the equatorial lower stratosphere, *J. Atmos. Sci.*, *42*, 376-396, 1985.

Dunkerton, T.J., and D. O'Sullivan, Mixing zone in the tropical stratosphere above 10 mb, *Geophys. Res. Lett.*, *23*, 2497-2500, 1996.

Fyfe, J., and I. M. Held, The two-fifths and one-fifth rules for Rossby wave breaking in the WKB limit, *J. Atmos. Sci.*, *47*, 697-706, 1990.

Hack, J. J., and R. Jakob, Description of a global shallow water model based on the spectral transform method, *NCAR Tech. Note, NCAR/TN-343+STR*, 1992.

Hitchman, M. H., C. B. Leovy, J. C. Gille, and P. L. Bailey, Quasi-stationary, zonally asymmetric circulations in the equatorial middle atmosphere, *J. Atmos. Sci.*, *44*, 2219-2236, 1987.

Holton, J. R., and H.-C. Tan, The influence of the equatorial quasi-biennial oscillation on the global circulation at 50 mb, *J. Atmos. Sci.*, *37*, 2200-2208, 1980.

Holton, J. R., and H.-C. Tan, The quasi-biennial oscillation in the northern hemisphere lower stratosphere, *J. Meteorol. Soc. Jpn.*, *60*, 140-148, 1982.

Holton, J. R., P. H. Haynes, M. E. McIntyre, A. R. Douglass, R. B. Rood, and L. Pfister, Stratosphere-troposphere exchange, *Rev. Geophys.*, *33*, 403-439, 1995.

Juckes, M. N., and M. E. McIntyre, A high-resolution one layer model of breaking planetary waves in the stratosphere, *Nature*, *328*, 590-596, 1987.

Labitzke, K., On the interannual variability of the middle stratosphere during northern winters, *J. Meteorol. Soc. Jpn.*, *60*, 124-139, 1982.

Labitzke, K., Sunspots, the QBO, and the stratospheric temperature in the north polar region, *Geophys. Res. Lett.*, *14*, 535-537, 1987.

McIntyre, M. E., The quasi-biennial oscillation (QBO): Some points about the terrestrial QBO and the possibility of related phenomena in the solar interior, in *The Solar Engine and Its Influence on the Terrestrial Atmosphere and Climate*, edited by E. Nesme-Ribes, pp. 293-317, Springer-Verlag, New York, 1994.

Mote, P. W., K. H. Rosenlof, M. E. McIntyre, E. S. Carr, J. C. Gille, J. R. Holton, J. S. Kinnersley, H. C. Pumphrey, J. M. Russell III, and J. W. Waters, An atmospheric tape recorder: The imprint of tropical tropopause temperatures on stratospheric water vapor, *J. Geophys. Res.*, *101*, 3989-4006, 1996.

Naujokat, B., An update of the observed quasi-biennial oscillation of the stratospheric winds over the tropics, *J. Atmos. Sci.*, *43*, 1873-1877, 1986.

Newell, R. E., J. W. Kidson, D. G. Vincent, and G. J. Boer, "The General Circulation of the Tropical Atmosphere and Interactions with Extratropical Latitudes," MIT Press, Cambridge, Massachusetts, 1974.

O'Sullivan, D., Cross-equatorially radiating stratospheric Rossby waves, *Geophys. Res. Lett.*, *24*, 1483-1486, 1997.

O'Sullivan, D., and P. Chen, Modeling the quasi-biennial oscillation's influence on isentropic tracer transport in the subtropics, *J. Geophys. Res.*, *101*, 6811-6822, 1996.

O'Sullivan, D., and T. J. Dunkerton, Seasonal development of the extratropical QBO in a numerical model of the middle atmosphere, *J. Atmos. Sci.*, *51*, 3706-3721, 1994.

O'Sullivan, D., and M. L. Salby, Coupling of the quasi-biennial oscillations and the extratropical circulation in the stratosphere through planetary wave transport, *J. Atmos. Sci.*, *47*, 650-673, 1990.

Polvani, L. M., D. W. Waugh, and R. A. Plumb, On the subtropical edge of the stratospheric surf zone, *J. Atmos. Sci.*, *52*, 1288-1309, 1995.

Randel, W. J., Global atmospheric circulation statistics, 1000-1 mb, *NCAR Tech. Note, NCAR/TN-366+STR*, 1992.

Randel, W. J., and I. M. Held, Phase speed spectra of transient eddy fluxes and critical layer absorption, *J. Atmos. Sci.*, *48*, 688-697, 1991.

Roche, A. E., et al., Validation of CH_4 and N_2O measurements by the cryogenic limb array etalon spectrometer instrument on the Upper Atmosphere Research Satellite, *J. Geophys. Res.*, *101*, 9679-9710, 1996.

Salby, M. L., Deep circulations under simple classes of stratification, *Tellus, Ser. A*, *41*, 48-65, 1988.

Salby, M. L., R. R. Garcia, D. O'Sullivan, and J. Tribbia, Global transport calculations with an equivalent barotropic system, *J. Atmos. Sci.*, *47*, 188-214, 1990.

van Loon, H., and K. Labitzke, The southern oscillation. Part V: The anomalies in the lower stratosphere of the northern hemisphere in winter and a comparison with the quasi-biennial oscillation, *Mon. Weather Rev.*, *115*, 357-369, 1987.

Wallace, J. M., and F.-C. Chang, Interannual variability of the wintertime polar vortex in the northern hemisphere middle stratosphere, *J. Meteorol. Soc. Jpn.*, *60*, 149-155, 1982.

Wallace, J. M., and J. R. Holton, A diagnostic numerical model of the quasi-biennial oscillation, *J. Atmos. Sci.*, *25*, 280-292, 1968.

Waugh, D. W., L. M. Polvani, and R. A. Plumb, Nonlinear, barotropic response to a localized topographic forcing: Formation of a "tropical surf zone" and its effect on interhemispheric propagation, *J. Atmos. Sci.*, *51*, 1401-1416, 1994.

D. O'Sullivan, Northwest Research Associates, Inc., P.O. Box 3027, Bellevue, WA 98009-3027. (e-mail: donal@nwra.com)

(Received October 8, 1996; revised February 3, 1997; accepted May 5, 1997.)

WATER VAPOR AND EQUATORIAL WAVES

GEOPHYSICAL RESEARCH LETTERS, VOL. 25, NO.13, PAGES 2445-2448, JULY 1, 1998

Sub-seasonal variations in lower stratospheric water vapor

Philip W. Mote and Timothy J. Dunkerton

Northwest Research Associates, Bellevue, Washington

Hugh C. Pumphrey

Department of Meteorology, University of Edinburgh

Abstract. Observations of water vapor with high temporal and spatial resolution and good horizontal coverage just above the tropical tropopause have been scarce, but a preliminary version of such data has been developed using radiance measurements of the Microwave Limb Sounder. These data reveal distinct variations with periods in the ranges 10–25 days and 30–70 days, consistent with (respectively) slow Kelvin waves and the tropical intraseasonal oscillation.

1. Introduction

Signatures of equatorial Kelvin waves were first found in lower stratospheric temperature [*Wallace and Kousky*, 1968] and have also been found in trace constituents using satellite data [*Canziani et al.* 1994; *Ziemke and Stanford* 1994]. By studying ozone and water vapor profiles from the Limb Infrared Monitor of the Stratosphere (LIMS), *Kawamoto et al.* [1997] identified Kelvin-wave signatures in the lower stratosphere, though for water vapor the results were compromised by poor-quality data in the lower stratosphere.

In addition to possible Kelvin-wave signatures in lower stratospheric water vapor, we also wish to investigate in this paper the possibility of a stratospheric signature of the tropical intraseasonal oscillation (TIO). For both kinds of sub-seasonal variations we turn to a relatively new water vapor data set from the Microwave Limb Sounder (MLS) instrument aboard the Upper Atmosphere Research Satellite (UARS). While MLS stratospheric water vapor data have previously been used in a number of studies, the data set used here is based on a new retrieval that extends the data down to 100 hPa, as explained in section 2. We analyze the spectral characteristics of sub-seasonal anomalies in MLS water vapor at the 100 and 68 hPa UARS levels.

2. Data

MLS measures water vapor in two spectral bands, 183 GHz and 205 GHz, with best sensitivity in the stratosphere and upper troposphere respectively. With the standard retrieval, the 183 GHz radiometer yields data at and above 46 hPa with a resolution of about 5 km. A nonlinear retrieval has been developed that extends the sensitivity to 100 hPa and doubles the vertical resolution; results from an earlier version of the nonlinear retrieval were presented and discussed by *Mote et al.* [1996]. The retrieval has been improved, primarily by eliminating systematic errors and by speeding up the code to allow all available days to be processed. The range of available days lies between late September 1991, the launch of UARS, and late April 1993, when the 183 GHz radiometer failed. There are several one-day gaps, a four-day gap, and a long gap in June–July 1992 when only a few days of data were taken. We bridge the shorter gaps by linear interpolation, and the long gap forces us to divide the record into two segments for most analyses.

In contrast to solar occultation instruments, MLS, because it measures emissions at the limb, can gather over 1300 profiles per day. We have formed a zonal, equatorial cross-section of water vapor data in time and longitude by binning profiles within 2.5° of the equator in 24° longitude bins for each day, after quality control. All equatorial data values at 100 hPa are flagged by the retrieval as suspicious (meaning that the error of the retrieved product is greater than one half of the error of the a-priori data) but are nonetheless reasonable in some respects: the seasonal variations agree with 100 hPa temperatures and with HALOE water vapor [*Mote et al.*, 1996]. The higher-frequency, zonally-varying fluctuations of MLS water vapor at 100 hPa also seem reasonable, and do not arise from the (zonal mean) a-priori data, but may be affected by the values at 68 hPa, the next UARS level above 100 hPa. To be on the safe side, we concentrate here on the data at 68 hPa.

3. Results

As shown by *Mote et al.* [1996], water vapor has a large annual cycle at the tropical tropopause. In fact, low-frequency variability accounts for more than 90% of the variance. In order to reveal the subtler signature of higher-frequency variations, we high-pass filter the data removing periods longer than about 90 days. We then remove variations in the zonal-mean component and consider two 256-day intervals, one on each side of the data gap in June–July 1992.

For the 68 hPa level (Figure 1a), a clear signature of mostly eastward-traveling disturbances emerges. Unlike the slower disturbances at 215 hPa reported by *Clark et al.* [1998], which usually vanished above the eastern Pacific, these disturbances occur at all longitudes, and sometimes circle the globe. For example, the positive anomaly (light shading) apparent near 0° at the end of September 1991 can be traced more than once around the globe, returning to 0° in mid-October and possibly again in early November.

In order to elucidate the characteristics of these oscilla-

Paper number 98GL51847.
0094-8534/98/98GL-51847$05.00

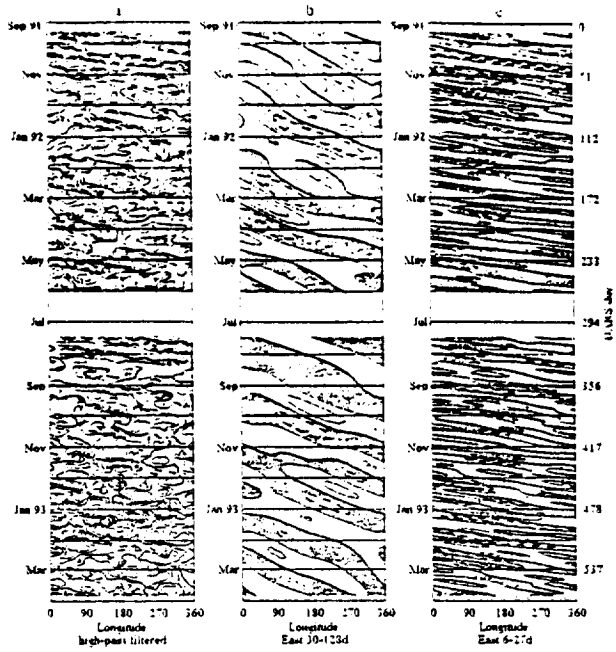

Figure 1. Hovmöller diagrams of (a) equatorial (2.5°S–2.5°N) 68 hPa water vapor, high-pass (period < 90d) filtered; (b) the same, reconstructed using only eastward wavenumbers 1–3 and temporal periods 30–128 days (see lower box in Figure 2a) and (c) as in (b) but for temporal periods 6–27 days (see upper box in Figure 2a). Dark shading indicates negative anomalies. Contour interval is 0.04 ppmv in (a) and (c), 0.02 ppmv in (b).

tions, we calculate wavenumber-frequency power spectra of the 256-day segments of data shown in Figure 1a and also of the corresponding data at 100 hPa. At each longitude the time series data are tapered at the endpoints to assure continuity when applying the spectral analysis. (The results are virtually identical without tapering.) Then the time-longitude data are regressed to find coefficients of terms like $\cos(kx - nt)$ where x and t are defined so that k and n are integers; k varies from -7 to 7 (since there are 15 grid points) and n varies from 1 to 128, corresponding to periods between 256 and 2 days.

The results are shown in Figure 2. The dominant spectral peaks are at eastward-traveling wavenumber 1 with periods between 10 and 70 days and a weak minimum at 30 days, suggesting a division into two spectral bands, 10–25 day period and 30–70 day period. We discuss the significance of these two bands separately, tentatively associating them respectively with Kelvin waves and with the tropical intraseasonal oscillation (TIO), also known as the Madden-Julian Oscillation.

3.1. 30–70 day band

Clark et al. [1998] studied MLS water vapor (from the 205 GHz channel) at 215 hPa: they too found considerable spectral power in the 30–70 day band, and identified it with the TIO. While a signature of the TIO in the lower stratosphere has not generally been acknowledged, it seems reasonable to identify the spectral peaks at 30–70 days at the 68 and 100 hPa levels (Figure 2) with those at 215 hPa, thus connecting them to the TIO as well. Figure 1b shows a reconstruction of the water vapor variations using the limited space-time coefficients enclosed in the lower dashed box in Figures 2a and 2b, that is, limited to wavenumbers 1–3 and to periods of 30–128d. Some features (e.g., in March 1992) clearly correspond to features in Figure 1a, and are anticorrelated with the variations at 215 hPa (figures not shown, but cf. *Clark et al.* [1998]).

The spectral power in the 30–70d band drops by approximately four orders of magnitude between 215 and 100 hPa, due partly to the corresponding decrease in water vapor mixing ratio, and another order of magnitude between 100 hPa and 68 hPa, where the mixing ratios are comparable. The attenuation with height is consistent with our interpretation of the variations at 100 and 68 hPa as an evanescent stratospheric response to the TIO.

3.2. 10–25 day band

In the 10–25 day spectral band, the disturbances are only attenuated by a factor of 2 between 100 and 68 hPa. The fact that shorter periods dominate at higher altitudes is consistent with the observations of *Canziani et al.* [1994] showing distinct spectral bands of slow (roughly 10–20 day), fast

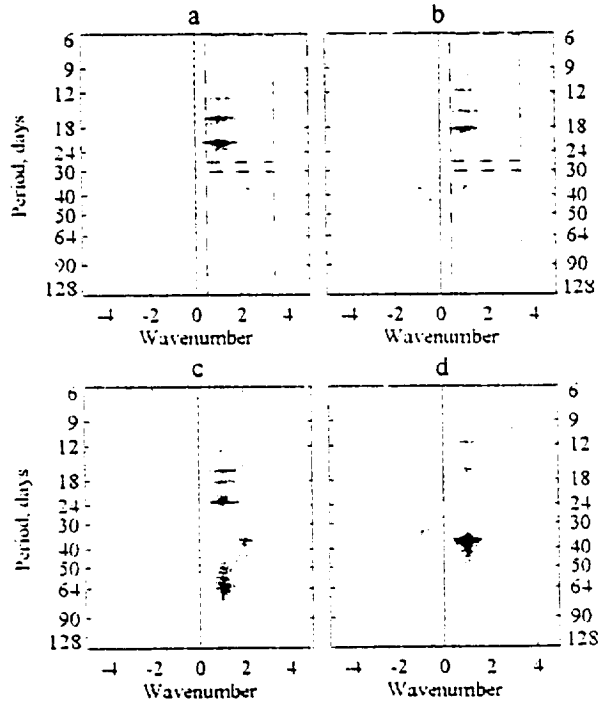

Figure 2. Power spectra, by wavenumber and frequency, of the water vapor variations shown in Figure 1a for 68 hPa (top two panels) and of the corresponding variations at 100 hPa (bottom two panels). Positive wavenumbers refer to eastward waves, and negative wavenumbers to westward waves. Figures 2a and 2c refer to the first 256-day interval in Figure 1, and figures 2b and 2d refer to the second interval in Figure 1.

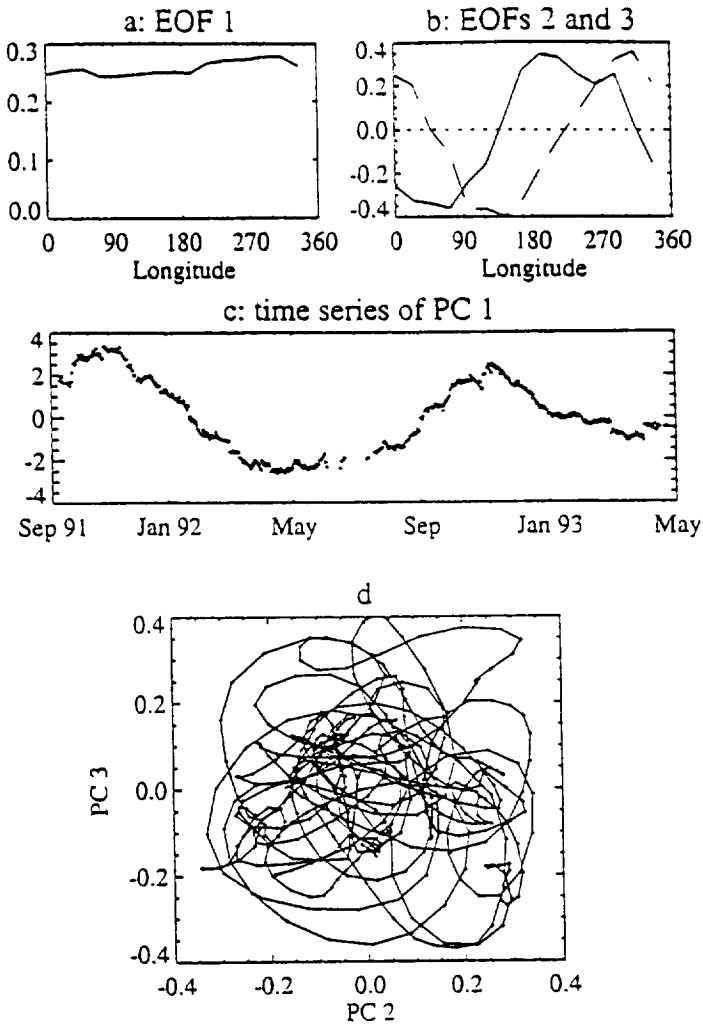

Figure 3. Empirical orthogonal functions of equatorial water vapor at 68 h Pa (a–b) and the time series of their principal components (c–d). In Figure 3b, EOF 2 is indicated by the solid curve, EOF 3 by the dashed curve. In Figure 3d, the (slightly smoothed) principal component time series of EOFs 2 and 3 are plotted against each other to emphasize their phase relationship.

(5–9 day), and ultrafast (3–4 day) waves; slow waves dominated in the lower stratosphere and fast waves in the middle and upper stratosphere (their figures 8 and 11). *Tsuda et al.* [1994] also found a roughly 20-day spectral peak in radiosonde data, confined mainly to the 15–20 km altitude range, and identified it as a Kelvin wave. We also find (figures not shown) that the equatorial water vapor disturbances at these levels are coherent with (but stronger than) disturbances at both higher latitudes and higher altitudes. These attributes, with the correct phase relationship, could be manifestations of Kelvin waves in the water vapor field, though the interpretation is complicated by the fact that the vertical gradient of water vapor typically changes sign twice between 100 and 10 hPa [see *Mote et al.*, 1996, their Plate 1].

To emphasize the contribution of the 10–25 day band to the variations shown in Figure 1a, we reconstruct the variations using only wavenumbers 1–3 and periods between 6 and 27 days (the upper dashed box in Figure 2). The results, shown in Figure 1c, highlight the coherence of features in this spectral band and provide an aid in interpreting Figure 1a. At times (e.g., September–November 1991) the resemblance between Figure 1c and Figure 1a suggests that the higher-frequency eastward disturbances predominate.

An alternative approach for isolating the eastward-traveling variations seen in Figure 1 is to calculate empirical orthogonal functions (EOFs). We do this for the entire data record (not just the two intervals of Figure 1) at 68 and 100 hPa separately; the results for 68 hPa are shown in Figure 3, and the results for 100 hPa (not shown) are very similar. The first EOF (Figure 3a) is nearly zonally symmetric and accounts for approximately 94% of the variance, and its associated time series (Figure 3c) represents the seasonal variation in the zonal mean; this seasonal variation is formed by the seasonally varying tropopause temperature, and advected upward as discussed by *Mote et al.* [1996]. The second and third EOFs (Figure 3b) each explain about 1% of the variance, have comparable eigenvalues, have wavenumber-1 structure, and are temporally in quadrature, as revealed by the prevalence of circular patterns in Figure 3d. These char-

acteristics all describe a conjugate pair of EOFs, indicating that they describe a traveling oscillation. Their time series indicate variations at a range of periods but mostly near 20 days, as shown by visual inspection and by spectral and autocorrelation analysis. The largest cross-correlation is at a lag of 4 days, indicating a combined period near 16 days.

4. Discussion

Tsuda et al. [1994] stated that "upward flux of water vapor...into the equatorial stratosphere can also be modulated by the activity of Kelvin waves." The variations in tropical tropopause temperature shown in their figure 17 (approximately 185K to 193K) correspond to a variation in saturation mixing ratio from 1.5 to 5 ppmv. MLS water vapor variations in the sub-seasonal frequency range, on the other hand, are only a few tenths of a ppmv; this discrepancy could be attributed to a number of causes, including the vertical resolution and sensitivity of the MLS retrieval.

It seems likely that the data at 100 hPa contain useful information not just at low frequencies, as already demonstrated by *Mote et al.* [1996], but also at sub-seasonal frequencies. These data provide an important link between lower stratospheric and upper tropospheric water vapor, a link that will be investigated further. In the present paper we have shown that sub-seasonal variations in lower stratospheric water vapor are probably due to the joint influence of slow Kelvin waves and the TIO, but we have not established that this interpretation is correct. Subsequent papers will investigate (1) the relationships of the Kelvin-wave signatures shown here to those in water vapor at higher levels, as well as to those in temperature; (2) the relationship between lower stratospheric and upper tropospheric water vapor in the 30–70 day band.

Acknowledgments. We are grateful to Bob Harwood for his input on this paper. Work in the U.S.A. was supported by NASA contracts NAS1-96071 and NAS5-32862, and work in the U.K. by NERC.

References

Canziani, P.O., J.R. Holton, E. Fishbein, L. Froidevaux, and J.W. Waters, Equatorial Kelvin waves: a UARS MLS view. *J. Atmos. Sci., 51,* 3053–3076, 1994.

Clark, H.L., R.S. Harwood, P.W. Mote, and W.G. Read, Variability of water vapor in the tropical upper troposphere as measured by the Microwave Limb Sounder. *submitted to J. Geophys. Res.,* 1998.

Kawamoto, N., M. Shiotani, and J.C. Gille, Equatorial Kelvin waves and corresponding tracer oscillations in the lower stratosphere as seen in LIMS data. *J. Meteorol. Soc. Japan, 75,* 763–773, 1997.

Mote, P.W., K.H. Rosenlof, M.E. McIntyre, E.S. Carr, J.C. Gille, J.R. Holton, J.S. Kinnersley, H.C. Pumphrey, J.M. Russell III, and J.W. Waters, An atmospheric tape recorder: The imprint of tropical tropopause temperatures on stratospheric water vapor. *J. Geophys. Res., 101,* 3989–4006, 1996.

Tsuda, T., Y. Murayama, H. Wiryosumarto, S.W.B. Harijono, and S. Kato, Radiosonde observations of equatorial atmospheric dynamics over Indonesia, 1. Equatorial waves and diurnal tides. *J. Geophys. Res., 99,* 10,491–10,505, 1994.

Wallace, J.M., and V.E. Kousky, Observational evidence of Kelvin waves in the tropical stratosphere. *J. Atmos. Sci., 25,* 900–907, 1968.

Ziemke, J.R., and J.L. Stanford, Quasi-biennial oscillation and tropical waves in total ozone. *J. Geophys. Res., 99,* 23,041–23,056, 1994.

T.J. Dunkerton and P.W. Mote, Northwest Research Associates, PO Box 3027, Bellevue WA 98009. (e-mail tim@nwra.com, mote@nwra.com)

H.C. Pumphrey, Department of Meteorology, University of Edinburgh, King's Buildings, Mayfield Road, Edinburgh EH9 3JZ UK. (e-mail hcp@met.ed.ac.uk)

(Received February 27, 1998; revised April 20, 1998; accepted May 8, 1998.)

JOURNAL OF GEOPHYSICAL RESEARCH, VOL. 103, NO. D24, PAGES 31,695-31,707, DECEMBER 27, 1998

Variability of water vapor in the tropical upper troposphere as measured by the Microwave Limb Sounder on UARS

H.L. Clark and R.S. Harwood

Department of Meteorology, University of Edinburgh, Scotland, United Kingdom

P.W. Mote[1]

Northwest Research Associates, Bellevue, Washington

W.G. Read

Jet Propulsion Laboratory, California Institute of Technology, Pasadena

Abstract. The Microwave Limb Sounder (MLS), an instrument on the Upper Atmosphere Research Satellite (UARS), measures water vapor in the upper troposphere, with best sensitivity at the standard UARS level at 215 hPa. In this paper, we analyze the MLS observations with a view to characterizing the temporal and zonal variations of upper tropospheric water vapor between 20°N and 20°S. Time series of water vapor throughout the tropics show a strong annual cycle with maximum amplitude at 20°N and 90°E. An intraseasonal cycle with a period of 30–85 days is evident over the Western Pacific at latitudes from 10°N to 20°S. The cycle is associated with eastward propagating disturbances of zonal wavenumbers 1–2, suggesting that this intraseasonal cycle is related to the Madden-Julian oscillation.

1. Introduction

Water vapor is a significant absorber and emitter of infrared radiation and is the most dominant greenhouse gas [e.g., *Houghton et al.*, 1990; *Jones and Mitchell*, 1991]. The response of the climate to increases in anthropogenic greenhouse gases depends upon the water vapor feedback, which is generally believed to be positive; increased global temperatures lead to an increase in water vapor, in turn contributing to further warming. *Lindzen* [1990] suggested that increased global temperatures and consequent increased convection may lead to a drying of the upper troposphere through subsidence, which could offset some warming. Some debate still surrounds this idea as more recent papers suggest [e.g., *Chou*, 1994; *Soden*, 1997; *Spencer and Braswell*, 1997] and the primary reason for the continuing uncertainty is the lack of adequate global water vapor measurements in the upper troposphere.

Historically, measurements of the water vapor field have relied upon radiosonde profiles; the accuracy and spatial extent of which are limited [e.g., *Elliot and Gaffen*, 1991; *Soden and Lanzante*, 1996]. Radiosonde profiles are confined largely to northern hemisphere landmasses with the result that the water vapor field in the upper troposphere of the tropical region has been poorly observed. Satellites provide a better way to achieve greater spatial and temporal coverage. The Microwave Limb Sounder (MLS) on the Upper Atmosphere Research Satellite (UARS) is sensitive to water vapor in the upper troposphere. With a 3 km field of view in the vertical, it has greater vertical resolution than that of infrared instruments such as Meteosat [*Schmetz and Turpienen*, 1988], the U.S. Geostationary Operational Environmental Satellite (GOES) [*Soden and Bretherton*, 1993], and the TIROS Operational Vertical Sounder [*Salathé and Chesters*, 1995], which are sensitive to water vapor in a broad layer of the upper troposphere ~ 300hPa thick. The MLS measurement of upper tropospheric humidity (UTH) is relatively insensitive to cirrus clouds, giving it additional advantages over infrared techniques. The temporal resolution of MLS is better than that of solar occultation instruments such as the Stratospheric Aerosol and Gas Experiment 2 (SAGE II) from which measurements are limited to ~ 30 per day. For several years, MLS has provided daily coverage of the tropical region since its launch in September 1991.

The MLS water vapor data reveal synoptic-scale features and detrainment streams extending from tropical convective regions [*Read et al.*, 1995], as well as the gross annual variations of the zonal mean [*Elson et al.*, 1996]. In the tropics, *Newell et al.* [1996] have shown that the observed distribution of water vapor is consistent with the Walker circulation, and *Newell et al.* [1997] have shown that upper tropospheric

[1]Also at Joint Institute for the Study of the Atmosphere and Ocean, University of Washington, Seattle

Paper number 98JD02702.
0148-0227/98/98JD-02702$09.00

water vapor is closely related to sea surface temperature variations in the eastern Pacific. In this paper, the MLS measurement will be used to examine the temporal and zonal variability of upper tropospheric water vapor in the tropical region and to account for the observed variability by relating it to known processes.

2. Data

UARS is in an almost circular orbit at an altitude of 585 km and an inclination of 57° to the equator [*Reber*, 1993]. It makes ~ 14 orbits each day with adjacent orbits being separated by ~ 2670 km at the equator, thereby allowing a zonal mean and six wavenumbers to be resolved. MLS makes a limb scan perpendicular to the orbit path at tangent heights from 90 km to the surface. Each scan takes 65.5 s and consists of a profile of measurements which are usually retrieved onto 15 pressure levels. MLS provides a 3 km field of view in the vertical. Latitudinal coverage changes from between 80°N and 34°S to 34°N and 80°S because the satellite performs a yaw maneuver about every 36 days, but the tropical region is observed daily, enabling a nearly continuous time series to be constructed. The MLS instrument is described in more detail by *Barath et al.* [1993], and the measurement technique is described by *Waters* [1993].

The 205 GHz channel on MLS is principally used to measure chlorine monoxide but it is sensitive to water vapor in the upper troposphere when concentrations are in the range of 100 to 300 ppmv [*Read et al.*, 1995]. The best sensitivity occurs when the water vapor concentration is about 150 ppmv; of the standard UARS pressure levels, it is at 215 hPa (~ 12 km at low latitudes and ~ 7 km at high latitudes) that this concentration most often occurs. We therefore focus our study on the 215 hPa level.

Retrievals in the upper troposphere may be affected by thick cirrus clouds. In the tropical region between 6 and 12 km, the retrievals are not significantly affected, but at latitudes poleward 40°, a significant fraction of the measured radiances may come from scattering by cirrus clouds [*Bond*, 1996]. Ice crystals in cirrus clouds at a concentration of 0.1 g m^{-3} over a horizontal distance of 120 km could contribute to 20% of the absorption coefficient at 215 hPa but will usually be less, and at concentrations less than 0.01 g m^{-3} the effect is negligible [*Read et al.*, 1995].

The data are derived from the initial MLS UTH retrieval as described by *Read et al.* [1995]. A new and improved MLS UTH retrieval has recently been developed, which among other features has a formal error estimation calculation and has been compared with Vaisala thin-film capacitive radiosonde measurements. Comparisons with the newer product show the current analyzed product at 215 hPa, which is used in this paper, to be biased high by 50-60 ppmv (everywhere) and to have a precision of 5 ppmv.

Footprints were interpolated onto points spaced every 5° in longitude around latitude circles at 20°N, 10°N, the equator, 10°S, and 20°S. Footprints that fell within a given "search radius" of these points were given a distance weighting based upon the regression retrieval and space-time interpolation method used by *Jackson et al.* [1990]. A search radius of 2150 km was used with a scaling distance of 1000 km so that footprints 1000 km away from the given grid point have a relative weighting of 1/e whereas any that fall directly on the grid point have a relative weighting of 1. Zonal and meridional winds and vertical velocity were taken from the European Centre for Medium Range Weather Forecast's (ECMWF) initialized reanalysis data, which are gridded with a 2.5° by 2.5° resolution on the standard pressure levels.

3. Results

Whereas *Elson et al.* [1996] focused on the variability of zonal mean water vapor in latitude-time plots, we focus on the variability of zonal cross sections in longitude-time plots. First, we discuss the variability at low frequencies that is associated with the annual cycle. Next, we discuss intraseasonal variability and the connection between water vapor and meteorological fields.

To create longitude-time plots, the MLS footprints were first interpolated onto grid points as described in section 2. Data gaps were then filled in time using a Kalman filter. Most data gaps are of only 1 day, but a gap of ~ 2 weeks occurred in June 1992. The resulting longitude-time plots for the time period from December 1, 1991, to May 3, 1993, are shown in Plate 1, with the five regions showing the five latitude bins between 20°N and 20°S. Gaps longer than 3 days have been masked.

3.1. The Annual Cycle

In Plate 1 and particularly in Plates 1a, 1b, 1d, and 1e, an annual cycle in mixing ratio is apparent. Mixing ratios are high in local summer over continents when convection is strong and low in local winter when convection is weaker.

The northern hemisphere latitudes, 20°N and 10°N, are shown in Plates 1a and 1b respectively. The highest water vapor mixing ratios occur between 50°E and 120°E over the Indian Ocean and SE Asia from May to September when convection is strong. The annual cycle was isolated by least squares fitting to a sine wave. It is most pronounced in the region influenced by the Indian monsoon. At 20°N and 90°E, over the Bay of Bengal, it accounts for 80% of the variance in water vapor. Local maxima in the annual cycle occur just west of Panama as *Newell et al.* [1997] have noted, and minima over the cold eastern Pacific and Atlantic Oceans.

At the equator (Plate 1c), the range of mixing ratios is smaller than at the other tropical latitudes. The smaller range is probably because the Intertropical Convergence Zone (ITCZ) is rarely situated at the equator itself [*Philander et al.*, 1996]. The maximum mixing ratios are located over the Indian Ocean and Indonesia. The minimum mixing ratios occur over the eastern Pacific and are subject to an east-west migration on annual timescales, resulting in lower values extending further west in June-August and further east from November to January. As noted by *Newell et al.* [1997], the amplitude of the annual cycle, like the range, is smallest at the equator, and probably for the same reason. At the equa-

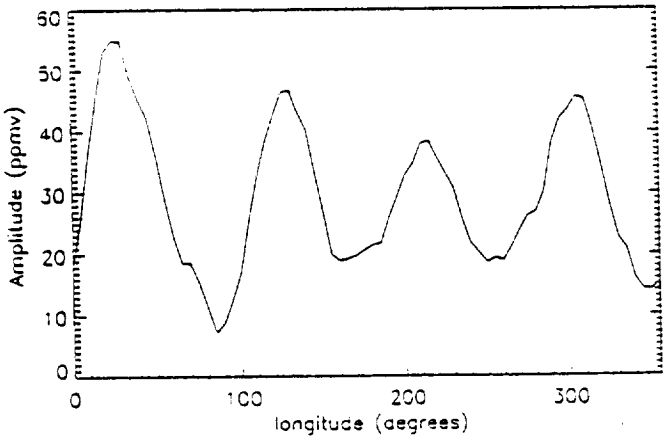

Figure 1. Amplitude of the annual cycle in water vapor mixing ratio (ppmv) at 10°S and 215 hPa.

tor, it exhibits its maximum amplitude at 90°W, off the coast of South America, where it accounts for 53% of the variance. *Newell et al.* [1997] showed that water vapor variations in the region 80°-90°W and 0°-10°S are related to variations in sea surface temperature (SST) caused by El Niño and also to anomalous changes in SST; the latter account for ~56% of the water vapor variance.

In the southern hemisphere, Plates 1d and 1e, mixing ratios are greater over Indonesia and South America during summer and lower over the eastern Pacific in winter. In the longitude-time section (Plate 1d), strong annual cycles can be seen over the African continent and South America. Figure 1 shows the variation of the amplitude of the annual cycle with longitude at 10°S and reveals further local maxima over Indonesia and the mid-Pacific. The influence of the cold eastern Pacific in suppressing convection and leading to a drier upper troposphere and of the warm western Pacific leading to a moister upper troposphere is evident in Plate 1d. This constitutes the Walker circulation with rising air in the west and subsiding air in the east. The influence of the Walker circulation on upper tropospheric water vapor from MLS has been noted by *Newell et al.* [1996] in two short periods of data from September 17 to October 22, 1991, and February 7 to March 14, 1994. Here, the presence of the Walker circulation can be seen to be a more persistent feature. Mixing ratios over the western Pacific show east-west migration similar to that at the equator, with low humidity found further west during winter, when the ocean is colder. Eastward moving features during the summer months originate over the warm Indian Ocean and are quickly terminated once they reach the eastern Pacific. These have a higher frequency than the annual cycle and are investigated by analyzing the time series with a focus on intraseasonal timescales.

3.2. Intraseasonal Variability

One of the main modes of variability in the tropics is the Madden-Julian oscillation (MJO) [*Madden and Julian*, 1971]. The MJO comprises large-scale circulation anomalies associated with convective anomalies which propagate eastward at 3-6 m s^{-1}. The dynamical signal of MJO, in zonal wind and surface pressure, has a period of 30-60 days and can be detected across the tropics. The convective signal has a broader range of 30-95 days [e.g., *Kiladis and Weickmann*, 1992; *Salby and Hendon*, 1994] and is strongest in the Indian Ocean and western Pacific.

Eastward moving moist features are apparent in the water vapor fields (Plate 1) and are most prominent at 10°S in southern summer. The moist anomalies at 10°S cover longitudes from 90°E to 245°E (115°W). One such feature begins at 105°E and travels to 190°E in ~22 days, thus moving with a speed of ~5 m s^{-1}. At the equator during southern summer, there are eastward moving features similar to those at 10°S, but they are less intense; during southern winter, eastward propagation is less common. Similar propagation of moist anomalies occurs at 10°N in northern summer with a more limited longitudinal extent, being confined mostly to the Indian Ocean. There is also evidence for the eastward movement of dry features between 130° and 280°E in northern hemisphere winter at 10° and 20°N (Plates 1a and 1b). In this section, the eastward moving moist features and their relationship to the MJO will be discussed.

The periodicity of the disturbances at a fixed longitude may be investigated from the power spectrum or from the lag correlogram. For a data set like that in Plate 1, the lag correlogram has some advantages, as it is insensitive to change of phase in the waves from one winter to the next and to whether the wave period is a proper harmonic of the length of the data set. Furthermore, it can reveal some information even when the waves exist for little more than one period.

Figure 2 shows the lag correlogram for 160°E and 10°S based on the 520 days of data used for Plate 1. Here, 160°E is illustrated as the longitude which exhibits the greatest intraseasonal variability. The annual cycle and low-frequency variability was removed from each longitude using a 150 day Butterworth filter. Also shown is the red noise background spectrum computed from lag-one autocorrelation [*Gilman et al.*, 1963] and the 95% confidence limits. The data have anticorrelation less than −0.2, at lags of 20–35 days, well below the red spectrum and significant at the 95% level. This is suggestive of waves of period 40–70 days, an interpretation supported by the existence of positive correlations at lags of 40–70 days. Inspection of Plate 1 suggests that these correlations arise from features which are only apparent in the southern summer months. Only slightly over one cycle is apparent in each year and so very high correlations cannot be expected. Moreover the magnitude of the correlation at the wave period will be necessarily less than that at the half period. By cross-correlating the time series at each longitude with the time series at 160°E using different lags, the estimated propagation speed was confirmed to be 4-5 m s^{-1}.

Figure 3 shows how the power at each frequency varies with longitude for 10°S. The strongest signal corresponds to a frequency of 0.014 $days^{-1}$ or a period of 70 days and falls within the frequency range associated with the convective signal of the MJO. The power spectrum was tested for significance at 95% by computing the signal to red noise ratio at each longitude and comparing it with the chi-squared distribution following the method of *Gilman et al.* [1963].

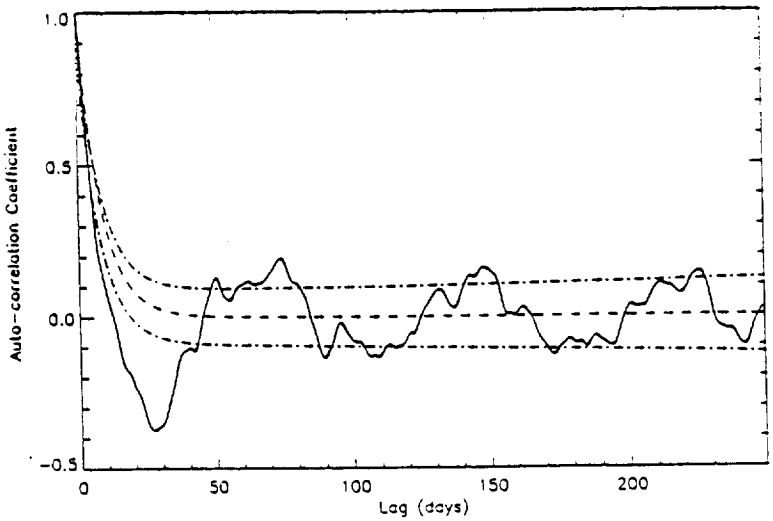

Figure 2. Auto-correlation of the time series of 215 hPa water vapor mixing ratios at 160°E and 10°S (solid line), red noise (dashed line), and 95% confidence limits (dash-dotted lines).

At 70 days and 160°E, values greater than 112ppm^2 are significant. The signal is confined in longitude from 140° to 180°E. This area, over the western Pacific, has been shown to exhibit strong intraseasonal variability in outgoing longwave radiation (OLR) which is often used to infer deep convection. *Salby and Hendon* [1994] examined 11 years of OLR data from the advanced very high resolution radiometer (AVHRR) and found that intraseasonal behavior was coincident with centers of climatological convection and warm sea surface temperature, with maxima over the Indian Ocean and western Pacific and secondary maxima over the eastern Pacific, Africa, and South America. They noted that most of the intraseasonal variance occurred over the Indian Ocean. This contrasts with the signal in water vapor which is dominant over the western Pacific. The absence of a signal in the water vapor field over the Indian Ocean may indicate that convective moistening is not reaching the 215 hPa level.

In order to focus on the intraseasonal frequency range characteristic both of the MJO and of the eastward moving disturbances seen in Plate 1, we filtered the water vapor data with a 30–85 day Butterworth band-pass filter similar to that used previously in studies of OLR [e.g., *Salby and Hendon*, 1994; *Zhang and Hendon*, 1997]. When applied to 520 days of data at 10°S and 160°E, the 30–85 day filter band accounted for 35% of the total power compared with 19% for the annual cycle. Mixing ratios in this band vary by

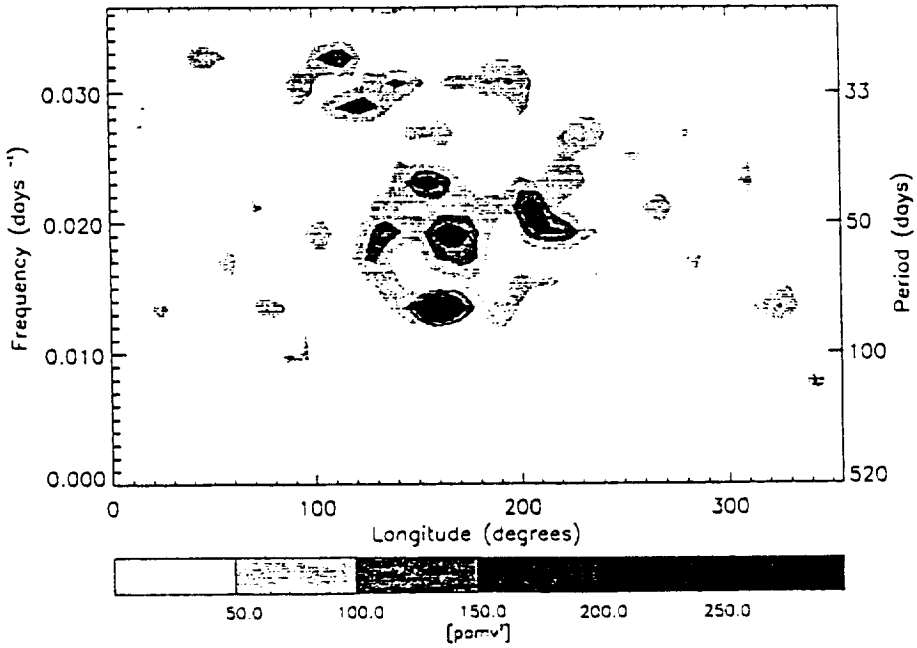

Figure 3. Power spectrum, as a function of longitude and frequency, of deseasonalized water vapor at 215 hPa. Contour intervals are 50 ppmv^2.

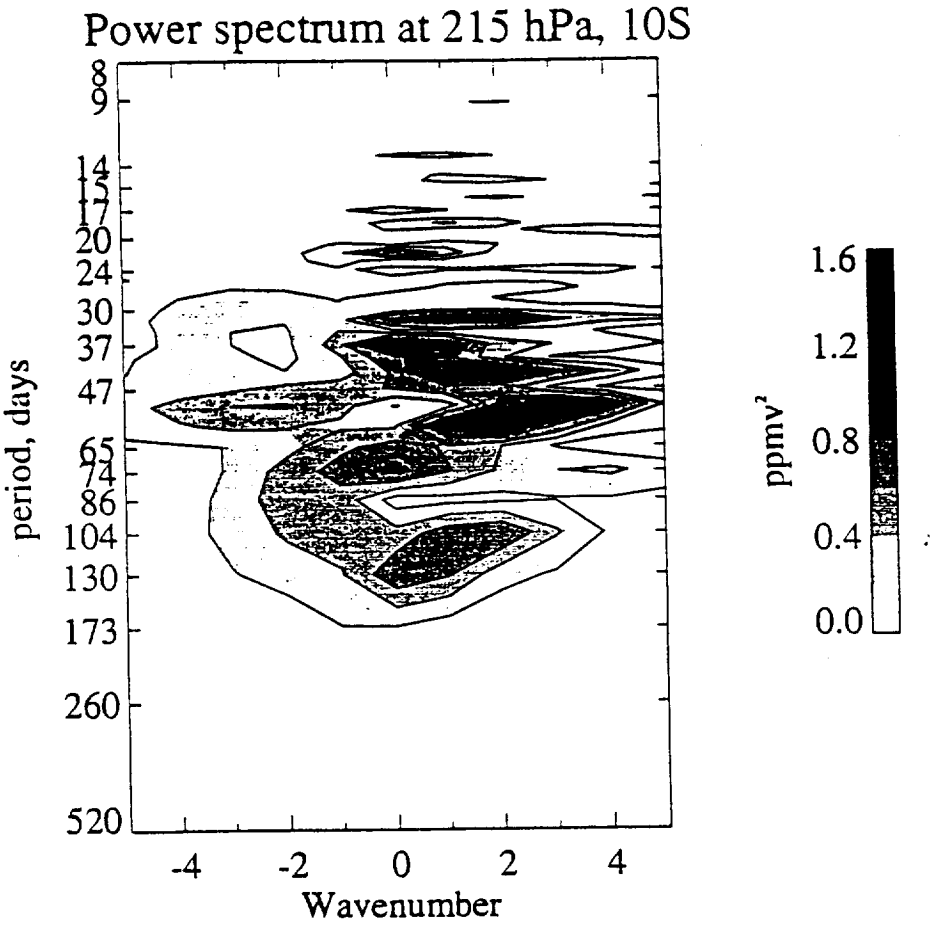

Figure 4. Power spectrum, as a function of wavenumber and frequency, of de-seasonalized water vapor at 215 hPa and 10°S.

± 60 ppmv. At the equator, intraseasonal activity occurring in the 30–85 day band accounts for 35% less power than at 10°S.

At 10°S the water vapor anomalies, consistent with the OLR signal [*Salby and Hendon*, 1994], possess a strong seasonality that is apparent in the longitude-time section (Plate 1d). The eastward propagating anomalies are strong when the ITCZ is near the latitude in question (local summer) but virtually absent when the ITCZ is not (local winter). When the eastward propagating anomalies are strong (December 1991 to March 1992), intraseasonal variability accounts for as much as 63% of the total variance, but, when they are weak (August–November 1992), intraseasonal variability only accounts for 7% of the total variance.

Further insights about the nature of the intraseasonal variability come from a wavenumber-frequency spectral analysis. The low-frequency variability was removed from 520 days of data using the 150 day band-pass filter as before, and the filtered data have been regressed against zonal and temporal harmonics of the form $\cos(kx - \omega t)$ to identify the power at discrete wavenumbers k and frequencies ω. Figure 4 shows the results of this analysis. There is very little power at the lowest frequencies, owing to the filtering; most power is concentrated in positive (eastward) wavenumbers 1–3 with periods from 30 to 60 days. Modes at $k = 0$ have a small share of the power, mostly at 37 and 74 days and represent a zonally symmetric mode. Because the zonal structure and frequency of the water vapor anomalies are similar to those usually identified with the convective component of the MJO (e.g., OLR), we tentatively identify these anomalies with the MJO.

To separate the modes of variability suggested by Figure 4, we calculate extended empirical orthogonal functions (EEOFs) [*Weare and Nasstrom*, 1982, *Wang et al.*, 1995]. Their more common cousins, empirical orthogonal functions (EOFs) , identify coherent variations by finding eigenvectors of the (symmetric) covariance matrix and ranking these eigenvectors in descending order of variance explained. For the longitude-time array of water vapor at 10°S, the covariance matrix for ordinary EOFs would be formed by summing (in time) the covariance $q_i(t)q_j(t)$ of water vapor $q_i(t)$ at every combination of longitudinal grid points. The EOFs would be one-dimensional functions of longitude and would yield a clearer picture of zonally coherent variations. Extended EOFs are found by calculating covariance of water vapor at each grid point not just with water vapor at other grid points but also at different lag times l, i.e., $q_{i,l}$, where the lag varies in this case between −60 and +60 days at 5

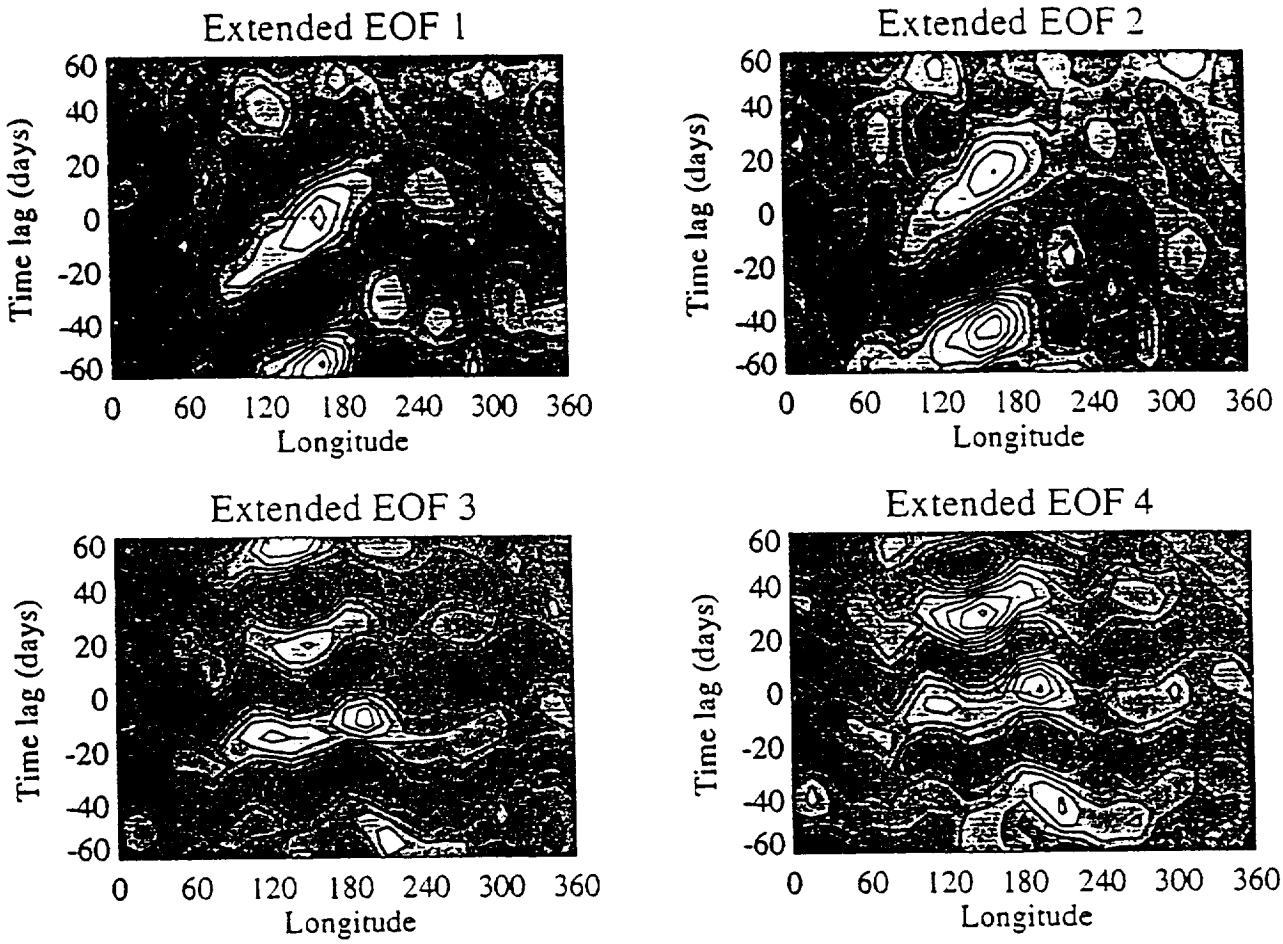

Figure 5. Spatiotemporal structure of the first four extended EOFs of deseasonalized water vapor at 215 hPa and 10°S.

day intervals. EEOF analysis yields a clearer picture of zonally and temporally coherent variations.

The first four EEOFs are shown in Figure 5. EEOFs (and EOFs) sometimes occur in conjugate pairs, identified by the closeness of their eigenvalues, by their associated time series which are in quadrature and by their spatiotemporal structure which is also in quadrature. The significance of conjugate pairs is that they describe a quasi-periodic oscillation of some sort. The first pair of EEOFs in figure 5 have the characteristics of a conjugate pair, as do the next pair of EEOFs. The next four EEOFs (not shown) form two more conjugate pairs, but their interpretation is more difficult. The oscillation indicated by the first pair of EEOFs shows eastward propagation between about 75°E and 200°E (as in Plate 1d); and the time lag between maxima is 55 days. The phase speed of anomalies is 3–4 m s^{-1}. High variance is confined to the Indian Ocean and western Pacific (75°E–200°E). By contrast, the oscillation indicated by the second pair of EEOFs is somewhat more broadly distributed in longitude, shows no identifiable eastward or westward propagation, and the time lag between maxima is 35 days.

The time series of the coefficients of the EEOFs, or principal components (PC) (Figure 6), reveal both the intraseasonal cycles and the seasonal envelope, with smaller variance during southern winter as noted above. Spectral analysis confirms what a visual inspection suggests: The dominant spectral peak for PC1 and PC2 is at 50 days, while the dominant spectral peak for PC3 and PC4 is at 36 days. (Note that the temporal resolution of the PCs is 1 day, while the temporal resolution of the EEOFs is 5 days.) Based on the spatiotemporal structure revealed in Figure 5 and the characteristics of the time series just discussed, it seems reasonable to associate the first pair of EEOFs with the band of variance at 50–60 days and wavenumbers 1–4 in Figure 4 and to associate the second pair of EEOFs with the $k = 0$ mode at 37 days in Figure 4.

Figure 7 is a reconstruction of the longitude-time section in plate 1d using combinations of the PCs. The original longitude-time section is shown for comparison alongside reconstructions using PC 1 and 2 only, PC 3 and 4 only, and PC 1, 2, 3 and 4 combined. Figure 7 highlights the eastward moving anomalies in the original data and demonstrates how the eastward propagation is captured by the EEOFs. Most of the eastward propagation west of the dateline is picked out by EEOF 1 and 2. EEOF 3 and 4 account for less of the variance, but their inclusion increases the eastward extent of the anomalies.

3.2.1. Relationship with other meteorological fields.

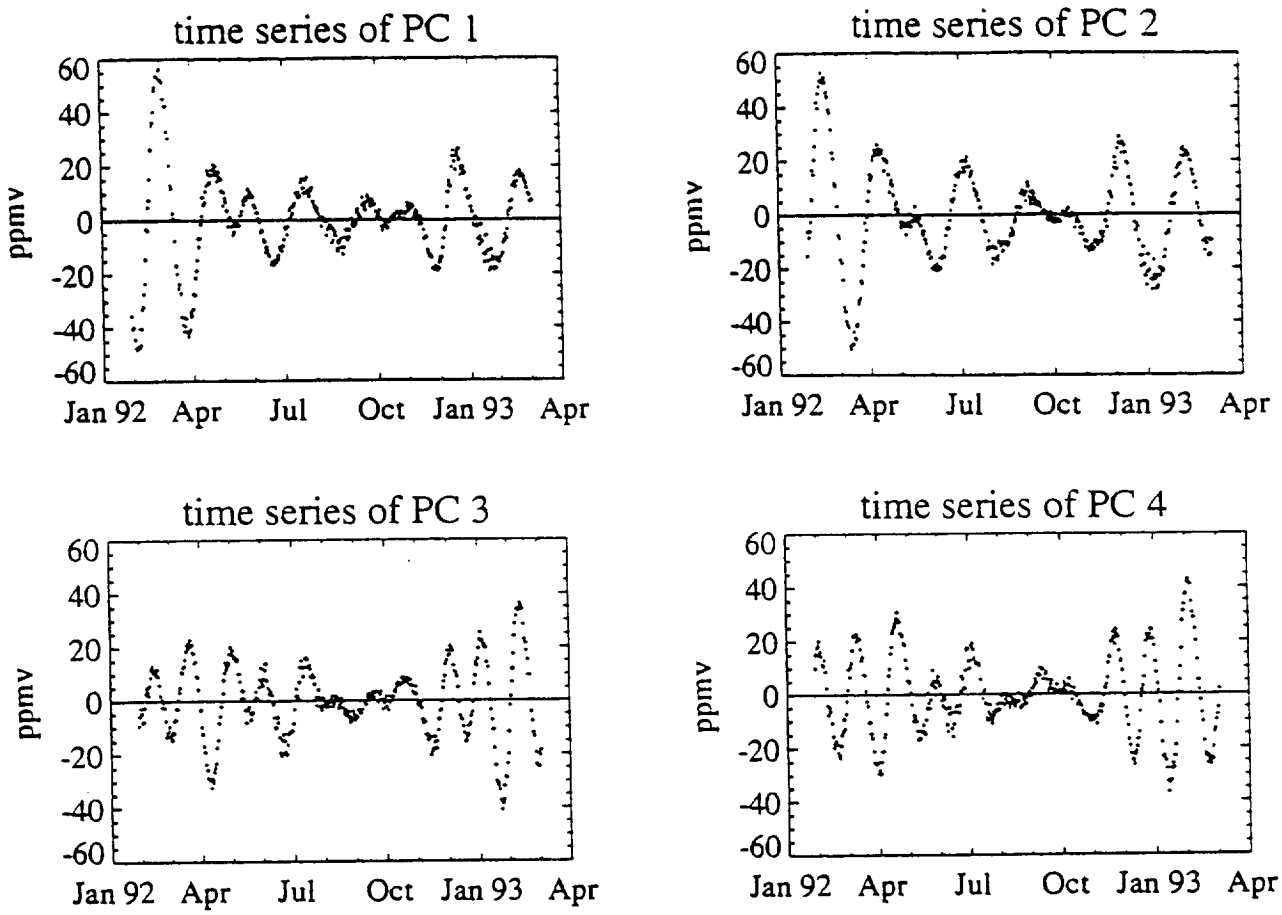

Figure 6. Time series of the coefficients of the EEOFs (principal components (PC)) in the previous figure.

In order to strengthen the proposed identification between the water vapor anomalies and MJO, the water vapor field is compared with vertical velocity and zonal winds obtained from ECMWF reanalysis. We examine the lifecycle of water vapor during the eastward moving event in December 1991 to February 1992 identified in section 3.2, and compare this to midtropospheric vertical velocity at 500 hPa. Both quantities are plotted as 5 day averages in Figure 8 where water vapor mixing ratios >170 ppmv are shaded in grey and upward vertical velocity less than -0.05 Pa s^{-1} is colored black. The dates indicate the middle of each pentad.

From December 17-22, mixing ratios >170 ppmv are spread out in a band along the equator. Several small pockets of vertical velocity are strung out along the equator from Africa as far as 135°W and there is indication of the South Pacific Convergence Zone (SPCZ). On the December 27, the distribution of high water vapor begins to shift from Africa and the Indian Ocean toward Indonesia. Similarly, the distribution of pockets of vertical velocity has shifted from Africa and the Indian Ocean toward Indonesia. Both the SPCZ and the ITCZ are well pronounced in the vertical velocity field.

On the January 1, there is a large vertical velocity pocket over the west Pacific and a corresponding area of high mixing ratio is beginning to develop. By January 6, the moist area has moved eastward from Indonesia to become centered over the western Pacific and vertical velocity is still strong at this time. On the January 11, the pocket of vertical velocity begins to break up, but water vapor mixing ratios remain high and continue to migrate eastward and to intensify along the SPCZ. The SPCZ remains a strong characteristic in both the vertical velocity and water vapor fields until February 5, but lingers as a feature in water vapor for a further 5 days. On the February 10, the small pockets of vertical velocity have returned to Africa and the Indian Ocean and mixing ratios have begun to increase here also. Finally, water vapor disperses from the SPCZ.

This correspondence between water vapor and vertical velocity illustrates a strong relationship between high mixing ratios and convection and indicates that the convective system as a whole moves eastward rather than the water vapor being advected along at the 215 hPa level. The patterns of water vapor mixing ratio are similar to those in OLR during the MJO in March–April 1988 described by *Matthews et al.* [1996]. Both begin as a low intensity band along, and mostly south of, the equator which becomes organized over Indonesia and the west Pacific and is followed by development in a southeast direction along the SPCZ. Again, the SPCZ remains prominent in the water vapor field for longer than in OLR. *Knutson and Weickmann* [1987] noted the development of OLR from the Indian Ocean to the SPCZ. *Rui*

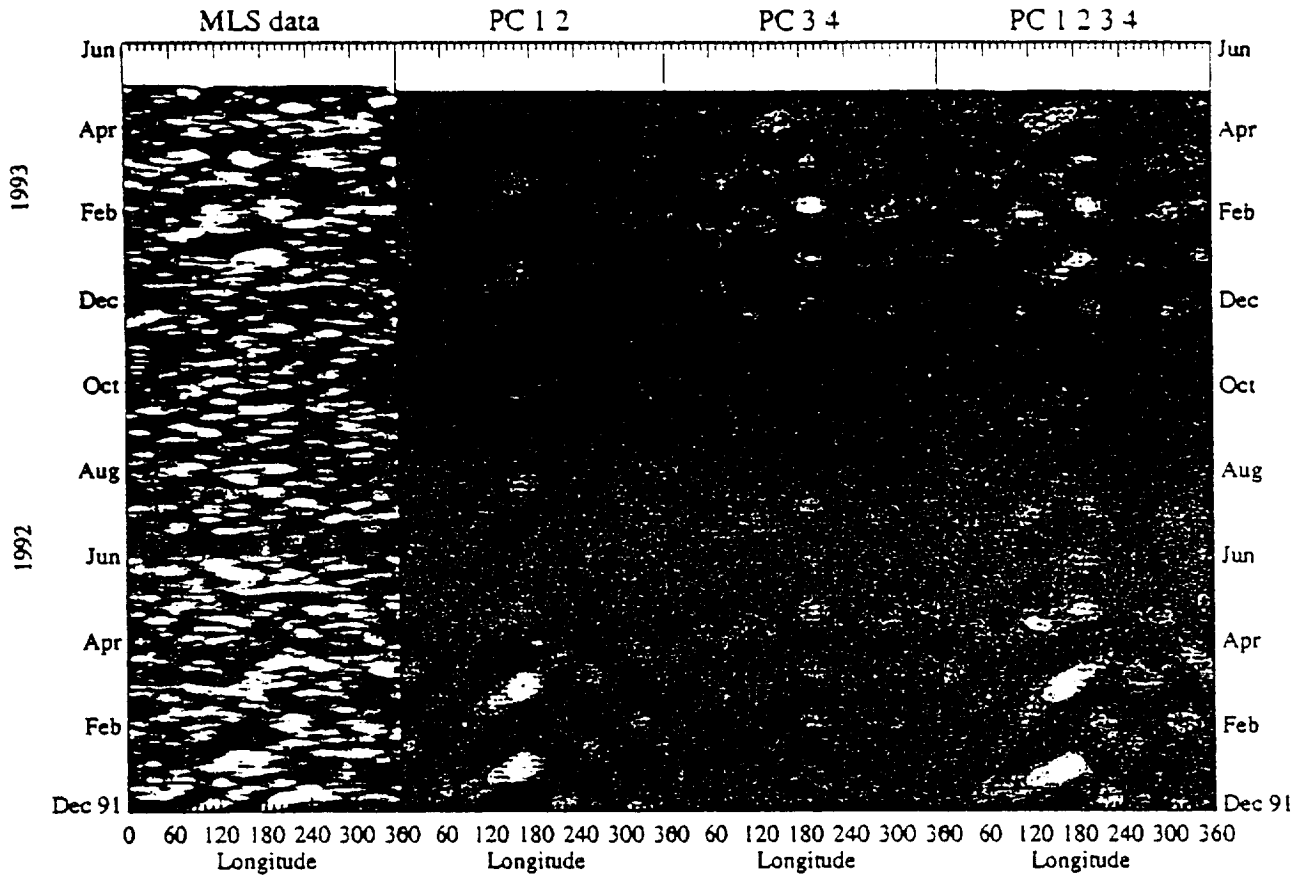

Figure 7. Reconstruction of the longitude-time section using combinations of the principal components (PC).

and Wang [1990] found that development along the SPCZ occurred in strong MJO events, and *Matthews et al.* [1996] found that enhancement or excitation of convection along the SPCZ is observed in virtually all MJOs from 1979 to 1988.

The high water vapor mixing ratios also appear to be related to westerly wind bursts in the lower troposphere. *Wang* [1988] showed that although the mean surface winds in the tropics are easterly, they are often westerly in the region where convective anomalies associated with the MJO originate. *Zhang* [1996] found that deep convection tended to occur in connection with 850 hPa westerly wind perturbations, and *Hendon and Glick* [1997] showed that westerly wind anomalies were related to enhanced evaporation. A time series of zonal winds at 850 hPa and 10°S is shown in Figure 9. Regions of westerly wind are evident during southern summer in both 1992 and 1993 and are well correlated with the eastward moving moist features in the longitude-time plot of water vapor (Plate 1d). The longitudinal extent of the westerly winds in 1992 (from 40°–200°E) corresponds well with the more evident eastward propagation in the water vapor field of this year.

In contrast to the zonal winds at 10°S, westerly wind bursts at the equator (not shown) are weaker and have a limited longitudinal extent. Similarly, *Zhang and Hendon* [1997] who also used 850 hPa zonal winds from the ECMWF analysis showed that the maximum intraseasonal variance in zonal wind was off the equator and concentrated in the western Pacific. This is an important reason for the mixing ratios being higher at 10°S than at the equator and further indication that the high mixing ratios are a result of enhanced evaporation and convection. The fact that the largest variances do not lie on the equator appears to be in conflict with those theories which attribute the MJO to moist Kelvin waves, as remarked by *Zhang and Hendon* [1997].

3.2.2. Interannual variability. There have been suggestions that the MJO varies in strength from year to year and that this may be related to the El Niño-Southern Oscillation phenomenon [e.g., *Lau and Chan*, 1986]. Accordingly, we have investigated the behavior of the MLS upper tropospheric humidity data for other years. There are some practical difficulties with this as data gaps prevent a detailed investigation of the southern summer months. The data gaps have increased in length as the spacecraft and instrument have aged and make later years more difficult to study. Longitude-time sections for southern summer periods are shown for 10°S in Plate 2 for all the available MLS data. Data have been treated in the same way as for Plate 1. Because there were not sufficient data for the southern summer of 1994–1995, that period is omitted.

Signs of eastward propagation are most apparent in 1991–1992 when mixing ratios between 170 and 195 ppmv reach

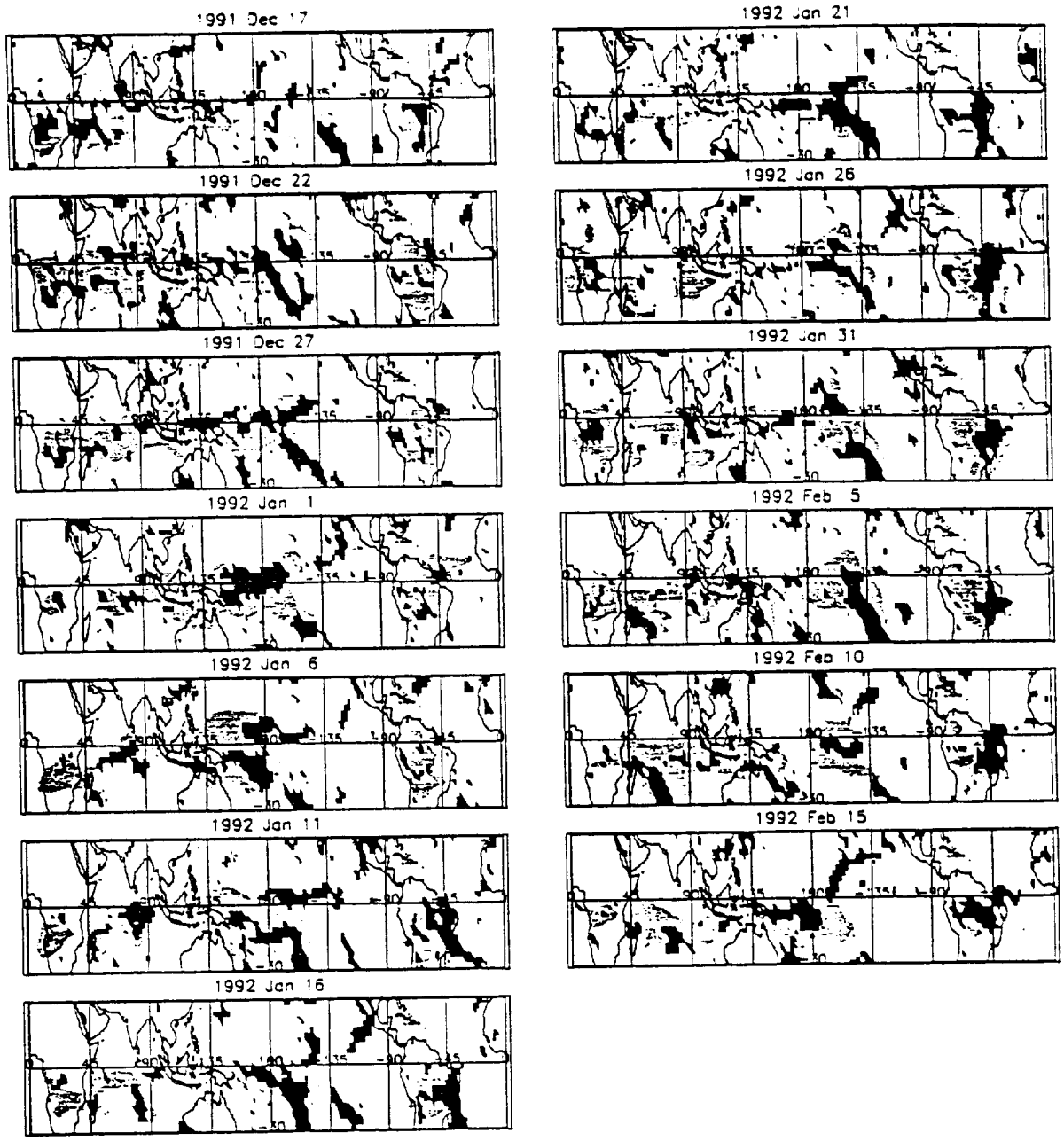

Figure 8. The 5 day averaged water vapor mixing ratios, at 215hPa and >170 ppmv (grey) and ECMWF vertical velocity at 500hPa and <-0.05 Pa s^{-1} (black). Dates indicate the middle of the pentad.

as far as 240°E (120°W). This is further east than in any other year, and it should be noted that this was an El Niño year [*Trenberth*, 1997]. In all other years, mixing ratios >170 ppmv never extend further east than 210°E (150°W). *Knutson and Weickmann* [1987] noticed similar behavior in OLR and proposed that low sea surface temperatures or descending motion associated with the Walker circulation suppress further eastward development. Hence, the greater extent of the anomalies in 1991–1992 is probably a result of the eastward shift of convection that is a fundamental component of ENSO.

In 1992–1993 (Plate 2b), the 30-85 day filter band accounts for 52% of the variance compared with 63% in 1991–1992, and in 1992–1993 eastward movement is less evident. In the summer of 1993–1994 (Plate 2c), total variance is the same as in 1991–1992, but that associated with eastward propagation is less. In 1995–1996, a La Niña year [*Trenberth*, 1997], the lowest mixing ratios of any of the years, <70 ppmv, are reached over the eastern Pacific, and the mean and maximum mixing ratios are also lower than in other years, with the maximum mixing ratios never exceeding 245 ppmv. Although the data in 1996–1997 are sparse, mixing ratios can be seen to be as high as those in 1991–1992, and there may even be signs of eastward propagation in late February and early March. High mixing ratios do not have the same eastward extent as in 1991–1992. *Salby and*

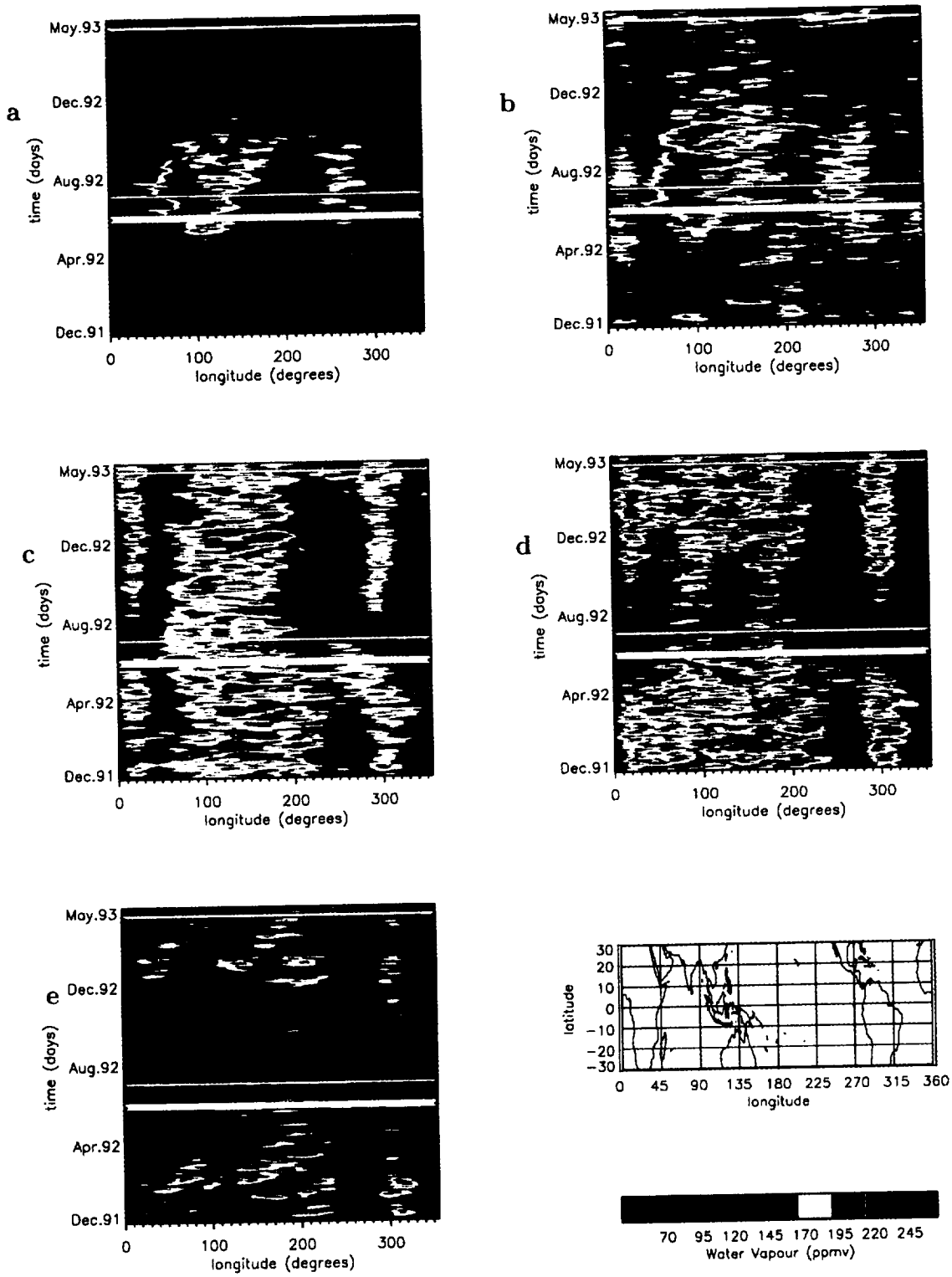

Plate 1. Longitude-time sections of water vapor mixing ratios (ppmv) at 215 hPa and latitudes of (a) 20°N, (b) 10°N, (c) 0°, (d) 10°S, and (e) 20°S. Data have been Kalman filtered and a mask applied to gaps of more than 3 days.

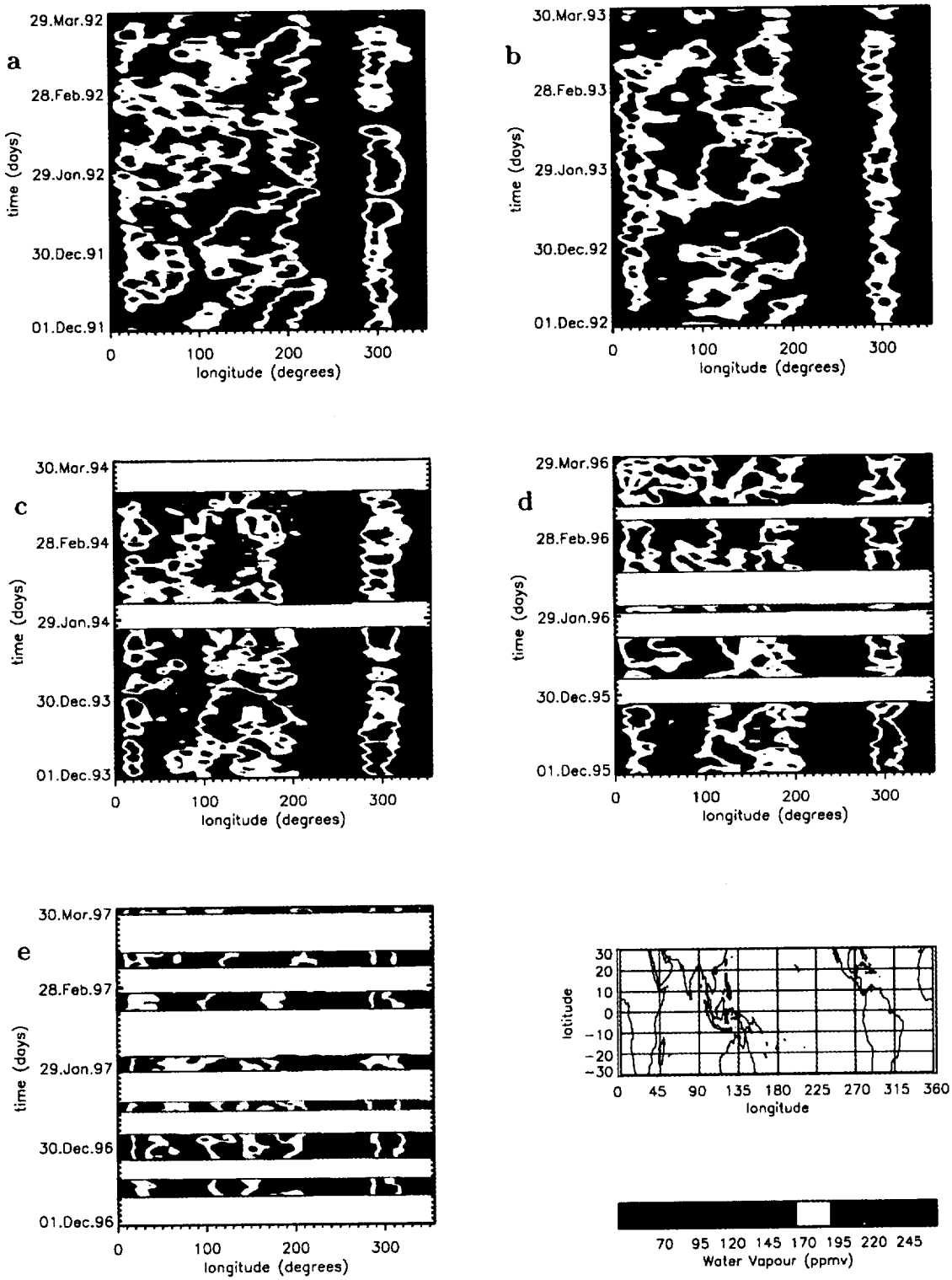

Plate 2. Longitude-time sections of water vapor mixing ratios (ppmv) at 215 hPa and 10°S for 120 days of southern summer from December–March in (a) 1991–1992, (b) 1992–1993, (c) 1993–1994, (d) 1995–1996, (e) 1996–1997. Data have been Kalman filtered, and a mask has been applied to gaps of more than 3 days.

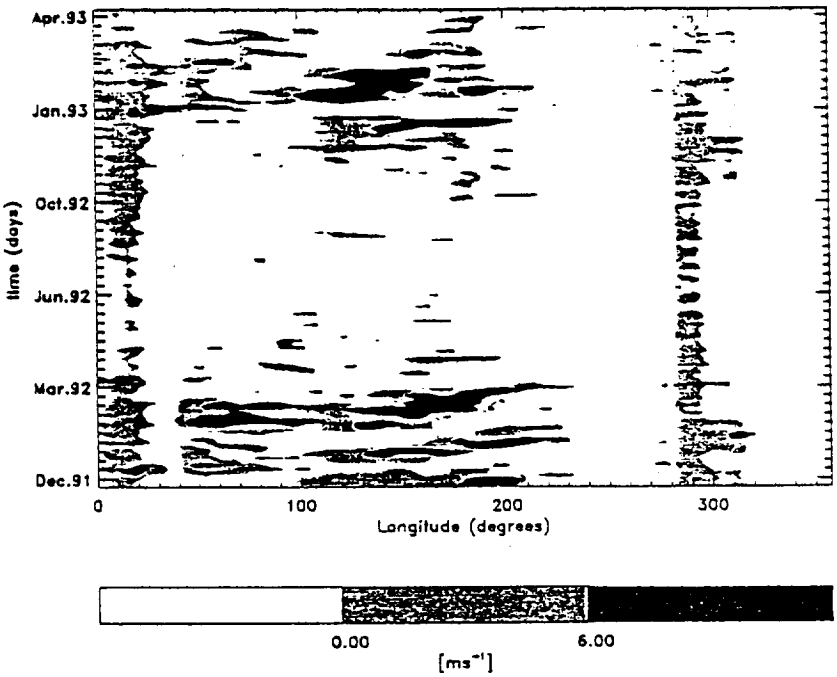

Figure 9. Longitude-time section of ECMWF zonal winds (m s^{-1}) at 10°S and 850 hPa.

Hendon [1994] found that the convective signal was absent during the strong ENSO cycle of 1982–1983 The relationship between the MJO and ENSO warrants further investigation.

4. Conclusions

We have shown that water vapor in the tropical upper troposphere varies on both annual and intraseasonal timescales. The annual cycle can be clearly seen in longitude-time sections of water vapor, but during southern hemisphere's summer, variability at intraseasonal timescales exceeds variability at the annual timescale. The annual cycle is most pronounced over the landmasses of South America and Africa, in agreement with the study by *Newell et al.* [1997]. Although the annual cycle is generally smaller over the oceans, local maxima occur in some oceanic locations, notably in regions influenced by the Asian monsoon and over Indonesia and the central Pacific.

Longitude-time sections revealed eastward moving moist anomalies that were most prominent at 10°S from December 1991 to March 1992. It is significant that this period coincides with an El Niño. The features originate in the Indian Ocean and propagate at speeds of 3-4 m s^{-1} until they reach the eastern Pacific. The EEOF analysis and wave-frequency analysis reveal eastward propagating modes at 30-60 days. These spectral characteristics in space and time (Figures. 4, 5, and 6) together with the longitudinal lifecycle of the moist anomalies observed in longitude-time sections, resemble those of the MJO. We therefore identify the anomalies with the convective component of the MJO. The longitudinal extent of the intraseasonal signal was limited to the western Pacific where it dominated over the annual cycle during the time period from December 1991 to May 1993.

In addition to the eastward propagating modes interpreted as the MJO, zonally symmetric modes with periods of ~37 and 74 days have also been identified from the EEOF analysis, combined with spectral analysis of the principal components (Figures 5 and 6) and from power-spectrum analysis and wavenumber-frequency spectral analysis (Figures 3 and 4). These may be related to standing components of tropical convection which have been observed in OLR and 150 hPa divergence [e.g., *Hsu et al.*, 1990; *Zhu and Wang*, 1993; *Zhang and Hendon*, 1997].

A sequence of pentad maps showed the movement of moist anomalies from Africa across the Indian Ocean, intensification over Indonesia and the West Pacific and development along the SPCZ. The vertical velocity field has similar characteristics, lending support to our assertion that the moist anomalies at 215 hPa are associated with slowly translating convection. The origin of the moist anomalies would appear to be enhanced surface evaporation during westerly wind bursts, which were seen to be strongly correlated with water vapor and are known to play an important part in generating and maintaining the MJO.

Acknowledgments. The water vapor data was produced at the Jet Propulsion Laboratory, California Institute of Technology, under contract with NASA and funded through its UARS Project. The work was supported by NERC in the UK and by NASA contracts NAS1-96071 and NAS5-32862. The authors thank H.C. Pumphrey for useful discussions.

References

Barath, F., et al., The Upper Atmosphere Research Satellite Microwave Limb Sounder Instrument, *J. Geophys. Res.*, *98*, 10751-10762, 1993.

Bond, S.T., The potential effect of cirrus on Microwave Limb Sounder retrievals, Ph.D. thesis, pp.161-173, Univ. of Edinburgh, Scotland, United Kingdom, 1996.

Chou, M.-D., Coolness in the tropical Pacific during an El Niño episode, *J. of Clim.*, *7*, 1684-1692, 1994.

Elliot, W.P. and D.J. Gaffen, On the utility of radiosonde humidity archives for climate studies, *Bull. Am. Meteorol. Soc.*, *72*, 1507-1520, 1991.

Elson, L.S., W.G. Read, J.W. Waters, P.W. Mote, J.S. Kinnersley, and R.S. Harwood, Space-time variations in water vapor as observed by the UARS Microwave Limb Sounder, *J. Geophys. Res.*, *101*, 9001–9015, 1996.

Gilman, D.L., F.J. Fuglister and J.M. Mitchell Jr., On the power spectrum of red noise, *J. Atmos. Sci.*, *20*, 182-184, 1963.

Hendon, H.H. and J. Glick, Intraseasonal air-sea interaction in the tropical Indian and Pacific oceans, *J. of Clim.*, *10*, 647-661, 1997.

Houghton, J.T., G.J. Jenkins, and J.J. Ephraumus, *Climate Change: The IPCC Scientific Assessment*, Cambridge Univ. Press, New York, 1990.

Hsu, H-H., B.J. Hoskins and F-F. Jin, The 1985/86 intraseasonal oscillation and the role of the extratropics, *J. Atmos. Sci.*, *47*, 823-839, 1990.

Jackson, D.R., R.S. Harwood, and E. Renshaw, Tests of a scheme for regression retrieval and space-time interpolation of stratospheric temperature from satellite measurements, *Q. J. R. Meteorol. Soc.*, *116*, 1449-1470, 1990.

Jones, R.L. and J.F.B. Mitchell, Is water vapor understood?, *Nature*, *353*, 212, 1991.

Kiladis, G.N. and K.M. Weickmann, Circulation anomalies associated with tropical convection during northern winter, *Mon. Weather Rev.*, *120*, 1900-1923, 1992.

Knutson, T.R., and K.M. Weickmann, 30-60 day atmospheric oscillations: Composite lifecycles of convection and circulation anomalies, *Mon. Weather Rev.*, *115*, 1407-1437, 1987.

Lau, K.M. and P.H. Chan, The 40-50 day oscillation and ENSO: A new perspective, *Bull. Am. Meteorol. Soc.*, *67*, 533-534, 1986.

Lindzen, R.S., Some coolness concerning global warming, *Bull. Am. Meteorol. Soc.*, *71*, 288-299, 1990.

Madden, R.A. and P.R. Julian, Detection of a 40-50 day oscillation in the zonal wind in the tropical Pacific, *J. Atmos. Sci.*, *28*, 702-708, 1971.

Matthews, A.J., B.J. Hoskins, J.M. Slingo, and M. Blackburn, Development of convection along the SPCZ within a Madden-Julian oscillation, *Q. J. R. Meteorol. Soc.*, *122*, 669-688, 1996.

Newell, R.E., Y. Zhu, W.G. Read, and J.W. Waters, Relationship between tropical upper tropospheric moisture and eastern tropical Pacific sea surface temperature at seasonal and interannual timescales, *Geophys. Res. Lett.*, *24*, 25-28, 1997.

Newell, R.E., Y. Zhu, E.V. Browell, W.G. Read, and J.W. Waters, Walker circulation and tropical upper tropospheric water vapor, *J. Geophys. Res.*, *101*, 1961-1974, 1996.

Philander, S.G.H., D. Gu, D. Halpern, G. Lambert, N.-C. Lau T. Li, and R.C. Pacanowski, Why the ITCZ is mostly north of the equator, *J. of Clim.*, *9*, 2958-2972, 1996.

Read, W.G., J.W. Waters, D.A. Flower, L. Froidevaux, R.F. Jarnot, D.L. Hartmann, R.S. Harwood, and R.B. Rood, Upper tropospheric water vapor from UARS MLS, *Bull. Am. Meteorol. Soc.*, *76*, 2381-2389, 1995.

Reber, C.A., The upper atmosphere research satellite (UARS), *Geophys. Res. Lett.*, *20*, 1215-1218, 1993.

Rui, H., and B. Wang, Development characteristics and dynamic structure of tropical intraseasonal convection anomalies, *J. Atmos. Sci.*, *47*, 357-379, 1990.

Salathé, E.P. and D. Chesters, Variability of moisture in the upper troposphere as inferred from TOVS satellite observations and the ECMWF model analysis in 1989, *J. of Clim.*, *8*, 120-132, 1995.

Salby, M.L., and H.H. Hendon, Intraseasonal behaviour of clouds, temperature and motion in the tropics, *J. Atmos. Sci.*, *51*, 2207-2224, 1994.

Schmetz, J., and O.M. Turpeinen, Estimation of the upper tropospheric humidity field from METEOSAT water vapour image data *J. Appl. Meteorol.*, 27, pp 889-899, 1988.

Soden, B.J., Variations in the tropical greenhouse effect during El Niño, *J. of Clim.*, *10*, 1050-1055, 1997.

Soden, B.J. and F.P. Bretherton, Upper-tropospheric relative humidity from the GOES 6.7 μm channel: Method and climatology for July 1987, *J. Geophys. Res.*, *98*, 16669-16688, 1993.

Soden, B.J., and J.R. Lanzante, An assessment of satellite and radiosonde climatologies of upper-tropospheric water vapor, *J. of Clim.*, *9*, 1235-1250, 1996.

Spencer, R.W., and W.D. Braswell, How dry is the tropical free troposphere? Implications for global warming theory, *Bull. Am. Meteorol. Soc.*, *78*, 1097-1106, 1997.

Trenberth, K.E., The definition of El Niño, *Bull. Am. Meteorol. Soc.*, *78*, 2771–2777, 1997.

Wang, B., Reply to comment by B. Wang on "An air-sea interaction model of intraseasonal oscillations in the tropics", *J. Atmos. Sci.*, *44*, 3521-3525, 1988.

Wang, R., K. Fraedrich, and S. Pawson, Phase-space characteristics of the tropical stratospheric quasi-biennial oscillation, *J. Atmos. Sci.*, *52*, 4482–4500, 1995.

Waters, J.W., Microwave Limb Sounding, in *Atmospheric Remote Sensing by Microwave Radiometry*, edited by M.A. Janssen, 383-496, John Wiley, New York, 1993.

Weare, B.C., and J.S. Nasstrom, Examples of extended empirical orthogonal function analysis, *Mon. Weather Rev.*, *110*, 481–485, 1982.

Zhang, C., Atmospheric intraseasonal variability at the surface in the tropical western Pacific Ocean, *J. Atmos. Sci.*, *53*, 739-756, 1996.

Zhang, C., and H.H. Hendon, Propagating and standing components of the intraseasonal oscillation in tropical convection, *J. Atmos. Sci.*, *54*, 741-752, 1997.

Zhu, B., and B. Wang, The 30-60 day convection seesaw between the tropical Indian and western Pacific Oceans, *J. Atmos. Sci.*, *50*, 184-199, 1993.

H. L. Clark and R. S. Harwood, Department of Meteorology, University of Edinburgh, West Mains Road, Edinburgh, U.K. EH8 3JZ. (e-mail: H.Clark@ed.ac.uk; r.harwood@ed.ac.uk

P. W. Mote, Northwest Research Associates, P.O. Box 3027, Bellevue, WA 98009. (e-mail: mote@nwra.com)

W. G. Read, Jet Propulsion Laboratory, 4800 Oak Grove Drive, Pasadena, CA, 91109-8099. (e-mail: bill@mls.jpl.nasa.gov)

(Received January 23, 1998; revised July 17, 1998; accepted August 14, 1998.)